THEORETICAL STUDIES OF THE EPITAXIAL GROWTH OF GRAPHENE

A Thesis
Presented to
The Academic Faculty

by

Fan Ming

In Partial Fulfillment
of the Requirements for the Degree
Doctor of Philosophy in the
School of Physics

Georgia Institute of Technology
December 2011

THEORETICAL STUDIES OF THE EPITAXIAL GROWTH OF GRAPHENE

Approved by:

Professor Andrew Zangwill, Advisor
School of Physics
Georgia Institute of Technology

Professor Walt de Heer
School of Physics
Georgia Institute of Technology

Professor Phillip First
School of Physics
Georgia Institute of Technology

Professor Dimitri Vvedensky
Department of Physics
Imperial College

Professor Kurt Wiesenfeld
School of Physics
Georgia Institute of Technology

Date Approved: 17 October 2011

To my parents and sister,

for all the love and support.

ACKNOWLEDGEMENTS

First, I would like to thank my thesis advisor, Dr. Andrew Zangwill, for his guidance and support. Without him this thesis would not have been possible. During my graduate studies, he has been very patient and always willing to discuss questions with me no matter how simple they are. His concern for his students extends far beyond his duty. His keen insight into the research, insistence of explaining science with explicit pictures and words will continue to guide me throughout my career.

I would like to thank my thesis committee and other faculty members including Drs. Walt de Heer, Dimitri Vvedensky, Phillip First, Edward Conrad, Kurt Wiesenfeld, and Meiyin Chou, for providing support, encouragement and inspiration for this thesis. I have also benefited a lot both personally and professionally from Drs. Claire Berger, Zhigang Jiang, Valery Borovikov and Xiaosong Wu.

I am thankful for the endless discussions with, Dr. Zhimin Song, Dr. Xuebin Li, Dr. Michael Sprinkle, Dr. Chris Malec, D. Britt Torrance, Ming Ruan, Lede Xian, Jeremy Hicks and Baiqian Zhang. Many thanks go to my close friends here, Dr. Shu Huang, Dr. Se il Lee, Chen Li, Yifan Gao, and of course, Yan Li, who have been an indispensable part of my life. Finally, I am deeply grateful to my parents and sister, for their constant support and generous love.

TABLE OF CONTENTS

LIST OF FIGURES

SUMMARY

Graphene, a sheet of carbon atoms organized in a honeycomb lattice, is a two dimensional crystal. Even though the material has been known for a long time, only recently has it stimulated considerable interest across different research areas. Graphene is interesting not only as a platform to study fundamental physics in two dimensions, but it also has great potential for post-silicon microelectronics owing to its exceptional electronic properties.

Of the several methods known to produce graphene, epitaxial growth of graphene by sublimation of silicon carbide is probably the most promising for practical applications. This thesis is a theoretical study of the growth kinetics of epitaxial graphene on SiC(0001). We propose a step-flow growth model using coarse-grained kinetic Monte Carlo (KMC) simulations and mean-field rate equations to study graphene growth on both vicinal and nano-faceted SiC surfaces. Our models are consistent with experimental observations and provide quantitative results which will allow experimenters to interpret the growth morphology and extract energy barriers from experiments.

Recently, it has been shown that graphene grown epitaxially on metal surfaces may lead to potential applications such as large area transparent electrodes. To study deposition-type epitaxial growth, we investigate a new theoretical approach to this problem called the phase field method. Compared to other methods this method could be less computationally intensive, and easier to implement at large spatial scales for complicated epitaxial growth situations.

CHAPTER I

INTRODUCTION

1.1 History & Motivation

Silicon has been the dominant material of the semiconductor industry since the 1960s. The development of complementary metal-oxide-semiconductor (CMOS) technology and photolithography has enabled a continuous miniaturization of electronic devices and an increase of the device packing density. However, this impressive trend is expected to end soon as we are approaching the electronic limits of silicon. One response has been a sustained research effort on carbon nanotubes (CNTs) as a possible basis for post-silicon nanoelectronics. Success has been achieved in manufacturing high mobility, high on-off ratio transistor devices based on single CNTs [1]. Unfortunately, the ultimate issue of placing these CNTs on substrates with high precision impedes the application of CNTs for large scale integrated circuits.

Two dimensional graphene can be viewed as an unrolled CNT. While sharing many electronic properties with CNTs, [2], graphene also has the advantage of providing a two dimensional patternable form that is compatible with state-of-the-art microelectronic processing. Therefore, since its potential as an electronic material was recognized, graphene has been considered as a viable candidate to succeed silicon in post-CMOS electronics [3].

Historically, graphene has been referred to as "monolayer graphite", which was known for many years before the name of "graphene" was officially coined in 1994 [4, 5]. Various methods have been developed to produce this two dimensional crystal. In particular, the epitaxial growth of graphene on silicon carbide (SiC) is most likely

to provide the kind of growth morphology control which is critical for practical applications. The basic mechanism to grow graphene from SiC is sublimation. At elevated temperatures (1200 °C to 1800 °C), Si atoms desorb from the SiC surface, leaving carbon atoms to rearrange themselves to form graphene films. Graphene films grown this way on SiC have an epitaxial crystallographic relationship to the substrate.

Van Bommel et al. first studied surface structures of epitaxial graphene grown by heating SiC in ultra high vacuum (UHV) [6]. It was found that the graphene films produced from the silicon-terminated SiC (0001) (or Si-face) surfaces were monocrystalline while films grown from the carbon-terminated SiC$(000\bar{1})$ (or C-face) surfaces were polycrystalline. Since then, most research on epitaxial graphene has focused on the Si-face.

Unfortunately, UHV prepared graphene films exhibit rough surfaces which are unacceptable for electronic devices [7]. In 2003, de Heer's group at Georgia Tech refined a growth method which places a SiC wafer in a graphite enclosure to control silicon sublimation [3]. This method results in high quality graphene films which exhibit high carrier mobility exceeding 10^4 cm^2/Vs in transport measurements.

Since then, several other techniques have been developed to control the silicon sublimation rate. These methods include increasing the silicon vapor pressure by supplying an additional silicon source such as silane [8] and flowing an inert gas such as argon over the hot SiC surface [9, 10]. In these non-vacuum growth environments, silicon sublimation from SiC terraces is suppressed and graphene grows by decomposing the SiC substrate steps (step flow growth mode).

Despite the progress made, the production of high quality graphene films by the above methods is still challenging and requires comprehensive understanding of the growth mechanism. So far, experimental studies of epitaxial graphene growth have been mostly qualitative. The same is true for the interpretation of the results. To our knowledge, there have been no theoretical studies of epitaxial growth by sublimation

for any material. For these reasons, this thesis is primarily devoted to a theoretical study of the epitaxial growth of graphene on SiC. A final chapter considers the growth of graphene by carbon deposition on a flat (metal) substrate.

1.2 Epitaxial Growth

The term "epitaxy" comes from the Greek, meaning "on" and "arrangement". Epitaxial growth usually refers to growing a single crystal on a single crystal substrate. The epitaxial film (or epilayer) adopts a specific lattice structure and orientation with respect to the substrate. If the epilayer is the same material as the substrate, the growth is called homoepitaxy. Otherwise, it is called heteroepitaxy.

Homoepitaxy can be used to produce large quantities of the same material with high purity. An example is the growth of silicon carbide, which will be discussed in detail in the next Chapter. By contrast, heteroepitaxy, such as metal-semiconductor and insulator-semiconductor epitaxy, has been widely used in microelectronic integration processes.

Conventional epitaxial growth uses a deposition flux from gaseous or liquid precursors. When the deposition atoms are absorbed on a substrate, they become *adatoms*. These adatoms diffuse on the surface. Several adatoms can meet each other and form a stable island. Other adatoms may come to join the existing islands or be adsorbed by the substrate steps and defects where more dangling bonds are present. When there are many islands on the substrate, there will be competition for adatoms between adjacent islands. The islands continue to grow until they coalesce to even larger islands, which eventually cover the whole surface [11]. This growth mechanism has been applied to grow graphene films on metal surfaces (see Chapter VII).

If the growth occurs primarily at the surface steps, two important phenomena emerge known as "step flow" and "step bunching" [12]. At high temperatures, the diffusion length of adatoms is greater than the terrace width and the adatoms are

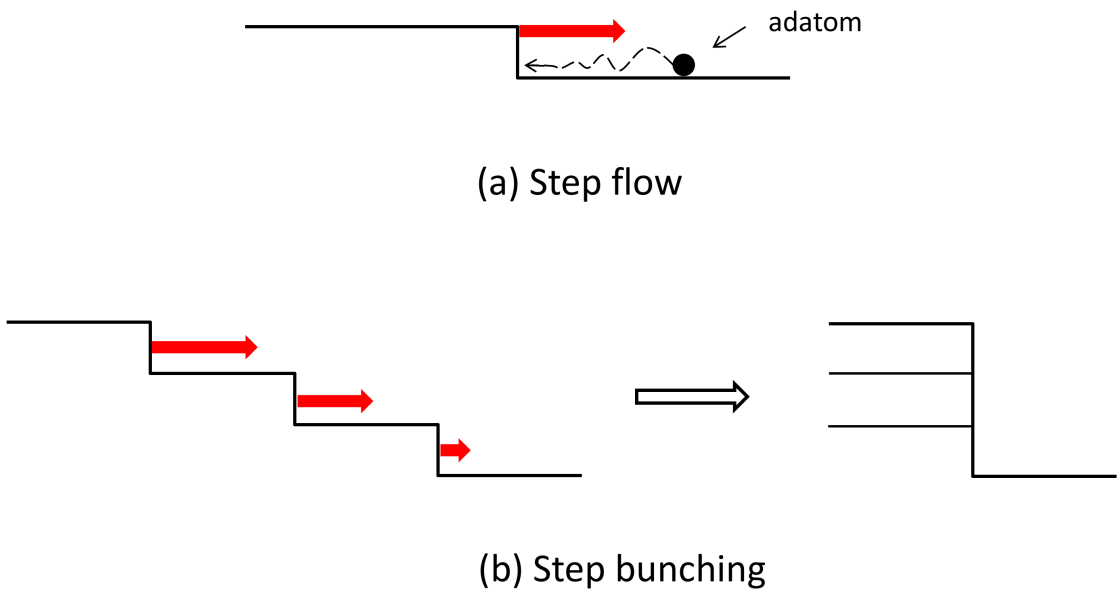

Figure 1: Diagram of step flow (a) and step bunching (b) in conventional epitaxial growth.

incorporated at the step edges without forming islands on the terrace. The incorporation of adatoms causes the steps to advance along the interface (Figure 1(a)). This is called step flow growth. However, if the adatom absorption capability for adjacent steps is not the same, these steps may advance at different velocities. Eventually, they may bunch together to form a larger step, in a phenomenon referred to as step bunching (Fig. 1(b)).

The epitaxial growth of graphene on SiC is unique in the sense that there is no deposition flux. Graphene is grown by thermal decomposition of SiC substrates. Nevertheless, step flow growth and step bunching occur during epitaxial graphene growth. More specifically, step flow growth produces graphene strips as SiC steps decompose and step bunching occurs when the receding SiC steps catch each other and form a larger step.

1.3 Approach & Objective

Several theoretical approaches have been developed to study epitaxial growth. The oldest of these are continuum rate equations, which is a mean-field theory. Other types of continuum models, such as the level set method (LSM) and the phase field (PF) method, include a stochastic deposition flux. To model graphene growth, kinetic Monte Carlo (KMC) simulations are particularly attractive because they are microscopic, and provide a visualization of the growing surface which can be compared directly with experiments.

First-principles KMC simulations of graphene growth from SiC are not feasible at the present time. Not least, nothing is known about the structure of the steps on the interface buffer layer between bulk SiC and the graphene film. The phenomenological KMC model introduced in this thesis is coarse-grained and addresses the step flow growth of graphene on SiC. This approach is similar to the one used to study the growth kinetics of III-V semiconductors [13]. When coupled closely with experiment, this phenomenology produced a decade of valuable insights before simulations based on total energy calculations of energy barriers for III-V systems became possible [14].

We mainly discuss the growth on the silicon-terminated face of SiC. The growth rate on this surface is slower and layer-by-layer growth is straightforward [10, 15]. Our interest is to understand experiments performed in non-vacuum environments where a deliberate attempt is made to control the silicon sublimation. As mentioned earlier, this invariably leads to better quality graphene films.

Our basic modeling strategy is to study the simplest possible kinetic processes, which are consistent with experimental observations. Using these kinetic processes, we build a KMC simulation to predict the growth morphology. In the best case, the values for our phenomenological energy barriers can be extracted by comparison with experimental results.

1.4 Outline

Chapter II is a review of the structural properties of the SiC substrate. The technique of growing SiC and preparing the surface will be discussed because both of them affect the subsequent graphene growth. In Chapter III, a brief review of graphene is provided, including the structural and electronic properties, applications, and production methods. Current experimental progress on epitaxial graphene will be discussed in detail in Chapter IV. This includes a comparison between different growth environments and different SiC surfaces. We will also pay specific attention to graphene/SiC interface structures, because they play an important role in creating any growth model.

In Chapter V, a step-flow growth model is proposed using coarse-grained KMC and rate equations to study graphene growth on SiC vicinal surfaces. When analyzing the simulation results, two growth regimes are revealed. In Chapter VI, the model is extended to include kinetic processes needed to study graphene growth on SiC nanofacets. Finally, we study the conventional deposition growth problem using a phase field method in Chapter VII. Chapter VIII is a summary.

CHAPTER II

SILICON CARBIDE

2.1 Structure, Properties, and Applications

Silicon carbide is a substrate material for graphene growth. The so-called "polytypes" of SiC correspond to different stacking arrangements of the basal plane of silicon and carbon atoms along the vertical c-axis. One such a plane is called a SiC bilayer, as shown in Figure 2. More than 250 polytypes of SiC have been found. These polytypes are divided into two categories. One category is β-SiC which has a zinc blende structure with cubic (C) symmetry (the structure of diamond is an example). All the other polytypes are classified as α-SiC and have either a hexagonal (H) or rhombohedral (R) structure.

β-SiC has only one polytype. When using the notation by Ramsdell [16], this polytype is referred as 3C-SiC. In this notation, "3" denotes the number of planes in the periodic structure, and "C" refers to the cubic structure. The most important polytypes for α-SiC are 4H-SiC and 6H-SiC. The lattice structures for 3C, 4H and 6H SiC are shown in Figure 3. The 4H and 6H polytypes have been used mostly to grow epitaxial graphene.

In Fig. 3, A, B, and C denote the occupation sites of the hexagonal close-packed structure. The SiC lattice is formed by stacking the SiC bilayers (Fig. 2) according to these occupation sites. The stacking order is ABCB ... for 4H-SiC, and ABCACB ... for 6H-SiC. For both polytypes, the c-axis spacing is ~ 2.5 Å and the the in-plane lattice constant is ~ 3 Å. Therefore, the unit cell height for 4H and 6H polytypes is 10 Åand 15 Å, respectively.

We pay specific attention to 6H-SiC, because it is the substrate that this thesis

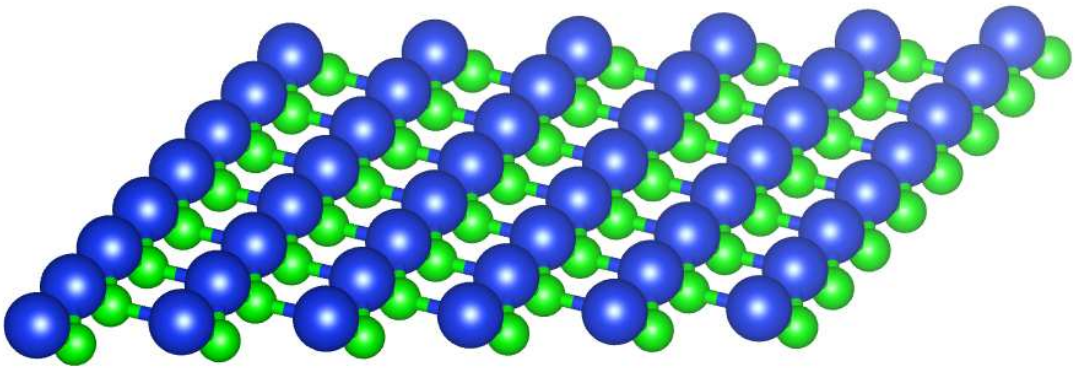

Figure 2: A SiC bilayer. Blue and green spheres represent Si and C atoms respectively.

work uses to model the graphene growth. For all polytypes, the SiC lattice has one surface terminated by silicon atoms, known as the SiC(0001) surface or Si face, and the other surface terminated by carbon atoms, known as the SiC($000\bar{1}$) surface or C face. Note that for hexagonal and rhombohedral structures, the 4-number Bravais-Miller index is often used to represent the crystal planes. These two polar faces play an important role in graphene growth.

SiC is a wide bandgap semiconductor. The bandgaps for 4H-SiC and 6H-SiC are 3.23 eV and 3.05 eV, respectively. As a result, SiC has a high break down electric field when a voltage is applied. For applications, SiC has already been used for ultrafast, high power and high temperature electronic circuits. Moreover, SiC substrates have also been widely used for the growth of group-III nitride semiconductors [17, 18], and of course, for the growth of graphene.

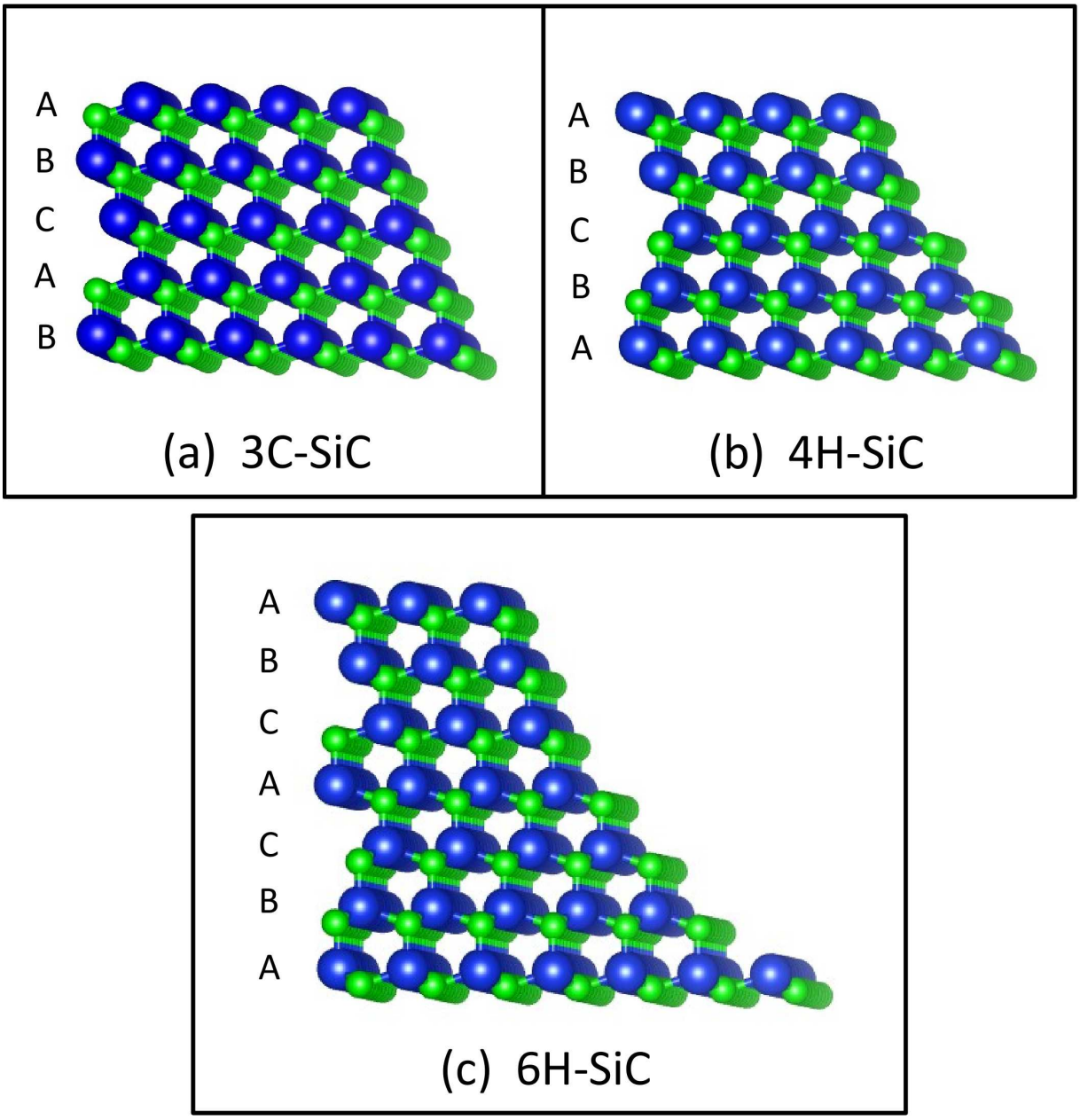

Figure 3: Lattice structure parallel to the $(11\bar{2}0)$ plane for (a) 3C-SiC, (b) 4H-SiC and (c) 6H-SiC, with the c-axis oriented towards $\{0001\}$.

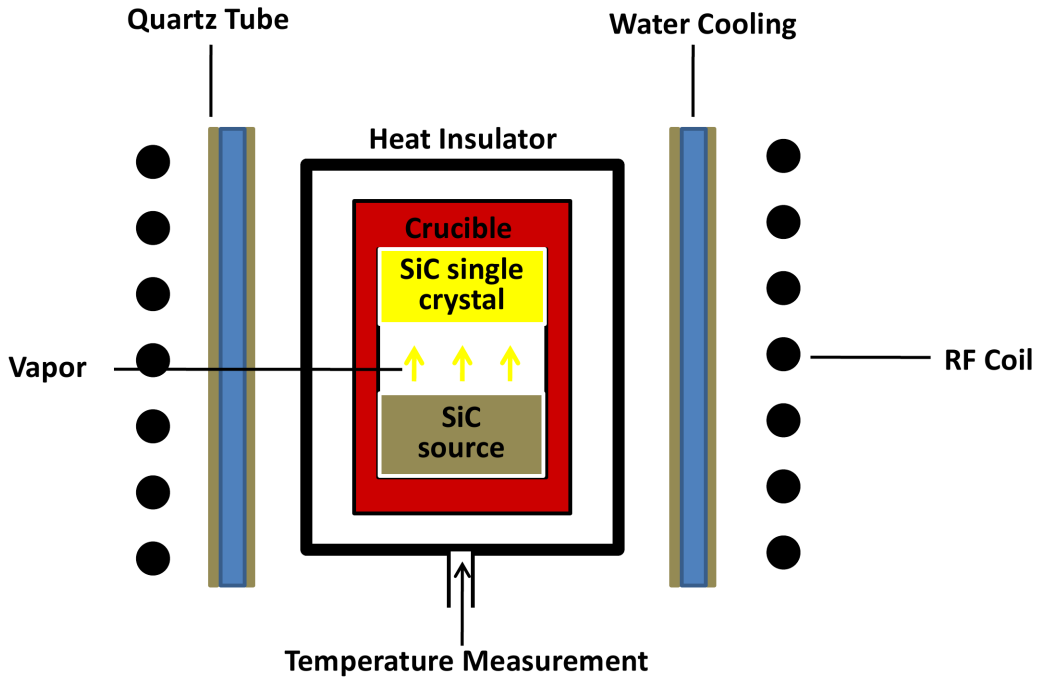

Figure 4: Schematic view of the induction furnace setup of the modified Lely process.

2.2 Production Methods

2.2.1 SiC Homoepitaxy

Several methods are known to grow SiC crystals. The Acheson process is the oldest, and has produced the most SiC material yet, albeit with low crystal quality. High quality α-SiC can be produced by a homoepitaxial sublimation growth method, the so called modified Lely process invented by Tairov and Tsvetkov in 1978 [19].

A schematic view of the growth environment is shown in Figure 4. In the furnace, there is a temperature gradient from the SiC source to the SiC seed crystal. At the hot side, the SiC powder source is vaporized at approximately 2200°C in an argon atmosphere. Under these conditions, the source SiC is kept close to equilibrium with the forming gas species such as Si_2C, SiC_2, Si_2 and Si [20]. These gas species are then driven by a gas pressure gradient and transported to the coldest part of the furnace where they condense onto the SiC seed crystal.

The growth rate is controlled by varying the pressure and temperature gradient

across the furnace, and the distance between the source and seed materials. In 1991, commercially available SiC wafers became available from Cree Research Inc. using this sublimation growth method.

It is important to note that, except for the argon atmosphere pressure, the furnace set-up in Fig. 4 is similar to the one used for the confinement controlled graphene growth [21]. Graphene grows at a much lower temperature (< 1800 °C). This confinement environment maintains a pressure from Si vapor in near chemical equilibrium with the SiC substrate. This growth method produces high quality graphene films.

After growth, SiC ingots are sliced into vicinal wafers whose orientation is often not perfectly on axis, but off-set by an unintentional miscut angle. For example, according to the specifications of SiC by Cree, Inc. [1], the nominal "on-axis" wafer can be made such that the surface orientation is within ±0.25° off the {0001} direction. Intentional off-axis wafers are also commercially available with the steps oriented toward <11$\bar{2}$0> direction.

Other growth techniques for SiC include molecular beam epitaxy (MBE) [22] and chemical vapor deposition (CVD) [23]. These deposition techniques use Si and C containing gas sources such as SiH_4, Si_2H_6,C_3H_8, and C_2H_4, etc. The typical growth temperature is 1500 to 1600°C, which is much lower than used for sublimation epitaxy. The typical growth rate of MBE and CVD epitaxy is low (< 5μm/h), which makes these methods unattractive for commercial production.

We now discuss the growth mechanism for α-SiC homoepitaxy. To ensure the high quality of the epilayer, SiC has to be grown in a step flow mode (or the so called step controlled epitaxy). This is achieved by using an off-axis seed substrate. The surface steps on the off-axis substrate have the long range stacking order of the substrate. Therefore, as all the adatoms are incorporated into the step edges, the epitaxial film

[1] Cree, Inc., "Silicon Carbide Substrates and Epitaxy" (2011), from http://www.cree.com/products/pdf/MAT-CATALOG.pdf

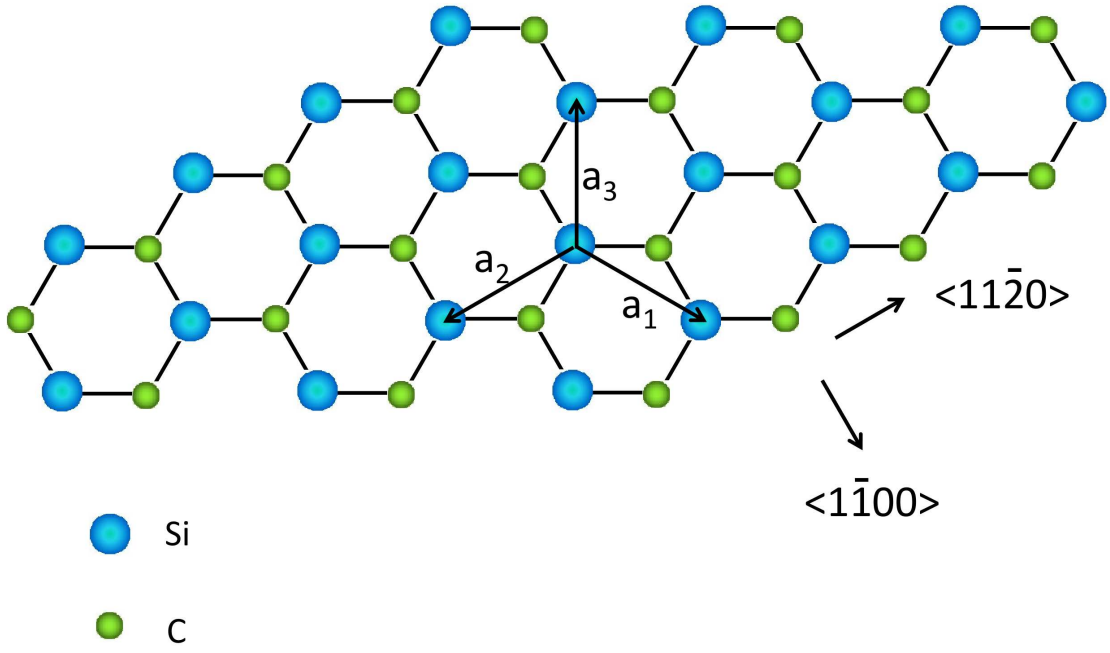

Figure 5: Top views of the crystalline orientations <11$\bar{2}$0> and <1$\bar{1}$00> in a SiC single bilayer.

follows exactly the same stacking order of the substrate.

For the growth of α-SiC, off-axis substrates with miscut steps oriented toward <11$\bar{2}$0> direction are mostly used. Another commonly mentioned crystalline orientation is <1$\bar{1}$00>, which is perpendicular to <11$\bar{2}$0> direction. Both of the two crystalline orientations are shown in Fig. 5. However, growth on 6H-SiC substrates with steps oriented toward <1$\bar{1}$00> produces a stripe-like morphology indicating pronounced step bunching [24]. This will be further discussed in the next Section. Therefore, <1$\bar{1}$00> is not used in SiC homoepitaxy growth.

2.2.2 Growth-induced Step Bunching

Besides step flow growth, step bunching during α-SiC growth is also observed with the formation of microsteps with a height corresponding to the unit cell or half unit cell of SiC [25, 26, 27] (see Figure 6). The microstep formation mechanism has been studied by different groups. Chien et al. [28] suggested that the surface energies may

be different for each SiC bilayer plane in the unit cell ({000n}, where n=1-6 for 6H-SiC). Depending on the occupation sites in the lattice structure, three different SiC bilayers can be identified. When a slower advancing SiC bilayer is caught by faster ones, two types of triple bilayer steps can form: ABC and ACB (see the upper triple bilayer and the lower triple bilayer in Fig. 3(c)). These two microsteps alternate on the surface, similar to those shown in Fig. 6(a).

A close look at Fig. 3(c) shows that these two triple bilayer steps do not have the same dangling-bond configuration. Further step bunching may occur between them and a microstep with a height corresponding to a SiC unit cell forms (Fig. 6(b)). This argument could also apply to 4H-SiC, where the step bunch height corresponds to a SiC double bilayer or quadruple bilayer.

It has been noticed experimentally that the tendency for growth induced step bunching is greater on the Si face than on the C face. Syvajarvi et al. suggested that the surface free energy for the Si-face could be higher than the C-face [29]. This surface free energy is reduced by the formation of hill and valley structures. However, the energy reduction on the C-face is not as large as on the Si-face. This explains why there is less step bunching on the C face.

Step bunching is also more common for the off-axis substrate when compared with the on-axis substrate. This could be caused by the further surface energy reduction when several adjacent microsteps bunch into a macrostep [30]. Moreover, more step bunching is observed for substrates titled toward the $<1\bar{1}00>$ than the $<11\bar{2}0>$ direction. It is clear from Fig. 5 that the step terminations are different between these two directions. As discussed earlier, initial step bunching creates two types of triple bilayer steps. When compared with the $<1\bar{1}00>$ direction, it is possible that there is only a smaller difference of the adatom absorption capability for the two types of triple bilayer steps perpendicular to the $<11\bar{2}0>$ direction, so that they do not tend to bunch together to form bigger steps.

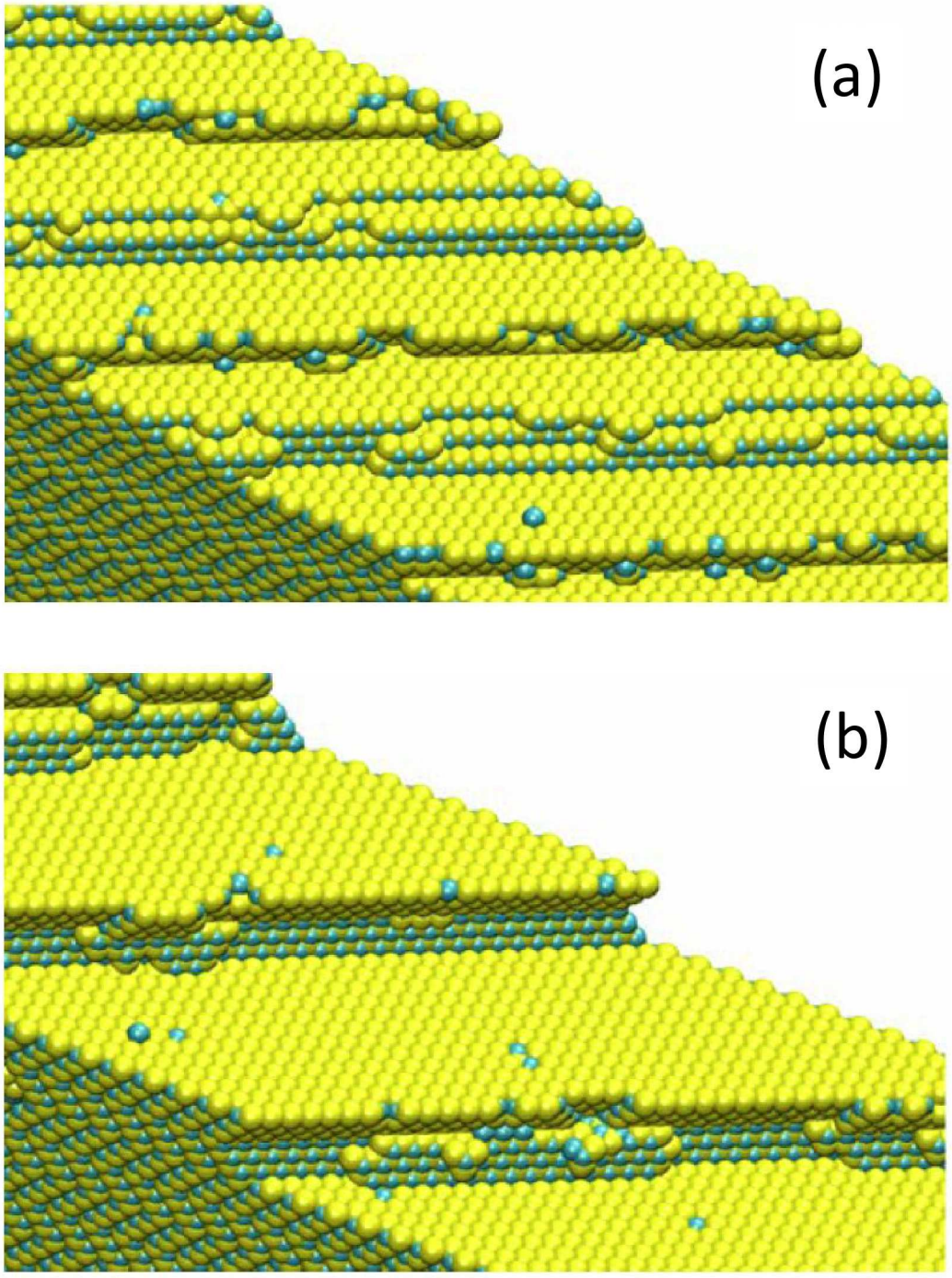

Figure 6: Time evolution of surface morphologies from KMC simulations showing growth-induced step bunching. The initial surface is a vicinal 6H-SiC(0001) surface with miscut toward <1$\bar{1}$00> direction. Yellow and blue spheres represent silicon and carbon atoms, respectively. Images adapted from Ref. [27].

2.2.3 SiC Heteroepitaxy

Despite the success of SiC homoepitaxy techniques, commercial SiC wafers are still expensive and limited in size. On the other hand, it has been shown that silicon substrates can also be used for SiC growth. Given the availability of large scale silicon wafers, this type of SiC growth can significantly increase the SiC wafer size and reduce the cost. For example, heteroepitaxial growth of 3C-SiC film on Si substrate by chemical vapor deposition (CVD) has been proposed [31, 32]. However, 3C-SiC on Si substrates usually are structurally disordered due to the large mismatch of the lattice parameter ($\sim 20\%$) and the thermal expansion coefficient ($\sim 8\%$). The 3C-SiC film also has a rough, curved surface with some cracking. These features have limited the application of heteroepitaxial 3C-SiC for electronic devices.

Nevertheless, some progress has been made to improve SiC heteroepitaxial growth. One example is using off-axis substrates to eliminate the anti-phase disorder [33] which occurs when domains nucleated on the substrate have different crystalline orientations. Another improvement involves the use of a carbonization step to form a buffer layer at the interface between 3C-SiC and the Si substrate. This buffer layer is formed through the reaction of carbon based gas with Si atoms on the surface in order to mediate the large mismatch between the two materials [34]. It is interesting to note that in epitaxial graphene growth, there is also such a buffer layer between bulk SiC and the graphene film. This topic will be discussed in Chapter IV.

In order to develop graphene based electronics, the substrate material has to be made low cost. Since graphene growth doesn't require thick SiC films, epitaxial graphene grown on a 3C-SiC(111) substrate has recently been reported [35, 36]. This could be an impetus for further development of SiC heteroepitaxial growth on Si.

2.3 Etching

2.3.1 Experimental Methods

Chemically abrupt and defect-free SiC surfaces are crucial for electronic applications. This provides the impetus for the surface treatment of SiC. However, commercially available 4H-SiC and 6H-SiC substrates exhibit rough and scratched surfaces due to polishing damage. An effective method to produce atomically flat surfaces is high temperature gas etching using H_2 [37, 38, 39], or H_2 mixtures such as H_2/HCl [40] and H_2/C_2H_4 (or C_3H_8) [41].

The most common process of SiC surface treatment is the following. The as-received SiC wafer with chemical-mechanical polish treatment is initially cleaned with acetone, methanol and HF solutions to remove organic contaminations and any native thin SiO_2 layer. Then the wafer is placed in an open CVD furnace with H_2 containing gas passing through at a temperature between 1400°C and 1700°C for about 30 min.

At high temperature, hydrogen reacts with surface silicon and carbon to form silane and hydrocarbons, both of which are volatile at the etching temperature and can be pumped away [42]. One critical issue is that excess silicon atoms may condense on the SiC surface and form silicon droplets. The addition of C_2H_4 or HCl has been shown to suppress the formation of silicon droplets [43]. This is because increasing the concentration of hydrocarbons can reduce the etching rate while HCl can help to react with excess silicon atoms, producing gaseous chlorosilanes. Typical etching rates are 0.3-2 μm/hour so that a few hundred nanometer of SiC surface material can be removed after etching.

2.3.2 Etching-induced Step Bunching

H_2 etching not only removes polishing damages and surface scratches, but also induces pronounced step bunching. The etched surface usually shows half-unit cell or several unit cell high SiC steps. This is particularly important for graphene growth. The

carbon density in one layer of graphene is almost the same as in a SiC triple bilayer. This means that a decomposing SiC triple-bilayer step leaves behind just enough carbon to form graphene covering the sublimed area. Therefore, graphene growth in step flow mode proceeds by the decomposition of straight step edges. This important observation means we can use a one-dimensional model for the growth. By contrast, graphene growth from single bilayer and double bilayer steps requires surface diffusion of carbon and this leads to a complex, finger-like graphene morphology [44, 45]. We don't treat these cases in this thesis.

Similar to growth-induced step bunching, etching-induced step bunching is usually more pronounced on the Si face for high miscut substrates tilted toward the $<1\bar{1}00>$ direction compared to C face on-axis substrates tilted toward the $<11\bar{2}0>$ direction. In the following, we pay particular attention to the differences between the two directions.

The etching occurs at the SiC step edges, hence the etching rate is expected to be dependent on the SiC step configuration. For straight steps perpendicular to the $<1\bar{1}00>$ direction, the step is terminated by the same type of atoms. In this case, the etching rate is expected to be uniform along the step. The corresponding surface morphology after H_2 etching indeed shows straight steps edges [39].

Fig. 3(c) on page 9 shows that the type of termination atoms can be chosen such that each termination atom has only one dangling bond. This leads to a minimization of the number of dangling bonds at the step edges [46]. However, the real step configuration is not the same as the one in Fig. 3(c). For off-axis 6H-SiC(0001) surface, it has been shown that the stable step configuration corresponds to a high index nano-facet $(1\bar{1}0n)$, with $n \approx 12$ (see Figure 7(a)). These nano-facets make an angle of $\approx 21^\circ$ with respect to the basal planes [39, 47], which is much smaller than the steep angle we show in Fig. 3(c).

A nano-facet usually refers to a stable structure composed of several closely-spaced

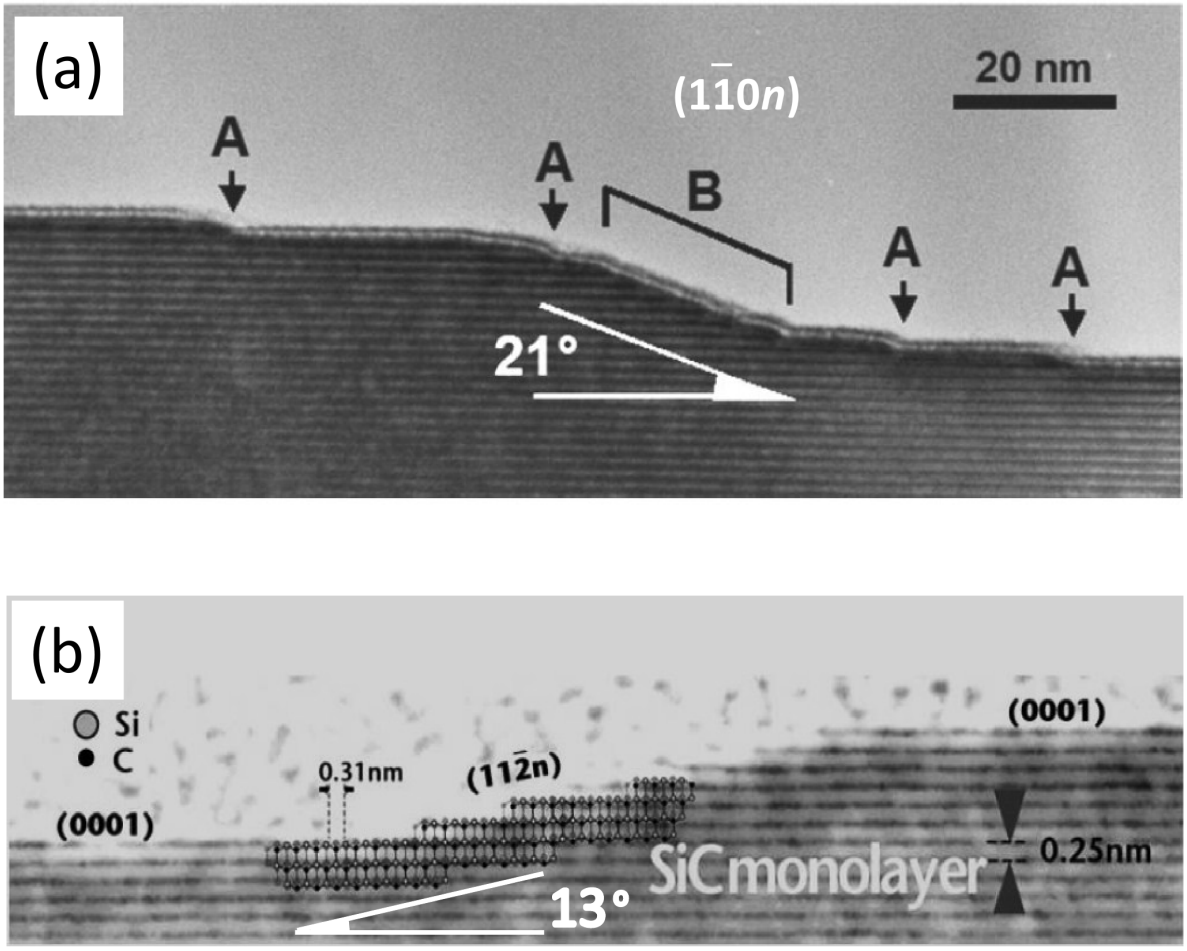

Figure 7: TEM images of nano-facets on the 6H-SiC(0001) surface. (a) A (1$\bar{1}$0n) nano-facet. Image adapted from Ref. [39]. (b) A (11$\bar{2}$n) nano-facet with an atomic drawing of the lattice. Image adapted from Ref. [48].

triple bilayer steps on the flat SiC surface. The observation of nano-facets suggests that, under etching conditions there is a repulsive interaction between adjacent steps. This leads to an increase of the horizontal spacing between these steps. We will study graphene growth on nano-facets in Chapter VI.

A similar situation also occurs for steps perpendicular to the <11$\bar{2}$0> direction. Fig. 7(b) shows a (11$\bar{2}$n) nano-facet on the 6H-SiC(0001) surface. Compared with the (1$\bar{1}$0n) nano-facet shown in Fig. 7(a), the (11$\bar{2}$n) nano-facet has a much lower angle and step height. Typical (11$\bar{2}$n) nano-facets on the 6H-SiC(0001) surface have an angle $13^\circ - 14^\circ$, which corresponds to $n = 16 - 21$ [48]. In Fig. 7(b), the lattice superimposed on the (11$\bar{2}$n) nano-facet shows that the average horizontal spacing between adjacent SiC bilayer steps is $\sim 4a$, where the lattice constant $a = 0.31$ nm.

CHAPTER III

GRAPHENE

3.1 Structure, Properties and Applications

Graphene is a name given to an atomic layer of carbon atoms covalently bonded into a honeycomb structure with a nearest neighbor distance of ~ 1.4 Å. Boehm et al. isolated and identified single graphene sheets by transmission electron microscopy (TEM) and X-ray diffraction in 1962 [4], and named the material "graphene" in 1994 [5]. Van Bommel et al. first studied the structure of "graphite monolayer films" grown by heating SiC at high temperatures in UHV in 1975. However, it is only recently that graphene was discovered to be a two dimensional electronic system with superior transport properties [3, 49].

The graphene unit cell consists of two carbon atoms. Each carbon atom has four valence electrons, of which three are used in the graphene lattice for sp^2 hybridization bonds (also known as σ bonds in graphene). The fourth electron of the carbon atoms occupy p_z orbitals, which give rise to the π state in graphene. These electrons are responsible for electron conduction. The electronic bands of graphene are different from conventional parabolic bands found in most three dimensional materials. In the 1940s, P. R. Wallace used a tight-binding method and showed that the energy band dispersion is linear for low energies near the six corners of the Brillouin zone [50] (Fig. 8(a)). This is given by Eq. 1, where v_F is the Fermi velocity. The value of v_F in graphene is about 10^6 m/s or 1/300 of the light velocity. The effective mass is defined as $m^* = \hbar^2(\frac{d^2E}{dk^2})^{-1}$. It is clear from Eq. 1 that the current carriers in graphene have zero effective mass.

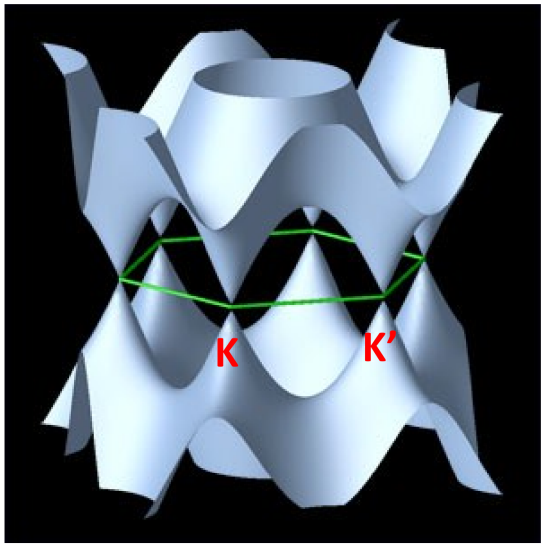

(a) Band Structure

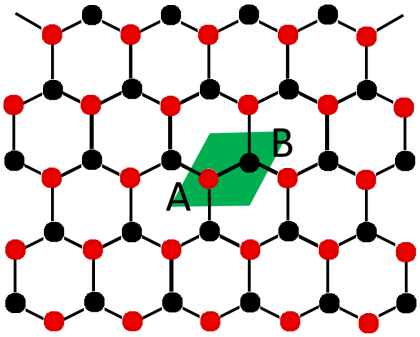

(a) Bi-particle lattice

Figure 8: (a) Graphene Brillouin zone, with the locations of K and K' marked. (b) Graphene hexagonal lattice. The unit cell (highlighted in green) consists of two carbon atoms.

$$E = \hbar v_F k \tag{1}$$

Graphene is a *semi-metal* where the conduction band and the valence band touch at a single point called the Dirac point. If the Fermi level is above zero energy, the current carriers are electrons. If the Fermi level is below zero energy, the valence band is not full, and unoccupied electronic states behave as positively charged holes. Both electrons and holes in graphene are called quasi-particles, which are governed by the Weyl Hamiltonian for neutrinos $\hat{H}(\mathbf{k}) = -\hbar v_F \boldsymbol{\sigma} \cdot \mathbf{k}$. Here, $\boldsymbol{\sigma}$ is the 2D Pauli vector and $\mathbf{k}$ is the momentum vector.

The Pauli vector comes from the crystal symmetry of the two sub-lattices in a unit cell (marked as A and B in Fig. 8(b)). It turns out that the wave functions of the quasi-particles have two components, which are analogous to spinor wave functions. For this reason, σ is usually called "pseudo spin". The pseudo spin is either parallel or anti-parallel to the carrier momentum. Therefore, like in the neutrino physics, a *chirality* can be defined, which is the projection of $\boldsymbol{\sigma}$ on the direction of $\mathbf{k}$. The pseudo spin leads to many interesting quantum phenomena including an unusual half integer quantum Hall effect and electron-hole symmetry. These electronic properties are unique to graphene, and are sometimes used to identify whether or not the material system under investigation is graphene.

The conservation of pseudo spin and chirality prohibits electron backscattering from $\mathbf{K}$ to $\mathbf{K}'$ in Fig. 8(a). This property leads to a substantially high mobility of the order of 10,000 $\mathrm{cm^2V^{-1}s^{-1}}$. Ballistic transport of the charge carriers in graphene occurs at relatively high temperatures[3, 51, 52].

The important properties of graphene are summarized as follows. Graphene has strong C-C valence bonds, which are mechanically and chemically stable down to atomic dimensions. Its two dimensional structure opens up possibilities for chemical modification and lithographic patterning. The charge carriers in graphene have a

remarkably high mobility and behave like massless Dirac fermions. This is essentially why graphene is widely considered to be a promising candidate to succeed (or at least complement) silicon in the semiconductor industry.

On the other hand, it is unfortunate that (unlike CNTs which can be an intrinsic semiconductor) graphene does not have an energy gap. This severely limits the potential of graphene in logic circuit applications. For example, the maximum off-to-on resistance ratio that has been demonstrated for graphene field effect transistors (FET) is about 10^2-10^3 at room temperature [53, 54]. Therefore, without modifications, graphene can not be used directly in microelectronic applications such as field effect transistors.

Many approaches have been proposed to open a band gap in graphene. One is to cut the two dimensional structure into narrow ribbons through nano-lithography techniques [3]. By using this method, in analog to CNTs, the carriers in graphene are confined in a quasi one dimensional system. The confinement is expected to quantize the charge carrier momentum in the width direction. Depending on the boundary conditions, the quantization can result in a finite energy band gap. First principle calculations predict that the energy band gap scales inversely with the ribbon width [55].

This narrow-ribbon induced band gap has been demonstrated by several groups. For example, Han et al. [56] patterned mechanically exfoliated graphene narrow ribbons on a SiO_2/Si substrate using e-beam lithography and etching techniques. They found that an energy band gap as large as 200 meV can be achieved on a 15 nm graphene ribbon. High quality graphene narrow ribbons less than 10 nm in width can be chemically derived from unzipped CNTs. These ribbons can have a band gap up to 0.4 eV, and produce FETs with on-off ratios of about 10^7 [57].

Several other methods to open a band gap in graphene are known. One example is applying a perpendicular electric field in a bilayer graphene system [54]. Another

more convenient way is to chemically convert graphene to a semiconductor by adding oxygen, hydrogen or fluorine groups to the graphene surface[58, 59, 60].

Scaled production of narrow ribbon graphene FETs can be obtained by patterning wafer size epitaxial graphene grown on SiC substrates [53]. Recently, the Georgia Tech group showed that narrow graphene ribbons grow on SiC nano-facets at specified positions [61]. These nano-faceted substrates are prepared by plasma etching lithography. Ribbons as narrow as 40 nm can be achieved. We discussed in Chapter II that SiC nano-facets can also form spontaneously by H_2 etching and high temperature annealing. This opens up possibilities of growing graphene nano-ribbons by a direct control of SiC surface steps. Graphene growth on nano-faceted SiC substrates will be discussed in detail in Chapter VI.

While the low on-off ratio may be a critical issue for graphene logic devices, there is a need to develop high speed analog transistors which do not require a large on-off ratio. Instead, this type of transistor requires a current and a power gain operating at substantially high frequencies. Graphene is a promising candidate for these applications because of its high mobility and high saturation velocity. In 2010, IBM fabricated 100-GHz transistors from epitaxial graphene [62]. In 2011, a wafer-scale graphene integrated circuit operating as a broadband radio frequency mixer at frequencies up to 10 GHz was also demonstrated [62]. These developments mark the first application of graphene based electronics.

Other than making FETs, graphene's high conductivity and optical transparency can also be used as transparent electrodes for display screens [63]. Moreover, due to the two dimensional structure, graphene can be used as a gas detector [64]. However, gas molecules do not absorb directly on graphene. Therefore, a surface chemical modification is usually required.

3.2 Production Methods

3.2.1 Exfoliation

It has been known for a long time that very thin graphite films can be obtained by tearing sheets from highly oriented pyrolytic graphite (HOPG) surfaces. HOPG is a polycrystalline material composed of highly oriented graphene sheets with a domain size of micrometers. In the surface science community, several techniques have been developed to isolate thin graphite films. For example, graphene sheets can be manipulated on HOPG surfaces with a scanning tunneling microscope (STM) and atomic force microscope (AFM) tips [65, 66]. Also by inserting large molecules into HOPG, large separations between the graphene sheets can be created so that these sheets can be considered as isolated graphene [67].

A more direct way to extract graphene sheets from HOPG is by scraping the thin HOPG samples against other surfaces. Surprisingly, this method proves to be very efficient to produce thin graphite films [68]. This micromechanical-cleavage method was further refined by the Manchester group to fabricate graphene films down to a few atomic layers [49]. These graphene films are usually referred as exfoliated graphene.

The production process is simple. A HOPG flake is repeatedly peeled by an adhesive tape until it becomes visibly thin. Then the tape is pressed against a Si/SiO_2 substrate, so that graphene flakes can come off the tape and be deposited on the substrate. After the tape is peeled off, the Si/SiO_2 wafer is placed under an optical microscope. Occasionally, some few-layer graphene films are found on the surface. The tricky part is that the thickness of the SiO_2 has to be carefully chosen ($\sim$ 300 nm) so that the graphene films can be optically visible by light interference.

Although this technique is crude and requires a large amount of time to identify the graphene single layers under an optical microscope, a graphene film made this way can have a domain size of 10 – 100 μm, which is sufficiently large for scientific experimentation. Indeed, the quantum Hall effect in graphene was discovered using an

exfoliated sample [69]. That being said, given the production method's uncontrollable and inefficient nature, it is unsuitable for commercial applications.

3.2.2 Growth on Metals

Graphene growth on metals, metal carbides and silicon carbide can produce graphene films that have the dimensions of the substrate. Therefore, they are much more efficient as production methods when compared to the exfoliation method. It has been known for a long time that graphene films can grow on various closed packed transition metal carbides or metals (Ni, TaC, TiC, Pt, Ru, Cu, etc.) by the dissociation of carbon monoxide or hydrocarbons at elevated temperatures. Some of the early demonstrations of monolayer graphene growth on metals were reported in Ref. [70, 71, 72, 73]. The growth of single-layer graphene can be achieved by controlling the reaction temperature at the substrate surface. Growth can be done by MBE or by CVD.

Different growth mechanisms have been found when the substrate and the growth condition are varied. For example, annealing an ethylene covered Pt(111) surface to 800 K leads to the formation of small islands (20 – 30 Å) uniformly distributed over the surface. Further annealing at 1230 K results in the formation of a few larger regularly shaped islands (several hundred Å in size) at the lower step edges of the Pt surface, which is due to the coalescence of the initial small islands.

By contrast, ruthenium (Ru) substrates always have a substantial number of carbon atoms dissolved in the bulk. When sputtering or heating Ru substrates between 1000 to 1400 K, graphene starts to grow on the surface by the segregation of carbon atoms to the surface from the bulk. Large graphene islands of several hundred Å in diameter can form at the lower step edges of a Ru surface [74].

Sutter and co-workers [75] refined the method to grow graphene on Ru. The Ru sample is first brought quickly to a high temperature when the carbon atoms are still

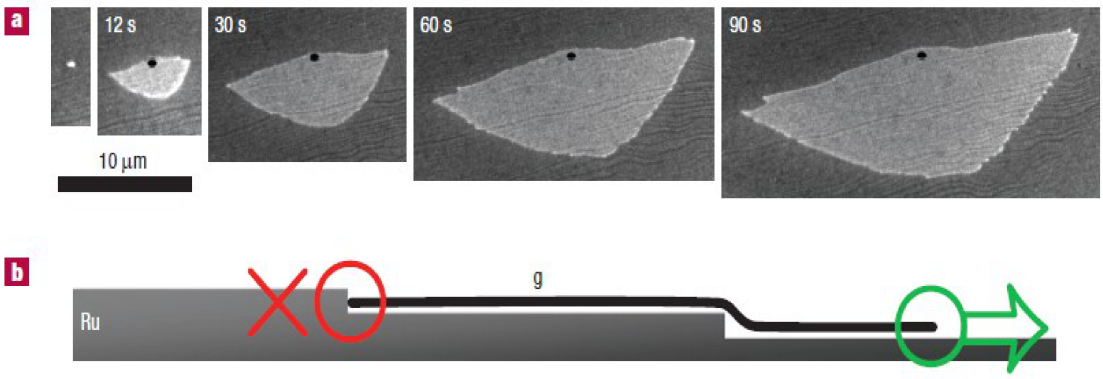

Figure 9: (a) Time-lapse sequence of LEEM images showing first-layer graphene island growth on Ru(0001) at 850 °C. Time was recorded after the nucleation of the graphene island. The steps are marked as faint dark lines, with the downhill direction from upper left to lower right. The black dot is the position of the initial graphene nucleus. (b) Schematic cross-sectional view of the graphene sheet growing in the downhill direction. Images adapted from Ref. [75].

dissolved in the bulk. This is followed by a slow cooling from 1150 °C to 825 °C, which drives carbon atoms to the surface. These carbon atoms sparsely nucleate graphene islands of macroscopic size (>100 μm) across many surface Ru steps as shown in Figure 9(a).

Fig. 9(a) shows that the graphene growth is entirely suppressed in the uphill direction as indicated by the nucleation location of the black dot. The growth in the downhill direction is not limited by the surface steps. This leads to a carpet-like graphene sheet across many steps, but with the higher side pinned at a Ru step edge (Fig. 9(b)). It is thought that a graphene sheet has an orbital overlap with an uphill Ru step edge so that the edge of the graphene sheet is immobile. However, there is no such orbital overlap when graphene sheet meets a downhill Ru step, and the growth in this direction is essentially uninterrupted.

More interesting perhaps is that the first-graphene layer on Ru is strongly bonded with the Ru substrate, whereas the second-graphene layer is weakly bonded to the substrate and retains the electronic structure of graphene. This is similar to graphene

growth on SiC(0001) where a carbon rich buffer layer exists at the interface between SiC and the first-graphene layer [7]. The structure of the epitaxial graphene – SiC system will be further discussed in the next Chapter.

Graphene sheets exceeding 1 cm^2 in area can be grown on thin nickel (Ni) and copper (Cu) films at a low pressure[63, 76]. The growth on these substrates is self-limited to a single graphene layer, which makes this type of graphene very attractive for transparent electrode applications. However, graphene films grown on metals requires a transfer to other substrates and a subsequent etching of the metal, which may affect the electronic properties of the graphene.

3.2.3 Growth on Silicon Carbide

Single and few-layer graphene has been grown by thermal decomposition of SiC. At high temperatures, silicon atoms desorb from the surface, leaving carbon atoms which reorganize into a graphene honeycomb structure. The graphene film quality and thickness can be controlled by the growth temperature, annealing time and silicon vapor pressure. Graphene produced in this way has the dimensions of the SiC wafer and a very high carrier mobility of the order of 10^4 cm^2/Vs. Graphene films grown on insulated SiC can be patterned directly to electronic devices without transferring to other substrates.

Epitaxial graphene on SiC has been characterized extensively by various surface analysis tools and electronic transport measurements. These experiments reveal that single layer graphene grown on the Si-face and (remarkably) multi-layer graphene grown on the C-face retain the electronic properties of free standing graphene sheets, such as the linear energy dispersion [77], Berry's phase [78] and half integer quantum Hall effect [79], etc. Given the above reasons, the epitaxial growth of graphene on SiC has been considered as a very promising candidate for electronic applications.

Besides the production methods we have discussed so far, many other methods

have also been known to produce graphene. For example, graphene obtained by reducing graphene oxide flakes was reported as early as in 1962 [4]. The reduction is tunable by controlling the heating. With a thermal conducting AFM tip that can locally heat graphene oxide, this technique can be used to pattern graphene nanoribbons [58].

CHAPTER IV

GRAPHENE GROWTH ON SILICON CARBIDE

In this Chapter, we discuss experimental progress in the growth of graphene on silicon carbide substrates. Understanding the growth morphology and observed structures is crucial to the development of any growth model.

4.1 UHV vs Non-vacuum Growth

As mentioned previously, few-layer graphene on SiC was first grown in ultra high vacuum (UHV, pressure < 10^{-9} Torr) above 800 °C in the 1970s [6]. In UHV, gas molecules have a mean free path that is orders of magnitude larger than the size of the growth chamber. This leads to a growth surface with no contamination. Moreover, UHV growth enables the use of many surface analytic techniques. In particular, low energy electron microscopy (LEEM) allows researchers to observe graphene growth in real time, which is very helpful to understand the growth mechanism.

Unfortunately, graphene grown in UHV has poor surface quality as shown in Figure 10(a). At high temperatures, silicon atoms are driven out of the surface at a high sublimation rate, leaving carbon atoms behind. This is a far-from-equilibrium process which leads to SiC substrate roughening. Even though the starting vicinal surface has a terrace width of micrometer size, the surface after graphitization has random steps with an average terrace width less than 500 Å[80]. The amount of released carbon atoms from the SiC single or double bilayer steps is not sufficient to form graphene that can cover the sublimated area [45]. As a result, adjacent steps bunch together and form deep pits [81]. Thicker graphene can nucleate in the pits where there is sufficient carbon source before the SiC terrace is covered by a single layer graphene. Eventually, the growth morphology becomes non-uniform.

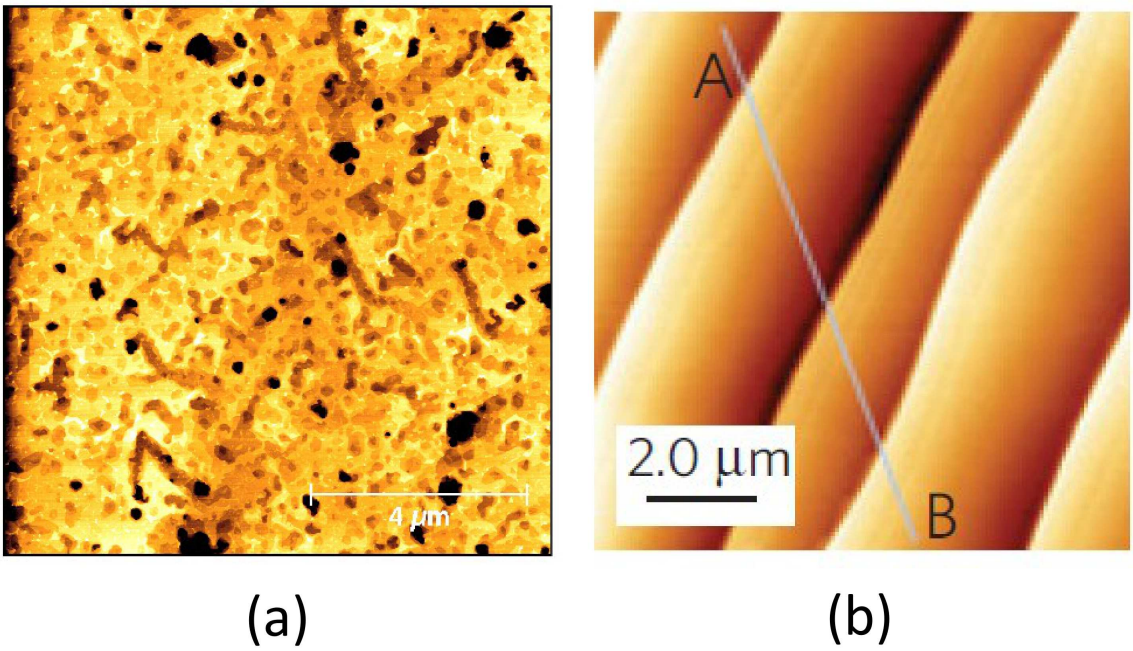

Figure 10: Surface morphology of graphene grown on SiC in UHV and non-vacuum environments. (a) Graphene grown on 6H-SiC(0001) in UHV shows poor surface quality. Sample was heated by e-beam bombardment of the back side to 1350 °C for 4 min at 10^{-9} Torr. Image adapted from Ref. [82]. (b) Graphene grown on 6H-SiC(0001) by annealing in Argon at 900 mbar pressure at 1650 °C. Image adapted from Ref. [10].

Increasing the silicon vapor pressure in the growth environment can suppress the silicon desorption rate. As a result, the graphitization occurs at a higher temperature. The enhanced silicon and carbon surface diffusion can repair surface vacancies and grain boundaries. This results in a much smoother growth surface. As discussed earlier in Chapter II, for Si face growth, higher temperature also promotes SiC step bunching, which creates large macrosteps and wide terraces. At graphitization temperatures, there is sufficient carbon source at the macrostep to form graphene. Therefore, compared to the UHV environment, the non-vacuum growth environment leads to a much better quality of graphene films, as shown in Fig. 10(b).

There are several different ways to control the silicon vapor pressure. For example, the Georgia Tech group uses a graphite enclosure. The silicon evaporation rate is suppressed by the return of silicon atoms to the surface from the enclosed environment. Hence, the SiC substrate is near equilibrium with the silicon vapor above. This method is very effective to produce large areas of monolayer or multilayer graphene films [21]. Other methods include supplying a silicon compound (silane) [8], and growing graphene in an argon atmosphere [10, 9].

4.2 Growth on SiC Planar and Non-planar Surfaces

We have mentioned that the graphitization behavior on the two polar surfaces of SiC is quite different. Graphene grown on the Si face in UHV has been characterized by low-energy electron diffraction (LEED), x-ray photoelectron spectroscopy, and angle-resolved photoemission spectroscopy [83]. These studies reveal that upon heating, the substrate undergoes a series of reconstructions: (3×3) – (1×1) – $(\sqrt{3}\times\sqrt{3})$R30 – $(6\sqrt{3}\times6\sqrt{3})$R30, with a graphitization temperature ~ 1100 °C. The graphene films are usually thin on the Si face, about 1 ~ 5 layers. Graphene multilayers are AB (Bernal) stacked, i.e., after one layer of graphene, one gets graphite.

The growth on the C face is quite different. The graphene growth rate tends to

be harder to control and results in much thicker graphene films[84]. In the early UHV studies, the C face films usually had multiple orientational phases and poor surface quality [6]. Given these reasons, there have been fewer studies on this face. With increasing temperature, the substrate also shows reconstructions: $(1\times1)/(\sqrt{3}\times\sqrt{3})$R30 – (3×3) – $(2\times2)_C$ [85]. The typical C-face graphitization temperature for UHV growth is ~ 1200 °C.

Using the previously mentioned confinement controlled sublimation method, the Georgia Tech group is able to produce high quality graphene films on SiC$(000\bar{1})$ above 1400 °C, which is much higher than the graphitization temperature used in UHV growth. The graphene films on the C-face can have a much larger domain size, and the carrier mobility is at least an order of magnitude higher than that of graphene films grown on the Si-face [21]. Multilayer graphene grown on the C face has a high density of rotational stacking faults where adjacent graphene sheets are rotated with respect to each other and Bernal stacked layers are less than 15% of the film [80, 21]. Due to this unique structure, the electronic properties of C-face grown multilayer graphene are identical to those of an isolated graphene sheet [78, 86, 87, 77].

Despite the significant differences in surface morphology and growth structures, STM studies show that both Si-face and C-face graphene grow continuously over SiC steps [88, 89]. This suggests that the graphene domains are highly oriented within the same graphene sheet.

More recently, graphene growth on SiC(0001) nano-faceted surfaces has been studied. The H_2 etched or off-axis SiC surface often exhibits self-ordered nano-facet structures consisting of pairs of (0001) basal planes and $(1\bar{1}0n)$ (or $(11\bar{2}n)$) nano-facets, depending on the wafer's miscut orientation [90, 15, 91]. It is found that the graphene growth is initiated exclusively at these nano-facets where the Si atoms are less bonded. In fact, several graphene layers can grow on the nano-facet before the growth propagates onto the basal planes [90]. The subsequent graphene growth on the basal planes

proceeds in a layer-by-layer mode [15, 10].

This usually leads to a better control of the quality of the graphene films on the adjacent terraces [10, 92]. Growth on nano-facets also plays an important role in graphene ribbon growth [61]. Little is known about the interface structure and the stacking order of the graphene films grown nano-facets.

4.3 Graphene/SiC Interface Structures

In the following, the graphene/SiC interface will be reviewed and discussed. In this context, there are two types of graphene/SiC interface structures. One is the interface layer between bulk SiC and newly formed graphene sheets above, the other is the interface between a sublimating SiC step and the adjacent graphene sheet.

The first type of interface on the Si-face is well known. STM, LEED and x-ray diffraction analysis of the graphene – SiC system reveals that the $(6\sqrt{3} \times 6\sqrt{3})$R30 reconstruction is not only a precursor phase to graphene formation but also exists between the bulk SiC and graphene films with only a slight change [93]. In the growth structure, the $(6\sqrt{3} \times 6\sqrt{3})$R30 reconstruction is located 1.6 Å (the spacings cited in this Section are all for 4H-SiC) above the bulk SiC. This interface layer is often referred to as a "buffer layer". This buffer layer has a carbon density that is about the same as graphene, but is composed of a mixture of sp^2 and sp^3 bonded carbon atoms, indicating that they have a strong interaction with the substrate [94, 80]. The first graphene layer is ~ 2.3 Å above the interface layer, which is much less than the graphite inter-plane spacing of 3.35 Å. The spacing between the first and the second graphene layer is about 3.5 Å. This is close to the average spacing between subsequent layers of 3.35 Å, which is also the inter-plane spacing in graphite.

There have been fewer studies on the first type of interface on the C-face, perhaps due to the difficulty of preparing high quality thin graphene films on this polar face. X-ray reflectivity suggests that there is also a carbon-rich interface layer which is

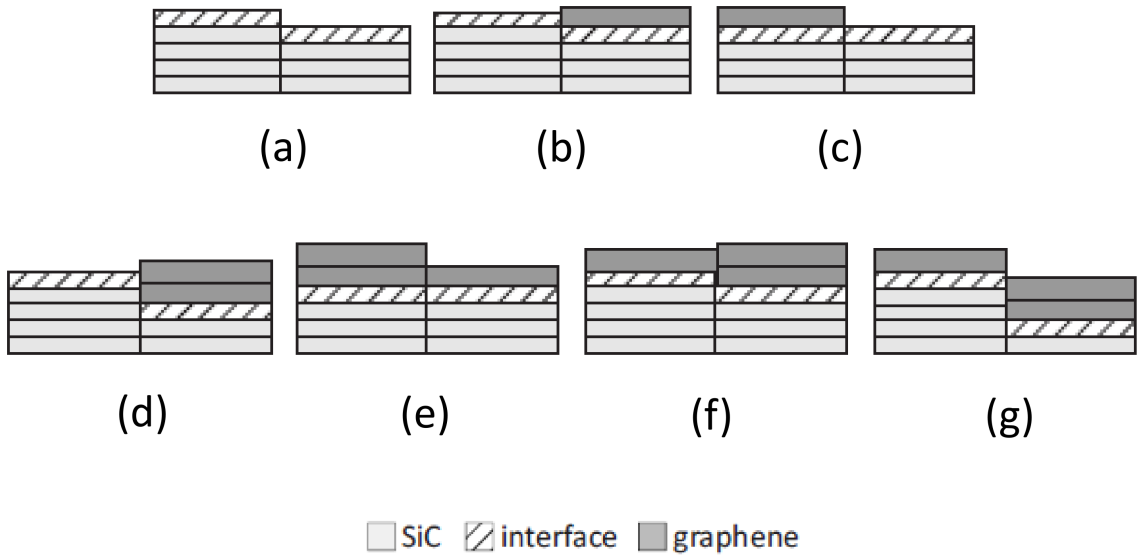

Figure 11: Configurations of SiC substrate steps and graphene layers. 6H-SiC(0001) surface was graphitized under Argon atmospheric pressure. Image adapted from Ref. [96].

located about 1.6 Å above the bulk SiC and has a carbon density slightly larger than a graphene sheet [80]. The bonding between the interface layer and the underlying bulk SiC is similar to that in diamond. The first graphene layer is ~ 1.6 Å above the interface layer. The spacing between the first and the second graphene layer is about 3.4 Å. The average spacing between subsequent layers is 3.37 Å, slightly larger than the inter-plane distance in graphite. This is likely caused by the rotational stacking faults. However, it is not clear how the interface layer results in the rotational stacking faults of the above graphene films during the growth.

At elevated temperatures, for both the Si-face and the C-face, new carbon atoms liberated by Si sublimation immediately below the buffer re-crystallize to form a new buffer layer, while the old buffer layer is pushed up and become a graphene sheet. New graphene layers form underneath the old ones [95], one at a time.

When studying the step growth of graphene, the second type of interface obviously

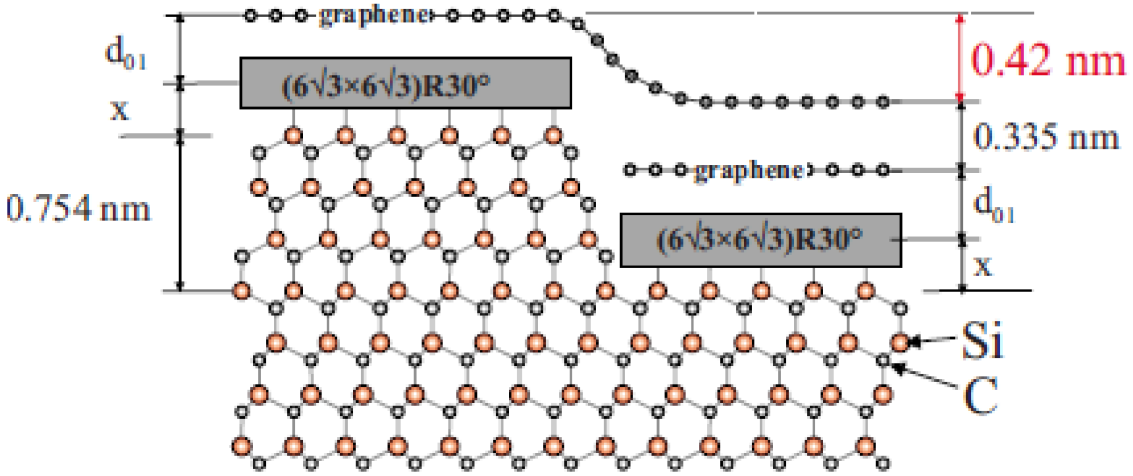

Figure 12: Conjectured atomic structures for Fig. 11(g). Image adapted from Ref. [96].

plays an important role. Kelvin probe force microscopy (KPFM) studies of graphene growth on 6H-SiC(0001) show different SiC step – graphene structures. These are summarized in Figure 11. Due to different surface preparation methods, SiC surface steps may have a height less than a triple bilayer, such as those in Fig. 11(a), 11(b), 11(d) and 11(f). On the other hand, for triple bilayer SiC steps, three types of configurations – Fig. 11(c), Fig. 11(e) and Fig. 11(g) – are found. In Ref. [89], Fig. 11(g) corresponds to the atomic structure as shown in Figure 12. No explanation is known for Fig. 11(c) and Fig. 11(e). In Chapter V, we will introduce a kinetic model based on the step flow growth of graphene, which reproduces the growth morphology in Fig. 11(c), Fig. 11(e) and Fig. 11(g).

Note that Fig. 12 does not indicate any atomic bonding between the SiC step and the graphene sheet. In truth, nobody knows. As previously discussed for graphene growth on Ru, the atomic bonding configuration may potentially lead to an anisotropic growth of the graphene nucleus. Figure 13 shows one of the few high-resolution STM image of the junction between graphene and an adjacent SiC(000$\bar{1}$) substrate[97].

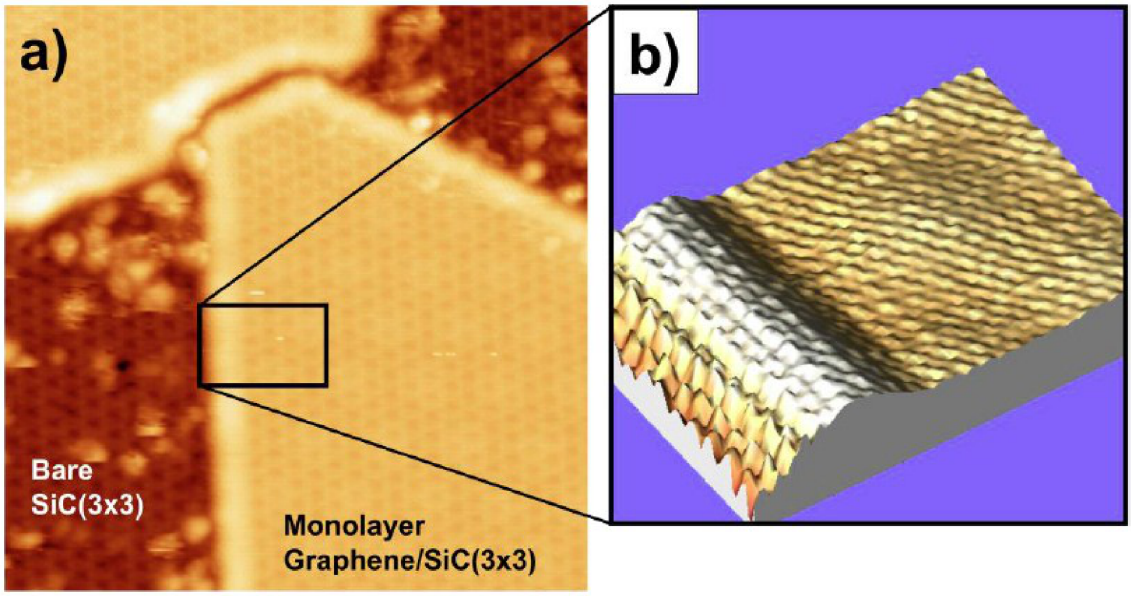

Figure 13: Interface between graphene and bare SiC($000\bar{1}$). (a) STM image of a graphene monolayer on (3×3) SiC reconstructed surface. (b) A zoomed-in STM image showing the interface between the graphene sheet and the SiC. Image adapted from Ref. [97].

In Fig. 13, the graphene edge is folded toward the SiC surface with a fold height of 50 pm. This fold feature could release the compressive stress which occurs due to the relative thermal contraction between graphene and SiC when the sample is cooled down after growth. Similar fold features have also been seen in STM images of Si-face grown graphene layers [89], but the cause has not been explained. We expect that more surface investigations around SiC surface steps covered by graphene will provide more information.

CHAPTER V

GRAPHENE ON SIC VICINAL SURFACES

5.1 Introduction

In this Chapter, we introduce a kinetic model for the growth of epitaxial graphene on 6H-SiC(0001) vicinal surfaces [98]. As discussed previously in Chapter II, the H_2 etched SiC surface is typically composed of a periodic array of half-unit-cell-height steps. Experimental results show that step flow sublimation of SiC promotes the nucleation and growth of graphene strips parallel to the step edges (refer back to Fig. 10(b)). Therefore, a one-dimensional model for the growth is sufficient. The model parameters are effective energy barriers for the nucleation and subsequent propagation of graphene at the step edges.

To model the growth, our computational tools are the kinetic Monte Carlo (KMC) method and rate equations. The KMC simulations are designed to mimic the time evolution of the kinetic processes that occur during growth. Rate equations are differential equations for the time-evolution of certain average quantities. They can be used to compare with the KMC simulations and gain further information about the growth kinetics.

This Chapter is organized as the follows. We will introduce our KMC model in Section 5.2 and show that the model is consistent with experimental observations. The simulation results will be further discussed in Section 5.3. In Section 5.4, a rate-equation analysis will be provided to gain further insights into our KMC simulations.

5.2 Modeling Growth on Vicinal Surfaces

5.2.1 Objective

Our KMC model focuses on vicinal surfaces and aims to (i) provide experimenters with a simple and convenient way to characterize the changes they see in surface morphology when growth conditions change; (ii) identify a statistical measure of submonolayer growth which identifies whether graphene step-flow growth is limited by nucleation at steps or by propagation on terraces; and (iii) provide physical insight into the competition between graphene strip coalescence and a new kinetic process (unique to this system) which we call "climbover".

Our approach is coarse grained and addresses step flow growth only. Moreover, we confine our attention to vicinal surfaces with triple bilayer steps. As mentioned earlier, this implies that graphene grows in strips parallel to the decomposing SiC step edges and this makes a one-dimensional model a good first approximation. We do not model the buffer layer explicitly, and we do not explicitly model the silicon sublimation from SiC terraces. Rather, our model focuses on the thermal decomposition processes which cause graphene to nucleate at the SiC step edges and to propagate across the SiC terraces. The rates assumed for these processes implicitly include the buffer-layer formation rate, which we assume is always present between the SiC substrate and the most recently formed graphene layer.

5.2.2 Model Description

Figure 14 shows the various processes we consider for a vicinal surface of 6H-SiC composed exclusively of half-unit-cell-height (or triple bilayer) steps. Each process involves the replacement of a unit area of a SiC triple bilayer by a unit area of graphene. Figs. 14(a) and 14(b) show the nucleation of graphene at a SiC step with no graphene nearest neighbors. This occurs in our model at a rate $r_{\text{nuc}} = \nu_0 \exp(-E_{\text{nuc}}/kT)$, where $\nu_0 \approx 10^{12} s^{-1}$ is an attempt frequency and T is the substrate temperature. Two points

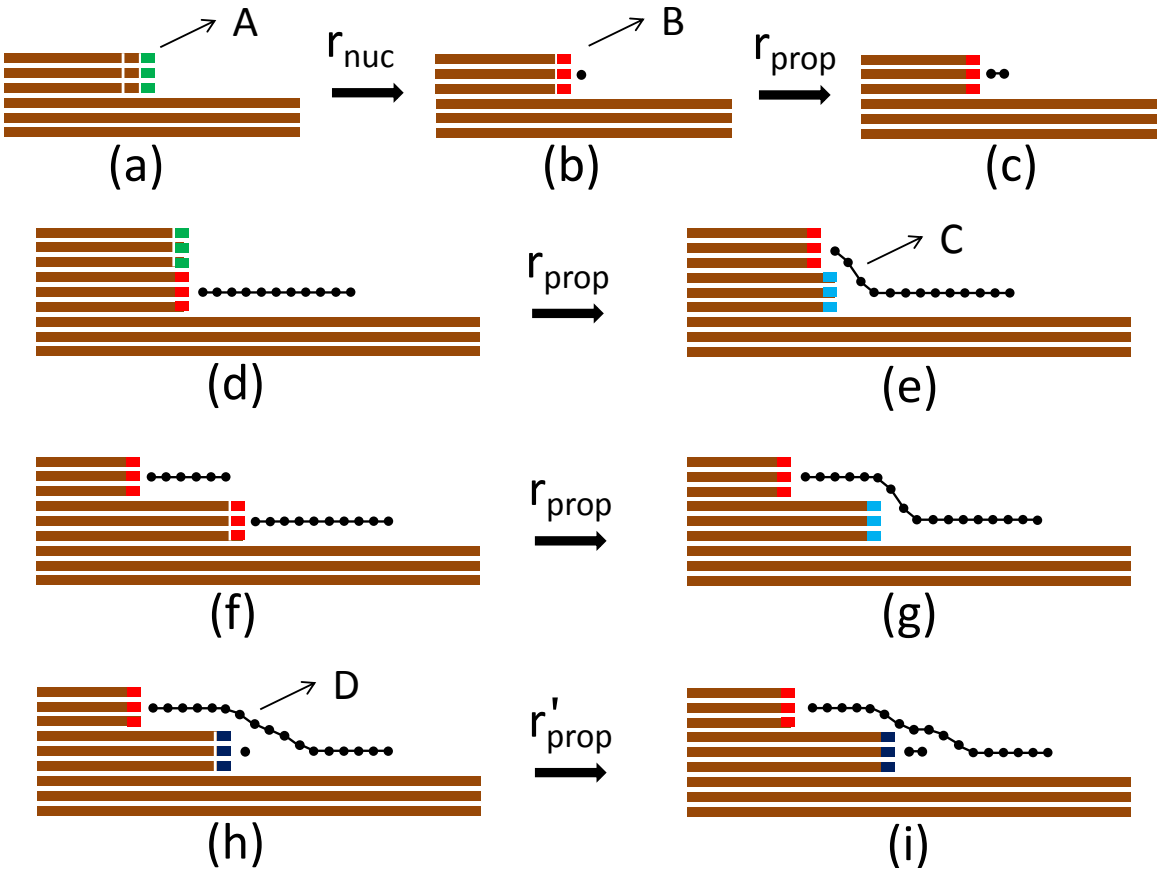

Figure 14: Kinetic processes allowed in the KMC simulation. The steps marked A (green), B (red), C (blue), and D (purple) play a role in the rate theory reported later in this Chapter.

are worth noting. First, E_{nuc} is an *effective* energy parameter which accounts for the combined effects of Si atom sublimation, C atom recrystallization, and graphene growth along the step edge. Second, a variation of our model could allow additional SiC to sublime before a stable graphene nucleus forms. This influences the predicted distribution of strip widths and, like the corresponding distribution of critical island sizes in conventional epitaxial growth, comparison with experimental results provides microscopic information that is nearly impossible to learn any other way [99].

After nucleation, graphene growth continues by dissolution of the adjacent SiC step at a rate $r_{\mathrm{prop}} = \nu_0 \exp(-E_{\mathrm{prop}}/kT)$ [Figs. 14(b) and 14(c)]. Propagation occurs only at SiC steps that are bounded by a graphene strip. Two fates are possible for

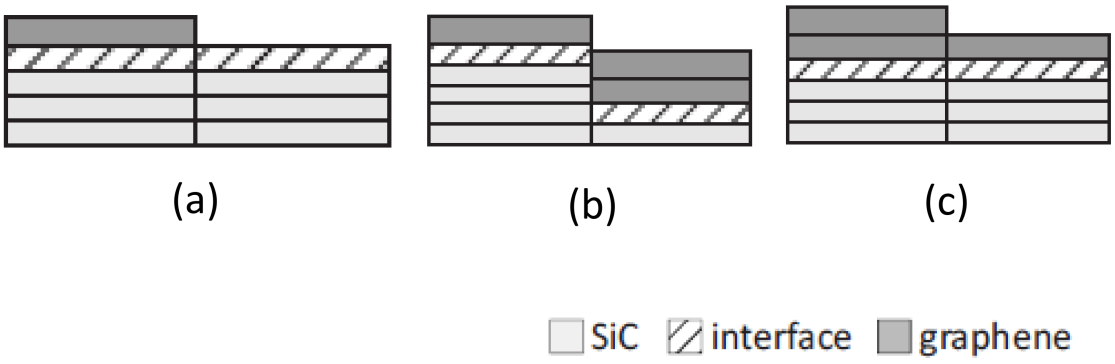

Figure 15: Schematic configurations of SiC triple bilayer steps and graphene layers. Images taken from Fig. 11.

such a strip. One is that the propagating strip runs into another SiC step and creates a step bunch of two triple bilayer steps [Fig. 14(d)]. If this happens, the strip can "climb over" the upper terrace at the rate r_{prop} [Fig. 14(e)]. Another possibility is that the propagating strip meets another strip on the upper terrace [Fig. 14(f)]. In this case, our KMC simulation coalesces the two strips at the rate r_{prop} [Fig. 14(g)]. Nucleation of a covered graphene layer at a covered SiC step occurs at the rate r_{nuc} [Fig. 14(g) and 14(h)]. Propagation of a covered graphene layer occurs at the rate r_{prop} or (for some of the simulations reported below) at the slower rate r'_{prop} [Fig. 14(i)]. The later growth continues in the same way as the first graphene layer.

We recall the step configurations illustrated in Chapter IV (also see Figure 15) to show that our KMC model is consistent with these observations. Fig. 15(a) is identical to the right part of the step in Fig. 14(c), which shows that graphene forms by SiC triple bilayer decomposition. This consistency is also seen for more complicated step configurations, e.g., when we compare Fig. 15(b), 15(c) with the lower step configuration shown in Fig. 14(i). In this case, the thickness variation of graphene layers from 1 to 2 in Fig. 15(b) and 2 to 1 in Fig. 15(c) can be found in Fig. 14(i), and the relative step height differences seen in Fig. 15(b) and Fig. 15(c) are also the same as in Fig. 14(i).

In addition, the coalescence and climbover events that we introduce in the model may be similar to the two different growth mechanisms found for graphene growth on Ru (see Section 3.2.2). When the temperature is increased from 1000 to 1400K, all the step edges are decorated by graphene islands. When these islands become big enough, they coalesce into large islands. However, a slow cooling from 1150 °C to 825 °C results in sparsely distributed nuclei. The subsequent growth proceeds in the downhill direction, and the graphene sheet carpet the substrate steps all the way down the path. This growth mechanism may be considered as the reverse "climbover", in the sense that in both processes one side of the graphene sheet is pinned whereas the other side is free to grow.

We use a standard KMC algorithm [100] to simulate growth on vicinal SiC surfaces composed of (typically) 5000 steps with periodic boundary conditions. We forbid third layer growth for simplicity only. This restriction is not fundamental to either our model or the simulations. The vicinal angle is $\phi = \tan^{-1}(3/W)$, where W is the terrace width. We begin our discussion with Θ_i, the graphene coverage of layer i, as a function of the total graphene coverage $\Theta = \sum_i i\Theta_i$. These quantities are accessible to spatial-averaging experimental probes and our model energy parameters should provide a simple and convenient way for experimenters to characterize variations in observed morphology with growth conditions. Later, we turn to the distribution of graphene strip widths as a quantity which could exploit scanning microscopy to learn the relative importance of competing surface kinetic processes during growth.

5.3 Results and Discussion

5.3.1 A Regular Array of Steps

We tested our model first using a step bunched substrate. Figure 16 compares a high-resolution transmission electron microscope (HRTEM) image of graphene grown on a stepped surface with a portion of a KMC simulation ($r'_{\mathrm{prop}} = r_{\mathrm{prop}}$) beginning

with a regular array of SiC steps, each three unit-cells in height (18 Si-C bilayers). The agreement with experiment is quite good.

In the figure, from the right to the left side (the direction in which graphene growth proceeds), the thickness of the graphene layers changes approximately from five to three. The model predicts that the variation of graphene-layer thickness should correspond to two SiC triple bilayers (Fig. 16(a)), which is about 1.5 nm. This height is also consistent with the HRTEM image shown in Fig. 16(b).

Our main interest is the statistical properties of the first and second layers of graphene grown on a regular array of SiC steps, each one-half unit-cell in height (3 Si-C bilayers). We now turn to results for surfaces of this kind.

5.3.2 Layer Coverage and Growth Time

Figure 17 shows simulation results for Θ_1 as a function of $\Delta E = E_{\rm nuc} - E_{\rm prop}$ with $r'_{\rm prop} = r_{\rm prop}$ for four different values of total coverage Θ and two choices for the vicinal angle ϕ. The rather counter intuitive behavior that Θ_1 *decreases* as ΔE *increases* for fixed Θ can be understood as follows. When ΔE is large, the propagation of existing graphene strips is relatively more likely than the nucleation of new graphene strips, and fewer graphene strips form. Many strips undergo the "climbover" process [Figs. 14(d) and 14(e)] when the widths of the graphene strips pass the terrace width, thereby creating many nucleation sites for second-layer growth. The net result is that nucleation of second-layer graphene begins earlier. Because these strips grow for a longer time, the total second-layer coverage is larger. When ΔE is further increased, the number of nucleation events for both the first layer and second layer are greatly reduced, and eventually the competition between the two layers is balanced. This effect produces the lower plateaus in Fig. 17.

At $\Delta E/kT = 0$, the steps are nucleated almost simultaneously, and only strip coalescence occurs. However, these events do not happen until sufficient surface

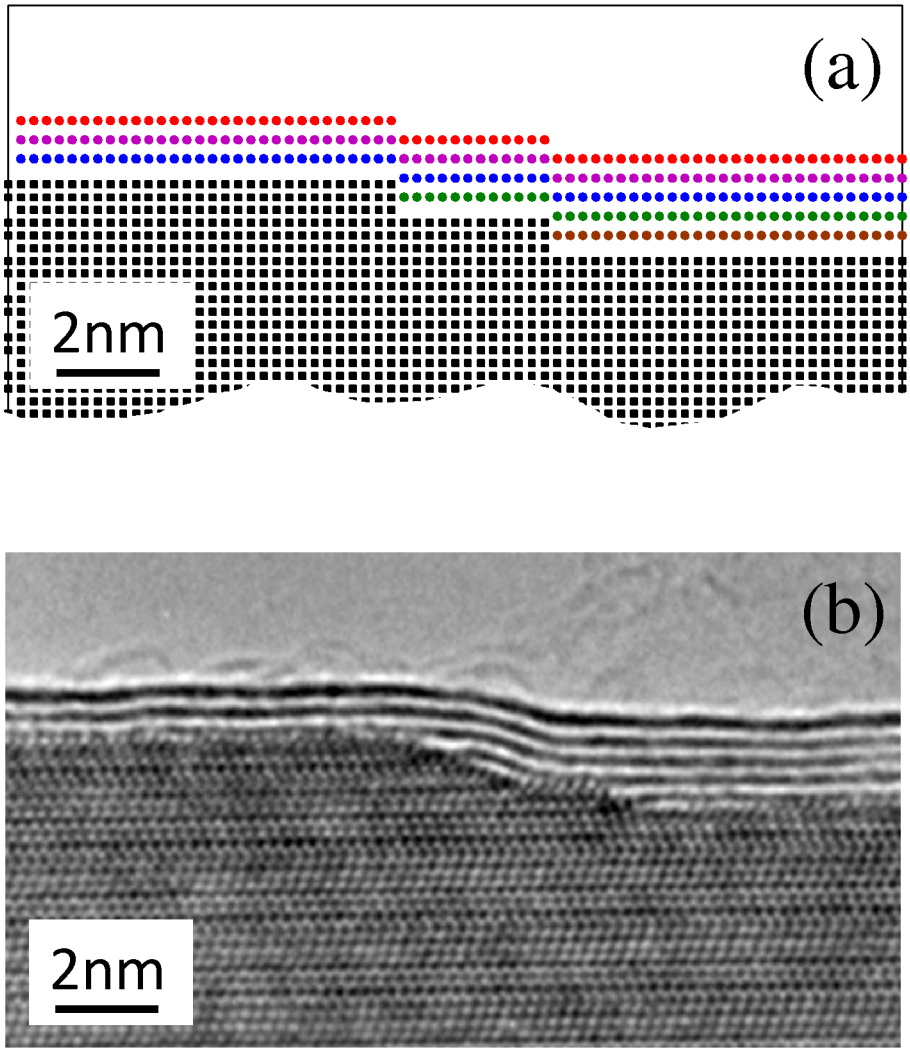

Figure 16: Multilayer graphene grown on a stepped surface: (a) KMC simulation; (b) HRTEM image. In the simulation, the total coverage $\Theta = 2.1$, $\Delta E/kT = 5.2$, and $\phi = 24°$. The TEM image reproduced from Ref. [91].

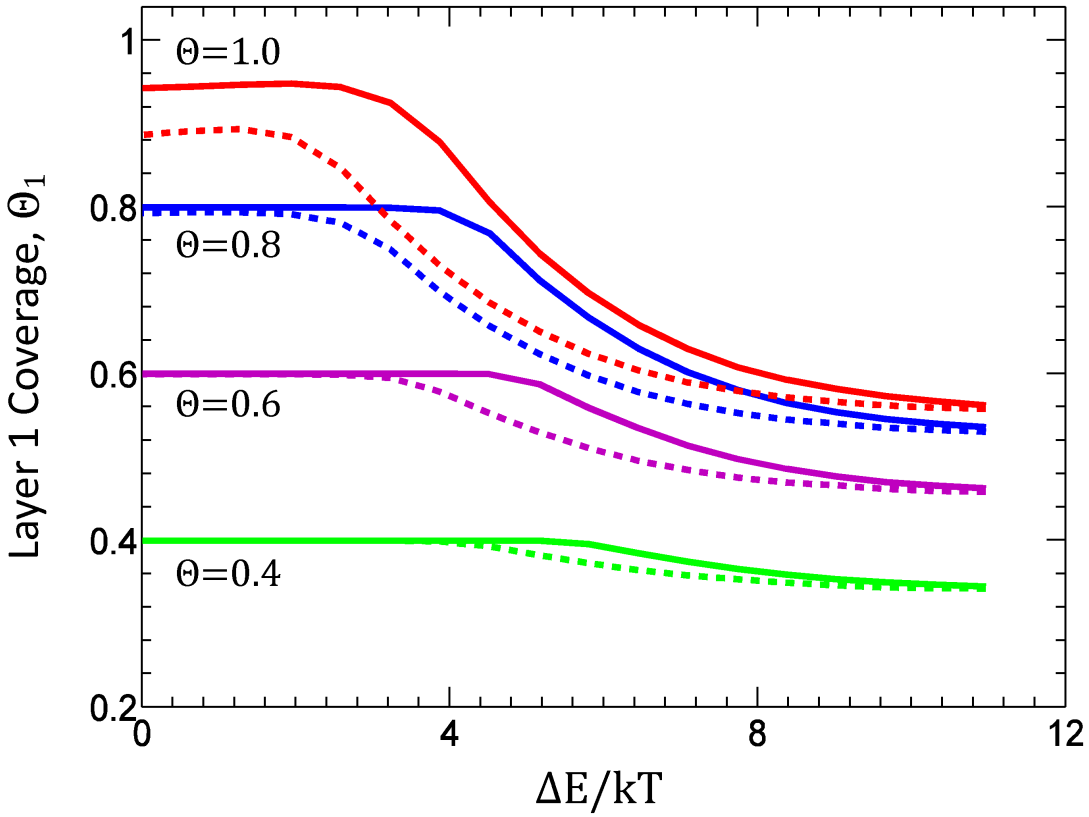

Figure 17: Layer 1 coverage as a function of the energy barrier difference ΔE and vicinality ϕ. Solid and dashed lines correspond to $\phi = 0.9°$ and $\phi = 3.4°$, respectively.

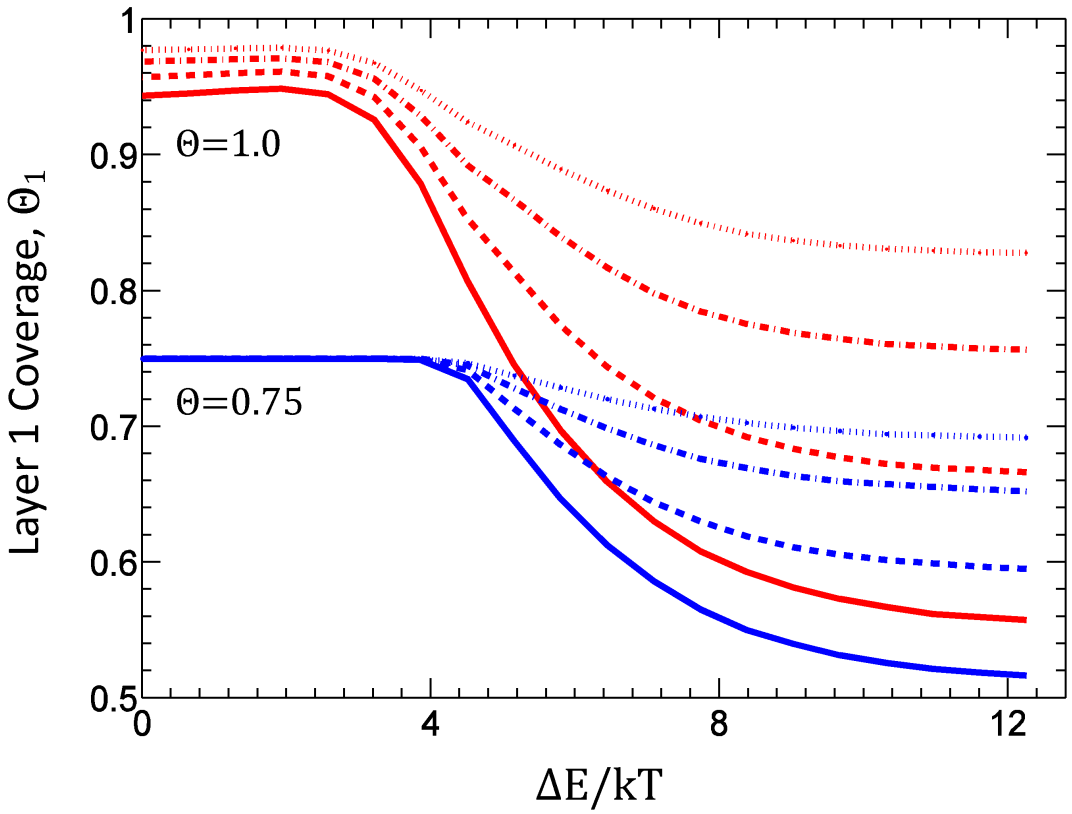

Figure 18: Layer 1 coverage as a function of ΔE for different values of $\Delta E'$. $\Delta E'/kT = 0, 0.6, 1.3$, and 1.9 applies to the solid curves, dashed curves, dashed-dotted curves, and dotted curves, respectively. The vicinal angle $\phi = 0.9°$.

coverage is achieved. That is why $\Theta_1 = \Theta$ in Fig. 17 for smaller values of Θ when $\Delta E/kT = 0$. On the other hand, for $\Theta = 1$, many coalescence events occur in a short amount of growth time. These events create steps which are covered by a continuous graphene layer and thus promote second-layer graphene nucleation. Therefore, Θ_1 is smaller than Θ. The vicinal angle dependence of Θ_1 in this region will be explained later. Fig. 17 implies that better surface homogeneity can be achieved by increasing the substrate temperature and decreasing the substrate miscut angle. This conclusion is consistent with the observations reported in Ref. [92]. A rate equation analysis described later in this Chapter provides another way to understand this behavior of our model.

In principle, experimental data for Θ and Θ_1 can be compared with the curves

in Fig. 17 (outside the plateau regime) to extract a value for ΔE. However, because it is surely harder for Si atoms to escape from SiC when they are covered by a graphene layer than when they are not, we introduce a second-layer propagation barrier $E'_{\rm prop} > E_{\rm prop}$. The corresponding rate for second-layer propagation is $r'_{\rm prop} = \nu_0 \exp(-E'_{\rm prop}/kT)$, and we define $\Delta E' = E'_{\rm prop} - E_{\rm prop}$. For simplicity only, we make the barriers for first- and second-layer nucleation equal.[1]

Figure 18 shows that as $\Delta E'$ increases, the first layer coverage increases substantially, as might be expected. Here, the curves for $\Theta = 0.75$ in the region $\Delta E/kT = 0$, and we see that $\Theta_1 = \Theta$. This is again due to the lack of coalescence as explained in connection with Fig. 17. We now have a three-parameter problem, and experimental data for Θ_1 at two values of total coverage Θ can be used to extract values for ΔE and $\Delta E'$ from Fig. 18.

It remains to deduce values of $E_{\rm nuc}$, $E_{\rm prop}$, and $E'_{\rm prop}$ individually. This can be done using the experimental growth time for a given total coverage because $\tau_K = t_E r_{\rm prop}$ relates the dimensionless KMC simulation time to the experimental growth time t_E. Figure 19 shows τ_K as a function of ΔE for different values of $\Delta E'$. This graph (or a similar one obtained for a different choice of Θ and ϕ) permits $E_{\rm prop}$ to be extracted from the values of ΔE and $\Delta E'$ determined earlier from the layer coverage curves. The two other energy parameters follow immediately.

5.3.3 Strip Width Distribution

We now turn to the distribution of first-layer graphene strip widths. This is the analog of the island size distribution studied in conventional epitaxial growth (see Chapter VII). This statistical quantity probes more deeply into the competition between nucleation and propagation and between coalescence and climbover. It also

[1]Many experiments suggest that the first layer nucleation barrier is small whereas there is finite second layer nucleation barrier. The author thanks Dr. Hannon from IBM T.J. Watson Research Center and Dr. Bartelt from Sandia National Lab for useful discussions. See also Ref. [44].

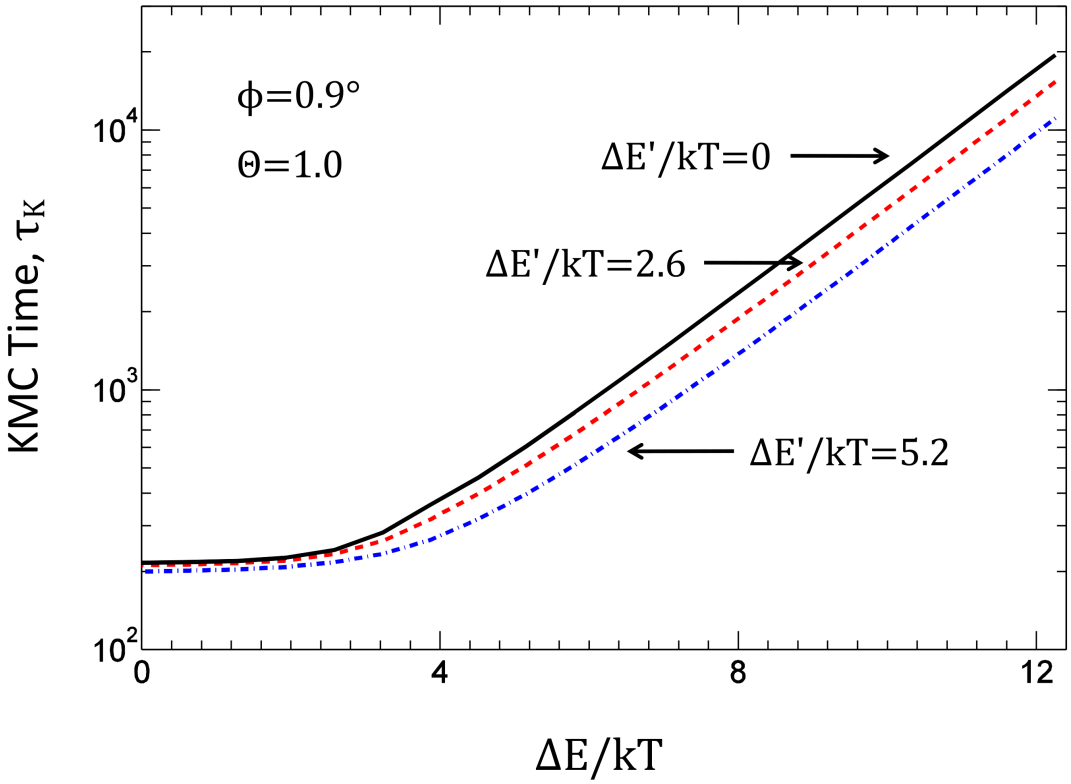

Figure 19: KMC time τ_K as a function of the energy barrier difference ΔE and $\Delta E'$ at a fixed total coverage.

provides another way to extract ΔE and to understand the crossover from the low-ΔE plateau to the high-ΔE plateau in Fig. 17. Compared to the coverage curves, this distribution is much more sensitive to ΔE and much less sensitive to $\Delta E'$. For this reason, we set the latter equal to zero in what follows.

Figure 20(a) shows a LEEM image [10] where the terraces are mostly covered by a single monolayer of graphene (light gray). Very near the step edges, strips composed of two (moderate gray) and three (dark gray) layers of graphene are apparent. Fig. 20(b) shows a KMC simulated morphology (with $\Delta E = 0$) which resembles the second-layer graphene growth in Fig. 20(a). This suggests that effective energy barriers with $\Delta E = 0$ provide a reasonable account of the experimental conditions which produce this type of second-layer graphene growth. Nevertheless, in Fig. 20(a), the third-layer graphene growth is not as uniform as the second-layer graphene. Some steps are covered by the third-layer graphene and some are not. This might be an indication that at least there is a finite nucleation barrier for the third-layer graphene for this growth condition.

According to our simulations, the graphene strip morphology changes significantly as ΔE increases in Figs. 20(c) and 20(d): The number of graphene strips decreases and many of them cover a number of SiC steps. Note also the change in scale from Fig. 20(a). This trend is confirmed by the experimental image shown in Figure 21, which was obtained under very different growth conditions than Fig. 20(a). Fig. 21 shows a few graphene strips of three monolayers (3ML) in a two-monolayer matrix. It closely resembles Fig. 20(d), where some strips cover many SiC steps while some SiC steps do not have any third-layer graphene nucleation.

To quantify the morphological change with increasing nucleation barriers, Figure 22 plots $\rho(s)$, the normalized distribution of strips with width s, for different choices of ΔE and Θ. The terrace width here is $W = 200$. When $\Delta E/kT = 0$ [Fig. 22(a)], the distribution is expected to be Poisson because graphene nucleates at

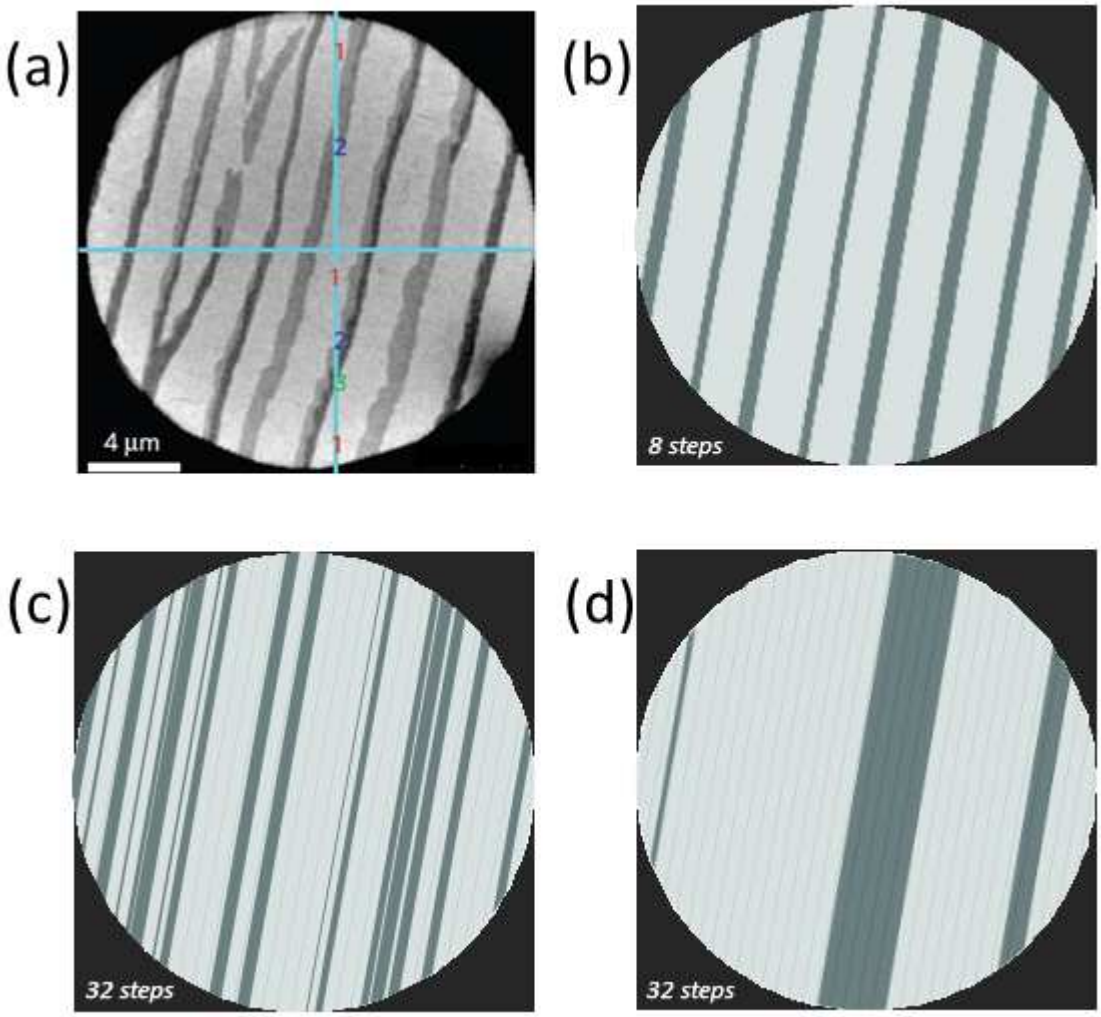

Figure 20: (a) LEEM image of graphene grown on vicinal 6H-SiC(0001) from Ref. [10]. The sample was prepared in a 900-mbar Ar atmosphere at 1650 °C. Regions covered by one, two, and three layers of graphene are shown as light, moderate, and dark gray, respectively. The latter two occur at SiC step edges. (b)-(d), KMC simulation images of monolayer graphene strips with $\Delta E/kT$ = 0, 5.8, and 11.6, respectively. The total coverage Θ = 0.25. Light gray lines and the right edges of graphene strips are SiC steps. The vicinal angle ϕ = 0.9°.

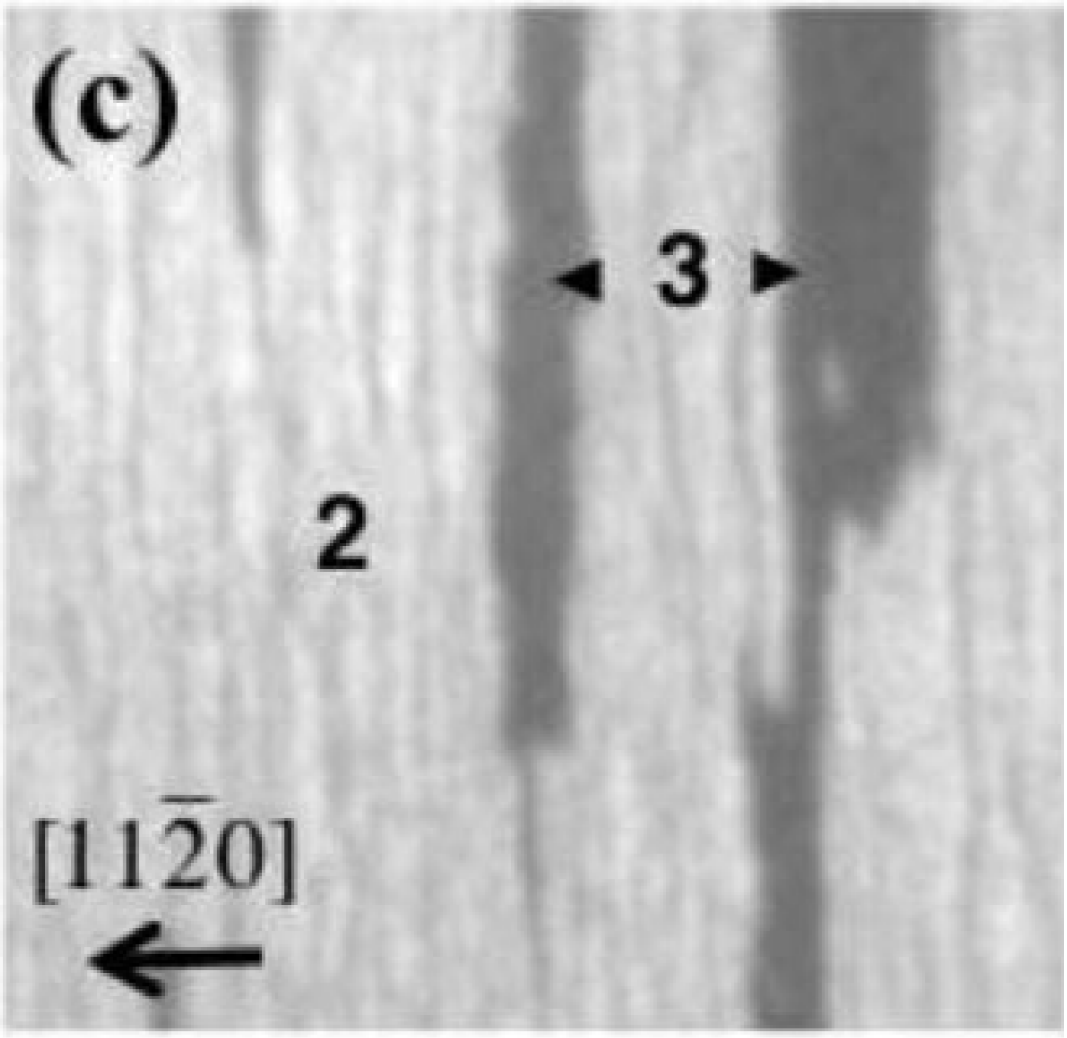

Figure 21: LEEM image of graphene layers annealed at 1600 °C for 600 sec. The numbers on the image indicate the layer thickness of graphene. Gray lines are the step edges. Image adapted from Ref. [15].

almost all the SiC steps simultaneously. We define s_{av} as the average graphene strip width. For low surface coverages, $s_{av} = W\Theta$, which is in the interval $[0, W]$. Figure 23 shows a good agreement between the scaled strip width distribution for $\Theta = 0.1$ and a scaled Poisson distribution (black dashed line) with a mean value $s_{av} = 20$.

In fact, Fig. 23 shows that the $\Delta E/kT = 0$ strip width distributions for $\Theta = 0.1$, $\Theta = 0.3$, and $\Theta = 0.8$ all collapse onto a single curve when scaled by s_{av}. This is reminiscent of conventional epitaxial growth in the submonolayer regime, where the scaled island size distribution also collapse onto a single curve for different surface coverages. However, when the coverage $\Theta > 0.8$ [bottom (blue) line in Fig. 22(a)], the leading edge of the distribution begins to cross the terrace width W, a few strips disappear by the "coalescence" mechanism [Figs. 14(f)-14(g)], and a few strips with widths close to $2W$ form. As a result, the strip width distribution is abruptly cut off at the terrace width, and the distribution repeats (with a much decreased peak amplitude) in the width interval $[W, 2W]$. The distribution moves farther across the terrace width boundary when Θ increases further. Fig. 23 shows that the scaled distribution deviates from the Poisson distribution for $\Theta > 0.8$ (red dashed line).

The general behavior of $\rho(s)$ with increasing coverage persists when the value of ΔE increases. However, a larger value of ΔE implies that some graphene strips nucleate earlier than others. This leads to a shift to the right in the peak position seen in Figs. 22(a)-22(c) for the same coverage. The increasing time delay between consecutive nucleation events similarly produces a distinct broadening of the distribution curves. Eventually, for sufficiently large ΔE, the distribution curves become uniform [Fig. 22(d)] in the scale we consider. This occurs when the graphene strips propagate so rapidly (relative to nucleation) that the step edges are no longer distinguishable. For $\Delta E/kT > 0$, Figure 24 shows that the scaled strip width distribution changes continuously as a function of the surface coverage.

We now return to the vicinal angle dependence of the coverage curves plotted in

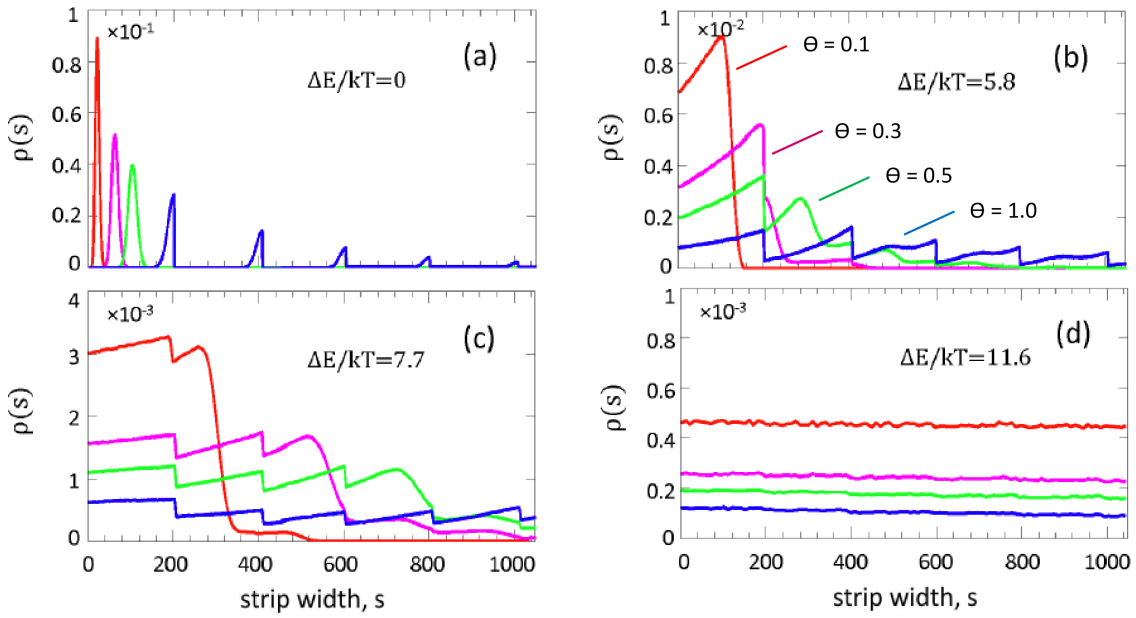

Figure 22: Graphene strip width distribution $\rho(s)$ for different ΔE and total coverage with ϕ = 0.9°. Different color lines correspond to Θ = 0.1 (red), 0.3 (magenta), 0.5 (green) and 1.0 (blue), respectively. The terrace width is W = 200.

Fig. 17. The $\rho(s)$ results imply that the transition between the two horizontal plateaus in these graphs as ΔE increases reflects a transition from a Poisson distribution to a uniform distribution of graphene strip widths. In the Poisson regime, the terrace width affects only the coverage distribution at late times when the maximum graphene strip width passes W. Therefore, a change in the vicinal angle ϕ only changes the coverage distribution for large Θ. This may be contrasted with the uniform regime, where the graphene strips grow so rapidly that they are not hindered by the SiC step edges. In this case, the coverage distribution does not depend on ϕ at all.

Nevertheless, as we see from Fig. 17, for fixed Θ, Θ_1 tends to be larger for smaller vicinal angle ϕ. This is so because the standard deviation divided by the terrace width for a Poisson distribution is $\sqrt{W\Theta}/W \sim 1/\sqrt{W}$, which implies that a smaller vicinal angle leads to a relatively narrower distribution of strip widths. In the limit when all the graphene strips are about the same width, coalescence events occur only

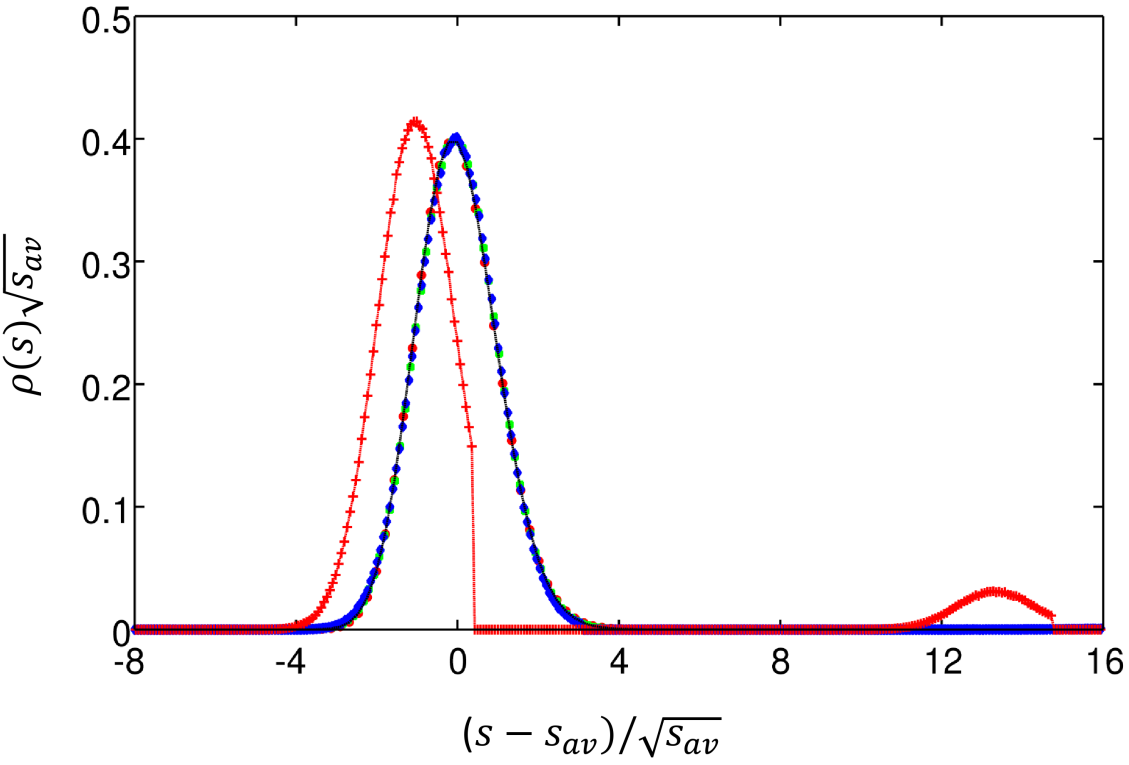

Figure 23: Collapse of scaled strip width distributions for different surface coverages when $\Delta E/kT = 0$. $\Theta = 0.1, 0.3$ and 0.8 for the red $\circ$, green $\square$ and blue $\diamond$ symbols, respectively. $\Theta = 0.9$ for the red dashed line with + symbols. The black dashed line is a scaled Poisson distribution with a mean value of 20.

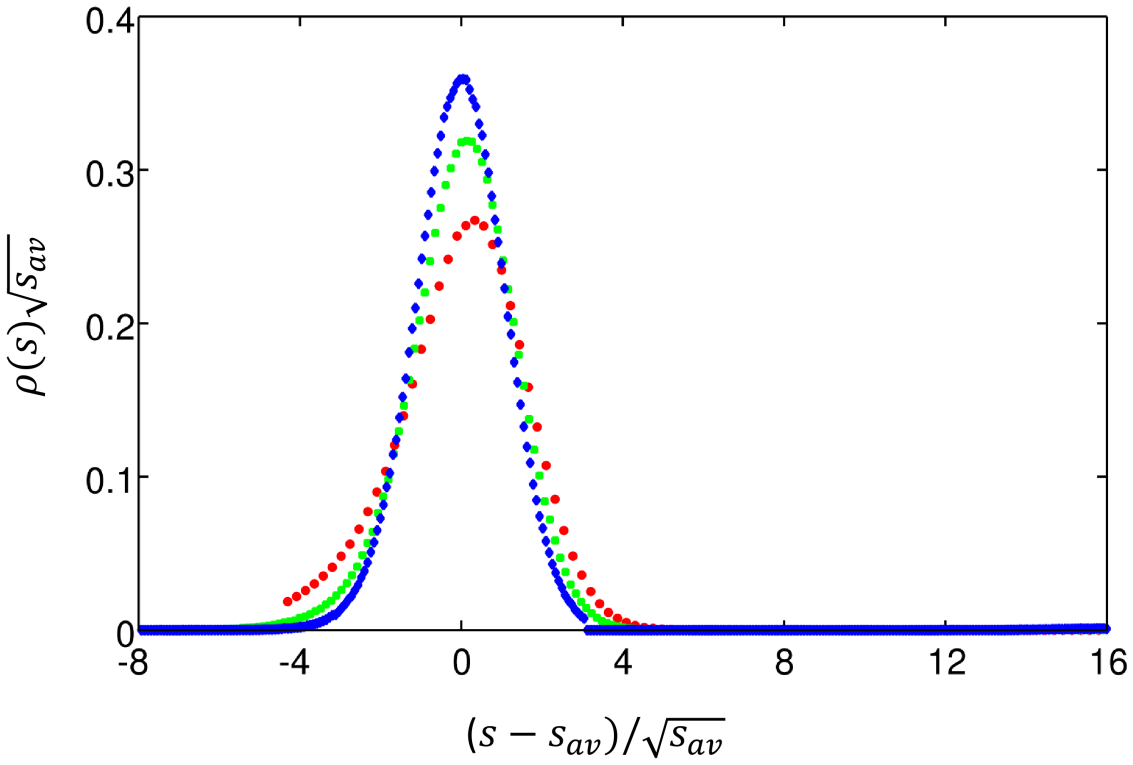

Figure 24: Scaled strip width distributions for different surface coverages when $\Delta E/kT$ = 1.9. Θ = 0.1, 0.3 and 0.8 for the red $\circ$, green $\square$ and blue $\diamond$ symbols, respectively.

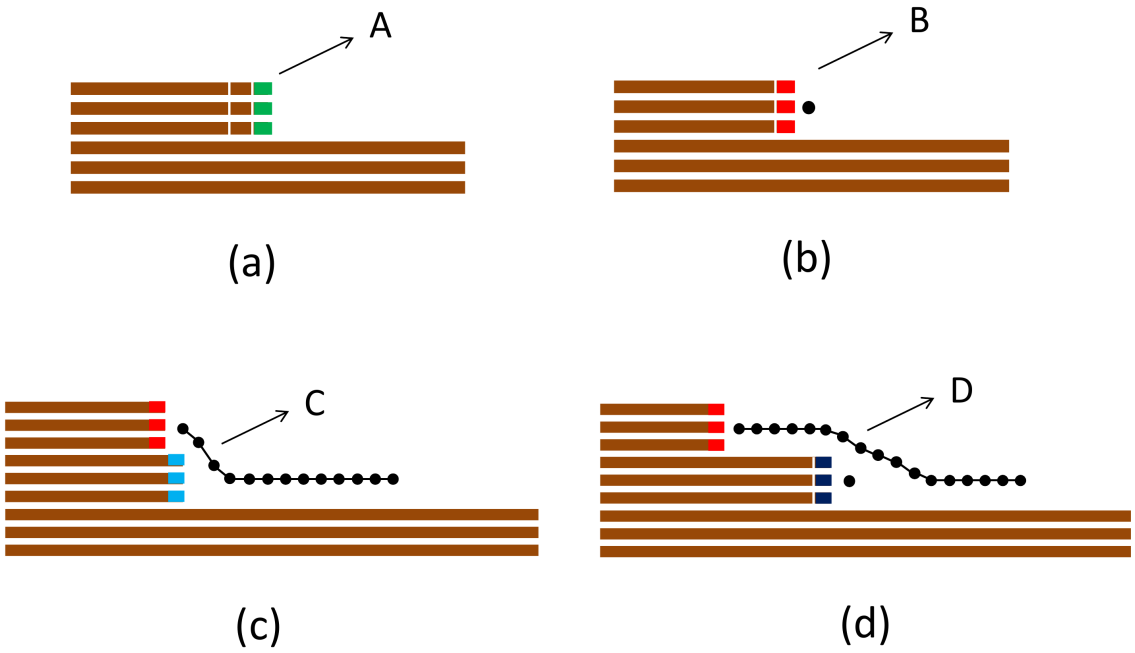

Figure 25: Four types of steps in the KMC model, denoted by A, B, C and D in the figure.

very near $\Theta = 1$ and there is essentially no second-layer growth. This supports our previous statement that better surface uniformity can be achieved by using a more singular surface.

5.4 Rate Equation Analysis

In this Section, we present a mean-field rate-equation analysis to provide further understanding of our graphene growth model. As with our KMC simulations, we model the growth of the first two graphene layers only. It is straightforward to extend the model to study thicker layer growth. The color coding in Figure 25 (reproduced from Fig. 14 in Section 5.3) identifies four basic types of steps in our KMC model: (A) a bare SiC step; (B) a step connected to a layer 1 graphene segment; (C) a step that is carpeted by a continuous layer of graphene; and (D) a step that is connected to a layer 2 graphene segment. For growth of more than two layers, more complicated step types have to be considered in the rate-equation analysis.

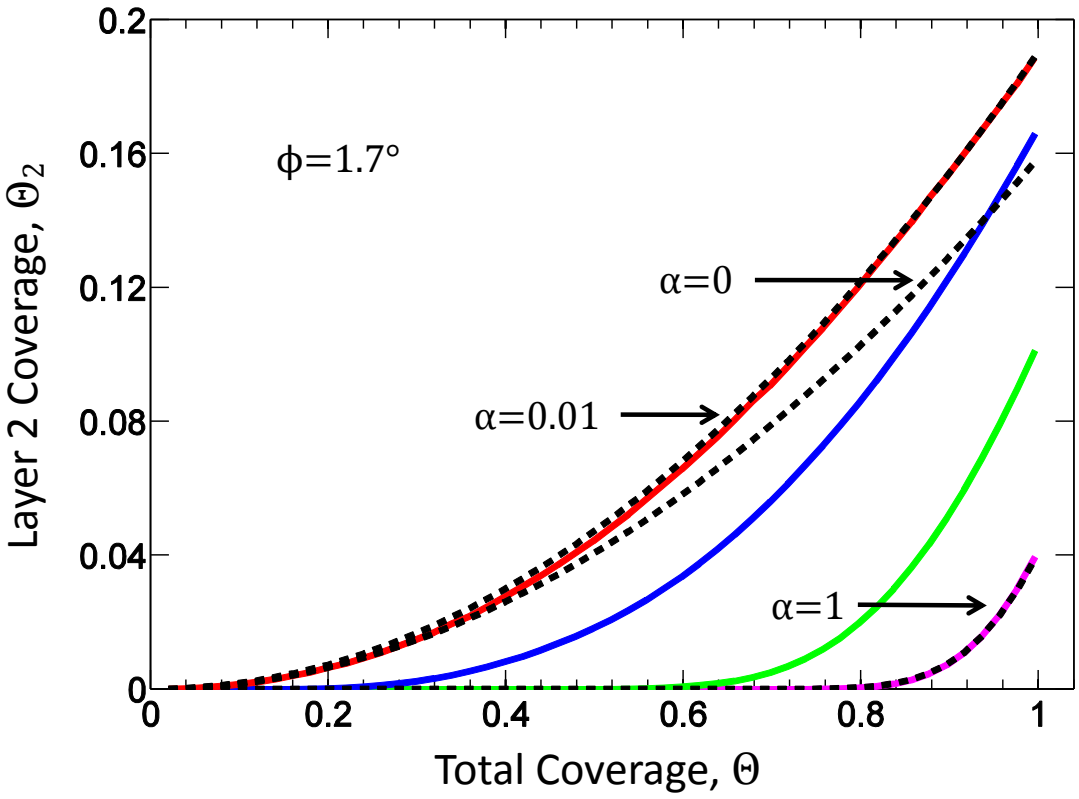

Figure 26: The second layer coverage Θ_2 as a function of the total coverage Θ with $\Delta E' = 0$. The solid lines are KMC simulations with (bottom to top) $\Delta E/kT = 0, 3.9, 5.8$ and 11.6. Dashed lines are the rate equation results.

We let n_A, n_B, n_C, and n_D be the number of steps of each type, so $n = n_A + n_B + n_C + n_D$ is the total number of steps and $L = nW$ is the system size. Then, if $p_d n_B$ is the number of B steps with an A step immediately above [Fig. 14(d)], and $p_f n_B$ is the number of B steps with a graphene segment immediately above [Fig. 14(f)], an approximate description of the epitaxial graphene growth processes is

$$\frac{dn_A}{d\Theta} = -r_1 n_A - r_2 p_d n_B \quad (2)$$

$$\frac{dn_B}{d\Theta} = r_1 n_A - r_2 p_f n_B \quad (3)$$

$$\frac{dn_C}{d\Theta} = -r_1 n_C + r_2 (p_d + p_f) n_B \quad (4)$$

$$\frac{dn_D}{d\Theta} = r_1 n_C \quad (5)$$

where $r_1 = r_{\rm nuc} L/r_{tot}$, $r_2 = r_{\rm prop} L/r_{tot}$, and $r_{tot} = r_{\rm nuc} n_A + r_{\rm prop} n_B + r_{\rm nuc} n_C + r'_{\rm prop} n_D$.

Equation (2) says that A steps (green) are lost by first-layer nucleation events and

by climb-over events. Equation (3) says that B steps (red) are created by nucleation events and lost by coalescence events. Equation (4) says that C steps (blue) are lost by second-layer nucleation events and created by both climb-over and coalescence events. Equation (5) says that D steps (purple) are created by second-layer nucleation events. We note that a climbover event does not change the number of B steps.

We consider two limits where p_d and p_f can be estimated. The first limit is $r_{\rm nuc} \ll r_{\rm prop}$ where first-layer nucleation events are rare. Climbover is frequent and coalescence is infrequent. These conditions imply, in turn, that $p_f \ll 1$ and $p_d \approx 1/W$. The second of these is true because when the coverage is fixed and the propagation rate is fast, the length (modulo W) of the graphene segment connected to a B step takes every value between one and the terrace length W. Conversely when $r_{\rm nuc} = r_{\rm prop}$, nearly every step produces a nucleation event and climbover is rare. This implies that $p_d \ll 1$ and p_f is the probability that the length (modulo W) of the graphene segment connected to a B step is $W-1$ as determined from a Poisson distribution with average value $W\Theta$.

We have solved Eqs. (2)-(5) numerically (assuming $\Delta E' = 0$ for simplicity) in the two limits discussed above using the initial conditions

$$n_A = n \qquad , n_B = n_C = n_D = 0. \tag{6}$$

Using this numerical data, we calculate

$$\frac{d\Theta_1}{d\Theta_2} = \frac{d\Theta_1/dt}{d\Theta_2/dt} = \frac{r_{\rm nuc} n_A + r_{\rm prop} n_B}{r_{\rm nuc} n_C + r'_{\rm prop} n_D} - 1, \tag{7}$$

and use $\Theta = \Theta_1 + 2\Theta_2$ to equate the right side of Eq. (7) to $d\Theta/d\Theta_2 - 2$.

Figure 26 compares Θ_2 versus Θ as determined from the KMC simulation (solid curves) with the correspondingly rate equation results (dashed curves). The agreement is quite good when $\Delta E/kT = 0$ (purple curve). This is the climbover regime where $\alpha = p_f/(p_f + p_d) = 1$. The agreement is similarly good when $\Delta E/kT$ is large (red curve) if we account for coalescence in the rate equations with the choice $\alpha = 0.01$ and

$p_d = 1/W$. The no-coalescence curve ($\alpha = 0$) falls below the $\alpha \neq 0$ curve because, in the rate equations, the presence of coalescence reduces the life-time for all first-layer propagating graphene segments, which reduce the number of competitors to second-layer propagation. Because $\Delta E/kT$ is large, there are not many graphene segments in the system to begin with. Removing some first-layer segments by coalescence promotes second-layer propagation and thus results in a larger second-layer coverage.

5.5 Conclusion

The H_2 etched 6H-SiC(0001) surface usually shows a regular array of SiC steps of triple bilayers. The graphene growth on this type of surfaces can be considered as one dimensional. In this Chapter, we have developed a KMC model to study the epitaxial growth of graphene by the step flow sublimation of such SiC vicinal surfaces. The kinetic processes in the model are consistent with step configurations in experiments. As a test to the model, when applied to SiC step bunched substrates, our model successfully produces a surface morphology similar to a transmission electron microscope image.

For SiC vicinal substrates, the layer coverages and the distribution of graphene strip widths were found to depend more or less strongly on the relative sizes of the effective energy barriers for graphene nucleation, first-layer propagation, and second-layer propagation. The crossover of the distribution from Poisson to uniform as the nucleation barrier increases clearly shows that there are two distinctive growth regimes, one dominated by "coalescence" processes and one dominated by "climbover" processes. The "climbover" processes have the effect of increasing the graphene surface inhomogeneity.

A rate-equation analysis has also been developed based on the correlation between graphene growth and the number of different type of SiC steps on the surface. The

numerical results agree well with the KMC simulations, and provide further understanding of the graphene layer coverages as a result of the competition between the "coalescence" process and the "climbover" process.

When compared to experimental results, our model also provides an effective way to characterize and extract energy barriers from the growth morphology. Our simulation results indicated that more uniform graphene growth can be achieved by using less vicinal substrates at higher growth temperatures, both of which are consistent with experimental observations. It will be interesting to compare these simulation results with experimental measurements to see how the effective energy barriers depend on growth parameters like the partial pressure of silicon in the growth chamber.

For future studies, it is also possible to use this new model to examine the "kinetic roughening" of the epitaxial growth when many graphene layers have been grown[102]. In the next Chapter, we will explore the ability of our model to understand the nonuniform graphene layer thicknesses observed when growth occurs on spontaneous faceted SiC substrates [91].

CHAPTER VI

GRAPHENE ON SIC NANO-FACETS

6.1 Introduction

Besides growth on SiC vicinal substrates, we have mentioned that graphene grows on nano-faceted SiC substrates [10, 92, 90] (see Figure 27). Growth on nano-facets often leads to better quality graphene films on the adjacent terrace [10, 92] and also plays an important role in graphene ribbon growth[61]. By controlling the nano-facet arrangement on a wafer-scale, hundreds of graphene ribbons can be reliably placed on the surface without error.

The purpose in this Chapter is to extend our previous study for vicinal substrates to include growth on nano-faceted substrates. We introduce a model for a SiC nano-facet and add several kinetic processes to our previous model. Our main result is that the original nano-facet is *fractured* into several nano-facets during graphene growth. This phenomenon is characterized by the angle at which the fractured nano-facet is oriented with respect to the basal plane. The distribution of this angle across the surface is found to be related to the strip width distribution for vicinal surfaces.

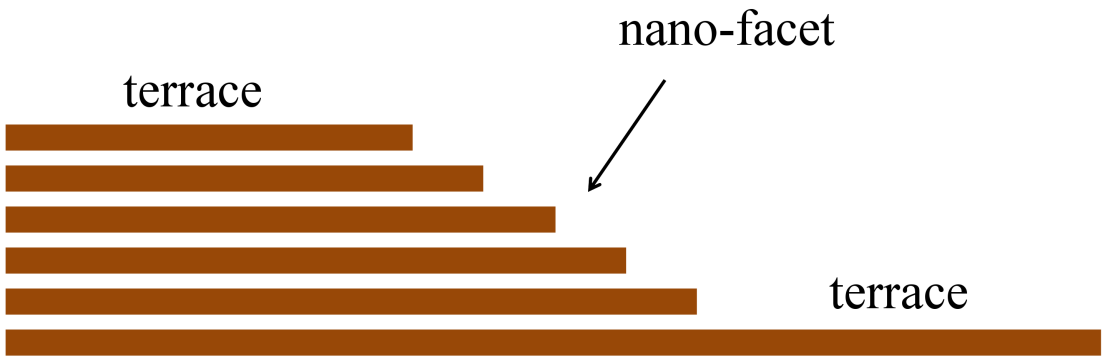

Figure 27: Schematic view of a nano-facet on the SiC substrate.

As the terrace propagation barrier decreases, the fracture angle distribution changes continuously from two-sided Gaussian to one-sided power-law. Using this distribution, it will be possible to extract energy barriers from experiments and interpret this type of growth morphology quantitatively.

6.2 SiC Nano-facet Formation

As discussed in Chapter II, commercially available SiC substrates exhibit rough and scratched surfaces. An effective method to produce atomically flat vicinal surfaces is high temperature H_2 etching. For on-axis 6H-SiC substrates, this method produces vicinal surfaces with triple bilayer steps. This type of microstep formation is related to etching kinetics and energy differences between different basal planes [46]. This contrasts with off-axis 6H-SiC substrates where the H_2 etched surface often shows periodic structures of nano-facets. Depending on whether the substrate is tilted toward the $\langle 1\bar{1}00\rangle$ or $\langle 11\bar{2}0\rangle$ direction, the nano-facet makes an angle of $\approx 25^\circ$ or $13-14^\circ$ from the basal plane [39, 47, 48]. Besides H_2 etching, controlled nano-facets can be achieved by a direct plasma etching of SiC surfaces [61].

Nano-facets can also form spontaneously when SiC is heated close to the graphitization temperature in non-vacuum environments. This type of step bunching is observed for both on- and off-axis SiC substrates. At higher growth pressure, a reduced silicon sublimation rate leads to a higher graphitization temperature. It is likely that at these elevated temperatures, the SiC vicinal surface of triple bilayer steps is further reconstructed into nano-facets to minimize the surface free energy.

The formation of graphene begins at these nano-facets where silicon atoms are less bonded to the substrate [91, 90]. Given the previous discussion, SiC step bunching to produce nano-facets may occur before graphene formation. Our model only considers the formation of graphene on pre-existing nano-facets regardless of their origin. We also neglect the difference between $(1\bar{1}0n)$ and $(11\bar{2}n)$ nano-facets.

6.3 Modeling Growth on Nano-facets

We model a nano-facet as a group of triple bilayer SiC steps with a fixed spacing between adjacent steps (Figure 28(a)). In this case, graphene growth on nano-faceted surfaces proceeds in step flow mode. Therefore, our previous one-dimensional model is a good starting point. The main difference is that nano-facets are observed to have different angles with respect to the basal plane depending on the substrate polytype, orientation of the substrate, and the graphene growth conditions [103, 91, 104, 90]. Adjusting the spacing width in our model allows different initial nano-facet angles.

We assume that growth starts at the bottom of the nano-facet, converting one step into one graphene unit. The nano-facet nucleation process occurs at a rate $r_{\text{nuc}} = \nu_0 \exp(-E_{\text{nuc}}/kT)$ (Fig. 28(a), and28(b)). The nucleated graphene unit propagates upward along the nano-facet at a rate $r_{\text{prop}} = \nu_0 \exp(-E_{\text{prop}}/kT)$ (Fig. 28(b), and 28(c)). We keep the value of $E_{\text{prop}} = 0$ because incomplete graphene coverage on the nano-facet is rarely observed experimentally. In other words, growth on a nano-facet is faster than other kinetic processes.

The nano-facet nucleation and propagation processes defined here are similar to those we defined for vicinal surfaces in Chapter V. As soon as a nano-facet propagation event occurs, a second-graphene layer can nucleate immediately under the first layer (Fig. 28(f)) and the growth of the second layer can continue in the same way as the first layer (Fig. 28(f), and 28(g)). This contrasts with our previous model for vicinal surface growth where a second layer of graphene can only grow at a step covered by a continuous graphene strip (see Fig. 14(h)).

When the propagation on the facet reaches the top junction between the nano-facet and the SiC(0001) basal plane, the graphene growth is allowed to continue on the (0001) basal plane but with a slower propagation rate $r'_{\text{prop}} = \nu_0 \exp(-E'_{\text{prop}}/kT)$ (Fig. 28(d), and 28(e)). This is due to the experimental observation that several layers of graphene often grow on a nano-facet before the graphene growth propagates onto

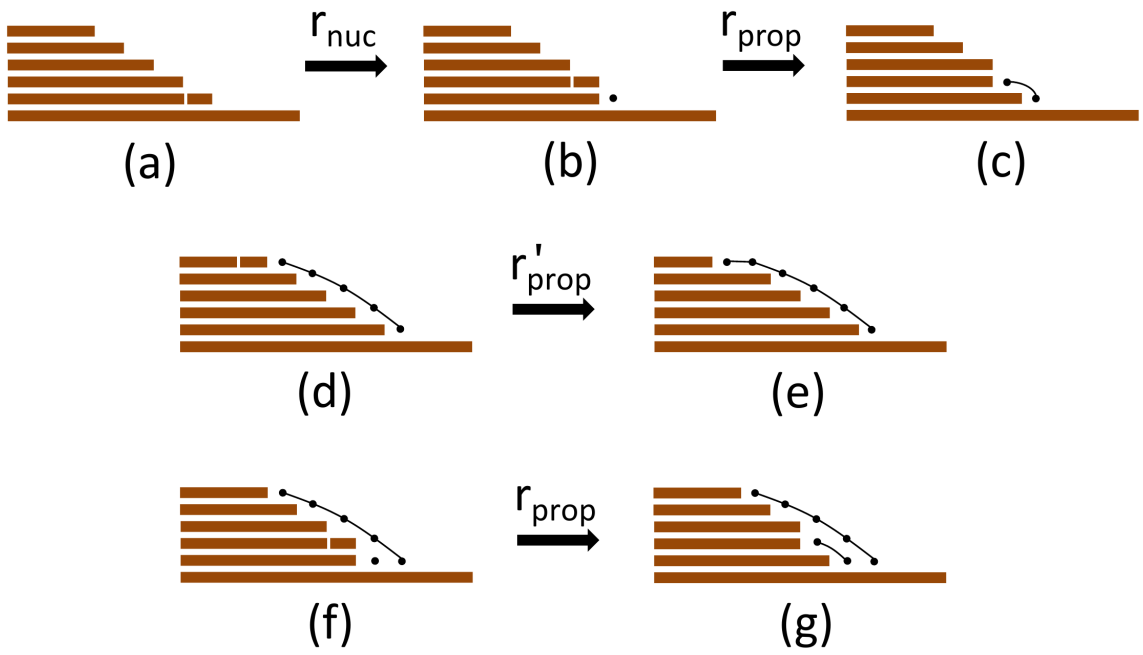

Figure 28: Graphene growth kinetics processes on a nano-facet.

the (0001) basal plane [90]. We focus on the early growth stage where the graphene layers of each macrostep grow independently, and no coalescences or climbovers are allowed.

6.4 Results and Discussion

6.4.1 Surface Morphology and Formation Processes

Figure 29 shows that a particular choice of KMC model parameters produces a simulated morphology similar to a transmission electron microscope image of graphene growth on a non-planar SiC(0001) surface. The TEM image was taken of a sample which was prepared at 1325 °C for 90 min, with step heights of 5 – 15 nm. Both the TEM and the simulation image show a sharp ending for all graphene layers at the bottom of the nano-facet, where the graphene growth starts. Fig. 29 also shows that, from the left to the right side, graphene layers grow continuously over the junction between the high index nano-facet and SiC(0001). The top-graphene layer is the longest, while the other layers have a similar length. In what follows, we call all the

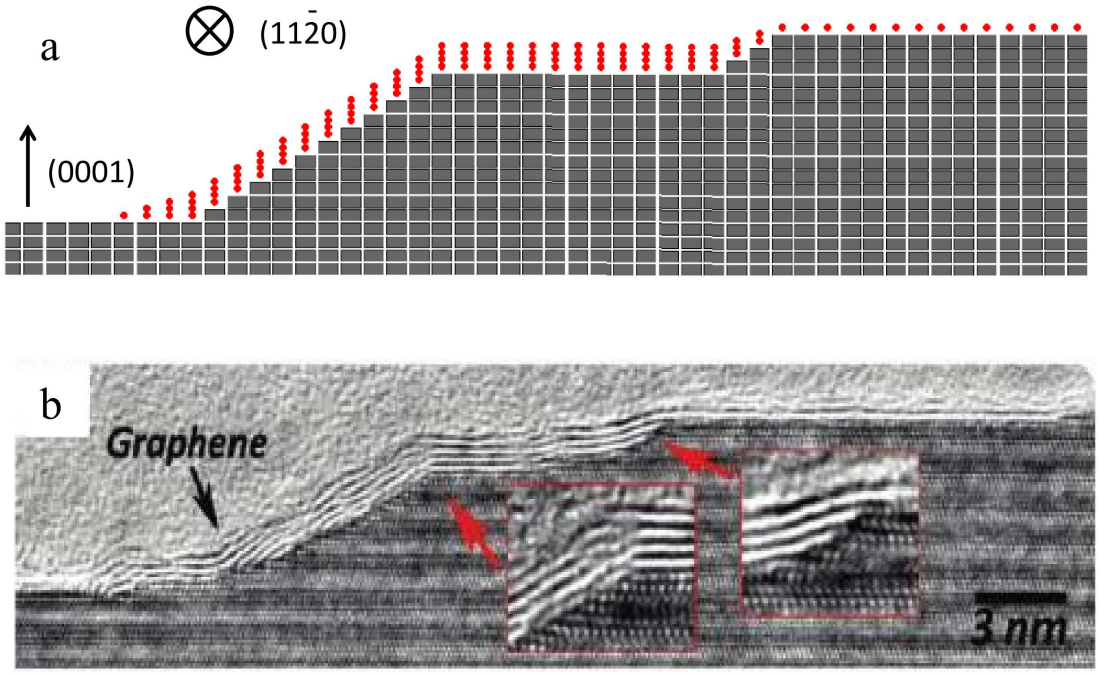

Figure 29: (a) KMC simulation snapshot. Total surface coverage Θ = 0.8, T = 1800 K, E_{nuc}/kT = 7.7, E'_{prop}/kT is 3.9 and 7.1 for the top-graphene layer and the interface-graphene layers, respectively. (b) Transmission electron microscope image adapted from Robinson et al. [90].

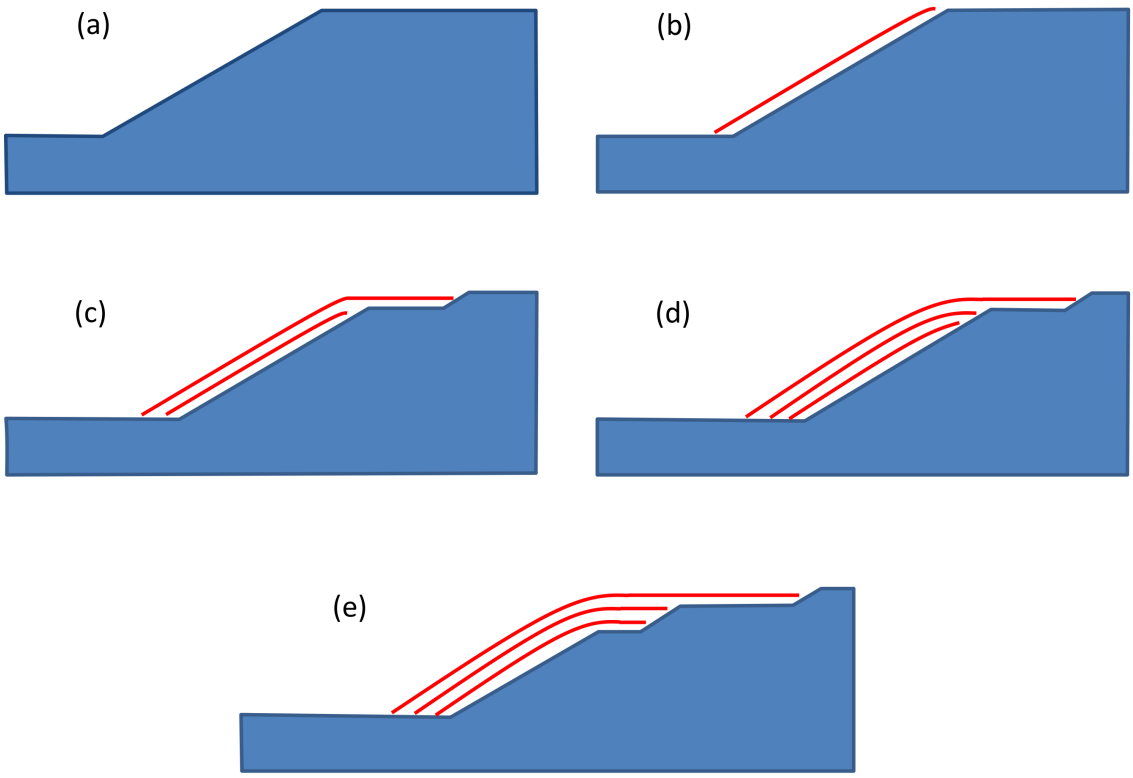

Figure 30: Formation processes for the surface morphology in Fig. 29.

graphene layers other than the top one "interface-graphene layers".

Figure 30 illustrates the formation process for the surface morphology in Fig. 29. The original nano-facet is shown in Fig. 30(a). The first-graphene layer nucleates at the bottom junction of the nano-facet, and propagates quickly up the slope until it reaches the top basal plane. This is shown in Fig. 30(b). Fig. 30(c) shows that the first-graphene layer continues to grow onto the terrace and a small triple bilayer nano-facet is fractured from the original nano-facet (This process was previously shown in Fig. 28(d), and 28(e)). However, the terrace propagation rate is slower than the nano-facet propagation rate. Therefore, Fig. 30(c) also shows that the first-graphene layer cannot grow very long on the terrace before the second layer is nucleated under the first layer and quickly covers the lower nano-facet.

The terrace propagation rate for the second-graphene layer is slower than the first layer due to the increasing difficulty for Si atoms to escape from SiC steps covered

by graphene. This leads to a possible scenario, shown in Fig. 30(d), that before the second-graphene layer grows on the terrace, a third-graphene layer is nucleated and catches up to the second layer growth at the top of the lower nano-facet. Later, when the second-graphene layer does grow onto the terrace like the first layer, another triple bilayer step is decomposed from the lower nano-facet. This process is the same for the third layer. However, assuming that the second- and third-graphene layers have a similar terrace propagation rate, Fig. 30(e) shows that a nano-facet of one unit cell high is fractured from the original nano-facet by growing the second- and third-graphene layers together on the terrace.

Two small nano-facets are now fractured from the original nano-facet, with heights corresponding to one and two triple bilayer steps, respectively. This is the same type of surface morphology seen in Fig. 29(b). We note that, in our model, graphene grows by decomposing SiC triple bilayer steps, so the graphene layer always has one side attached to a nano-facet. To emphasize this, in Fig. 30, we draw the graphene layers as slightly curved at the top of a nano-facet.

6.4.2 Fracture Angle Distribution

To quantify the surface morphology, we study the fracture angle θ made by the graphene layers on the nano-facet with respect to the basal plane. In the simulations, θ is quantified as follows (see Figure 31). If the nano-facet height is h, we count the number of units from the edge of the top terrace (marked as letter A in Fig. 31) to the edge of the bottom terrace (letter B in Fig. 31), and define the length as L (e.g. $L = 5$ in Fig. 31). Then $\theta \equiv \arctan\left((h+1)/L\right)$. The initial θ in the simulations is assumed to be $\theta_0 = 30°$, which is close to the nano-facet angle observed experimentally.

As soon as the top-graphene layer growth propagates onto the terrace, θ starts to decrease as a function of the growth time. Hence, we can use θ to characterize the nano-facet fracturing process due to graphene growth. θ can be measured directly by

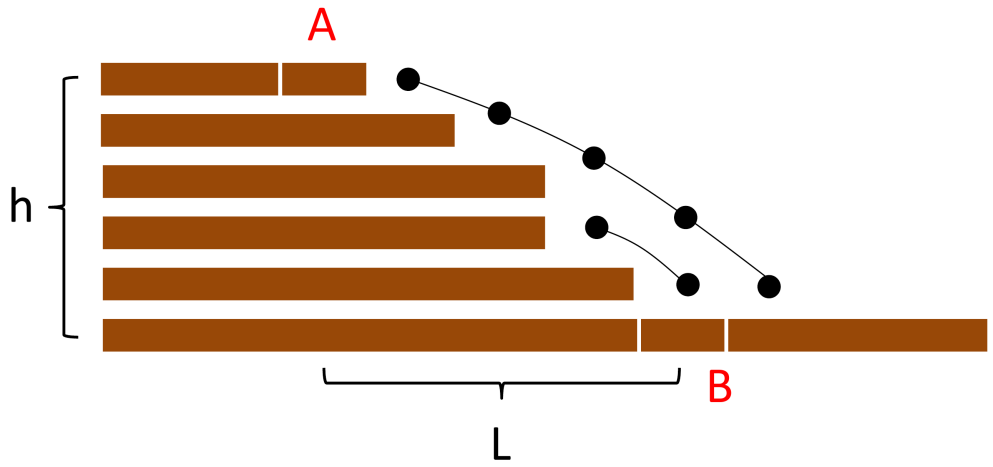

Figure 31: Computation of the fracture angle θ using the blocks specified by the letters A and B.

experiments using the definition above. Compared to experimental results, the KMC simulation can be used to provide some quantitative information about the nucleation and propagation barriers.

The initial surface for our statistical study of growth-induced fracturing is a periodic sequence of basal planes and nano-facets. We fix the height of the nano-facets to be 22.5 nm, which corresponds to $h = 30$ SiC triple bilayers. We use a long terrace width and a short total growth time so that no graphene strip coalescence occurs. For statistical purposes, the surface consists of 6×10^4 alternations of SiC(0001) and nano-facets, with a vicinal angle $\phi = 5.7°$. The growth temperature is fixed at 1800 K. We also fix the nucleation barrier $E_{\text{nuc}}/kT = 7.7$ and treat the terrace propagation barrier E'_{prop} as the only variable.

We now focus on the distribution of fracture angles at a given coverage. For simplicity only, we assume the energy barriers for all graphene layers are the same. Figure 32 shows the distribution $\rho(\theta)$ of the normalized fracture angle $\tan(\theta)/\tan(\theta_0)$ for different choices of terrace propagation barriers E'_{prop} with a fixed total coverage $\Theta = 0.5$. If we define $\Delta E_f = E_{\text{nuc}} - E'_{\text{prop}}$, it is clear from Fig. 32 that the distribution of fracture angles shows cross-over behavior as ΔE_f increases. For $\Delta E_f = 0$, it is

difficult for graphene to propagate on the terrace. After all the nano-facets are fully covered by graphene, growth on the terraces begins almost simultaneously. This leads to a Gaussian distribution of fracture angles in Fig. 32. This growth regime is similar to graphene growth on vicinal surfaces for $\Delta E = 0$, where all the steps are nucleated at the same time and a Poisson strip width distribution is found.

More interestingly, as ΔE_f increases, Fig.32 shows that the distribution of fracture angles becomes more and more one-sided. Eventually, when $\Delta E_f = 5.8$, the distribution follows an intriguing power-law form, in which the probability is zero for θ values smaller than the minimum θ given in the figure. We do not fully understand the power-law probability distribution. Nevertheless, the change in fracture angle distribution can still be related to the strip width distribution for vicinal surfaces in Fig. 22. For growth on vicinal surfaces, when the nucleation barrier is high, graphene is nucleated at some steps much earlier than at the others, leading to a shift of peak position to the right side in the strip width distribution (Fig. 22(b)). In other words, longer strips start to dominate the distribution. Similarly, for growth on nano-facets, when $\Delta E_f > 0$, the nano-facets are fractured one after another in a wide time range. In the regime where ΔE_f is big enough, the distribution is dominated by smaller values of θ made by longer top graphene layers. This leads to a one-sided distribution of θ.

Given the above discussion, similar to the strip width distribution, the cross-over behavior of the fracture angle distribution can be considered as a competition between the nucleation process at the nano-facet and the propagation process on the terrace. When compared to experimental observations, the fracture angle distribution can be used to determine ΔE_f.

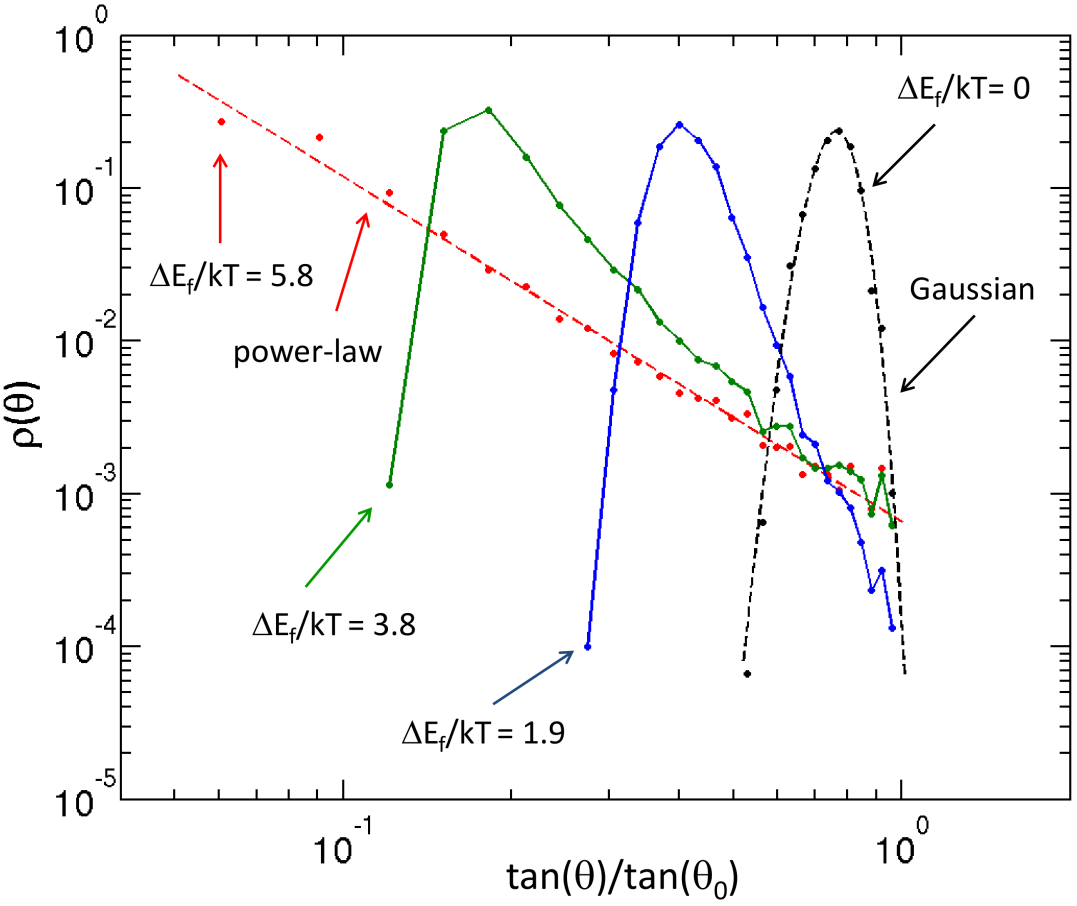

Figure 32: Fracture angle distribution for different terrace propagation barriers. The red dashed line is a power-law fit. The black dashed line is a Gaussian fit.

6.4.3 Effective Terrace Propagation Barrier

We define θ_m as the most probable θ in the fracture angle distribution. In the following, we give a simple analytic treatment to show how θ_m evolves as a function of the growth time. We define the total experimental growth time t_E and the initial growth time t_i spent on the nano-facet before the terrace growth occurs. Assuming $t_E \gg t_i$, the length of the top-layer graphene on the upper terrace is approximately $\nu_0 t_E \exp(-E''_{\text{prop}}/kT)$, where E''_{prop} is an effective terrace propagation barrier. Using the definition of h and L in Fig. 31, we have $L \leq h{+}1{+}\nu_0 t_E \exp(-E''_{\text{prop}}/kT)$. Therefore, the normalized θ_m is given by

$$\frac{\tan(\theta_m)}{\tan(\theta_0)} = \frac{h+1}{h+1+\nu_0 t_E \exp(-E''_{\text{prop}}/kT)}. \tag{8}$$

To derive this equation, it is clear that we do not consider t_i, which gives a small reduction to t_E in Equation. 8. E''_{prop} accounts for both the top-graphene layer terrace propagation barrier E'_{prop} and the nucleation barrier for interface-graphene layers. Increasing the number of interface-graphene layers will reduce the relative horizontal distance between the top and the bottom terraces at the fractured nano-facet (i.e. the horizontal distance between block A and B in Fig.31). Both the initial growth time spent on the nano-facet and the nucleation of interface-graphene layers have the effect of increasing θ. Therefore, it is expected that $E''_{\text{prop}} > E'_{\text{prop}}$. We treat E''_{prop} as a fitting parameter for our analytic model to see how it is related to E'_{prop}.

Figure 33 shows the simulation result for the normalized θ_m as a function of the KMC time τ_K for different choices of terrace propagation barriers. Here we define $\Delta = E'_{\text{prop}}/kT$. The KMC time is defined as $\tau_K = t_E r_{prop}$. Dashed lines are fitted curves according to Eq. 8. Despite the simplicity of Eq. 8, the model curves agree quite well with the KMC simulations for smaller Δ and later growth times. This is likely caused by the adjustment of initial growth time spent on the nano-facet. Smaller Δ indicates a faster graphene propagation on the terrace, which leads to

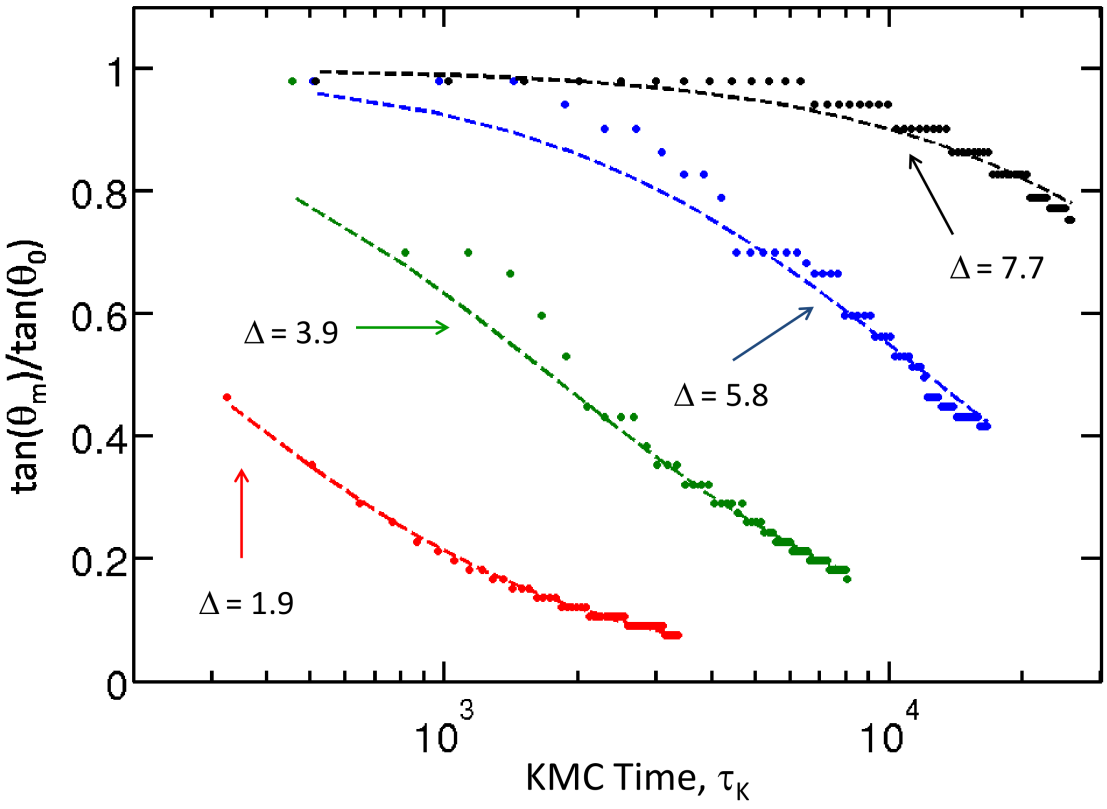

Figure 33: θ_m as a function of KMC time. Dashed curves are the fit results according to Eq. 8. Red, green, blue and black dashed curves give E''_{prop}/kT = 2.1, 4.0, 6.0 and 8.0, respectively.

a relatively shorter growth time spent on the nano-facet before the terrace growth occurs. Similarly, at later growth times when the initial growth time on the nano-facet becomes insignificant, the fitted curve also agrees better.

As we increase the terrace propagation barrier E'_{prop}, the fitting parameter E''_{prop} is also found to increase. This is shown in Figure 34. In fact, we find an excellent linear relationship between E'_{prop} and E''_{prop}: $E''_{\text{prop}} = E'_{\text{prop}} + 0.03$ eV. The relatively small correction to E'_{prop} suggests that the major contribution of E''_{prop} still comes from E'_{prop} for the top-graphene layer. The contribution from the nucleation barrier for interface-graphene layers acts as an additional energy barrier $\Delta E_{\text{prop}} = 0.03$ eV. Therefore, with Eq. 8, the time evolution of the fracture angle θ_m measured in an experiment can be used to obtain a good estimate of E'_{prop}. Combined with the result for ΔE_f from the analysis of fracture angle distribution, both E_{nuc} and E'_{prop} can be extracted experimentally.

Most experiments of graphene growth on SiC nano-facets are done at a temperature between 1600 K and 1800 K. We tested ΔE_{prop} in this range, but no temperature dependence was found. ΔE_{prop} also does not seem to be dependent on the original nano-facet height h. As we increase the nano-facet height from 22.5 nm to 100 nm, the change of ΔE_{prop} is less than 10%, well within the accuracy of E''_{prop} as obtained from Fig. 33. The effects of the growth temperature and the nano-facet height are also shown in Fig. 34. This suggests that ΔE_{prop} is only a function of the energy barriers in the model, and weakly dependent on the growth temperature or the initial nano-facet height in the experimental parameter range.

6.5 Conclusion

Graphene growth starts at SiC nano-facets where more dangling bonds are present. Controlling the nano-facet arrangement either by using etched patterns or furnace

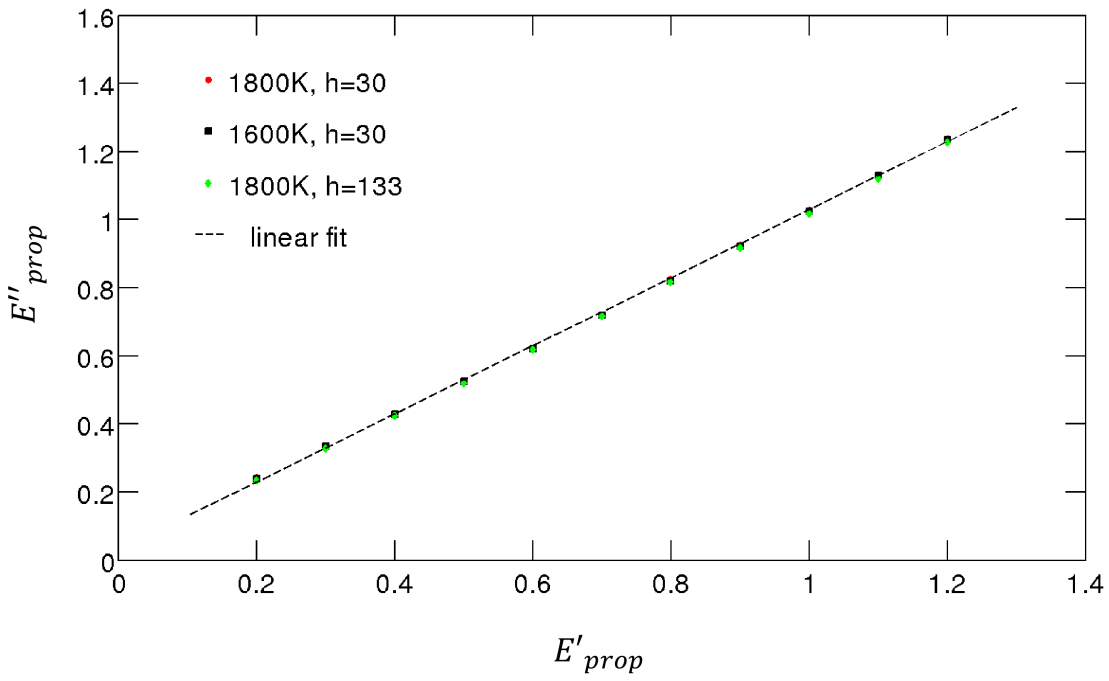

Figure 34: Effective propagation energy barrier E''_{prop} as a function of terrace propagation barrier E'_{prop}, when the growth temperature and the nano-facet height are varied. The linear fit is given by $y = x + 0.03$.

processes provides a cheaper and more reliable solution to produce graphene narrow ribbons. Interesting transport properties have been found for these quasi-one-dimensional ribbons [61]. Therefore, there is practical interest in understanding the formation mechanism of graphene growth on nano-faceted SiC substrates.

In this Chapter, we have presented a model for graphene growth on non-planar nano-faceted 6H-SiC substrates based on our previous model of growth on vicinal substrates. The simulation produces a surface morphology similar to experimental observations. A description of the formation process for this type of surface morphology is provided.

For graphene growth on nano-faceted SiC substrates, a fracture angle can be used to characterize the growth-induced fracture of a nano-facet. The distribution of fracture angles is related to the graphene strip width distribution for growth on vicinal substrates. As the terrace propagation barrier decreases, the fracture angle distribution deviates from a Gaussian and eventually becomes a power-law.

The analytic result for the most probable fracture angle as a function of growth time agrees well with the KMC simulations. The difference between the fitting parameter and the real terrace propagation barrier is insignificant and mostly comes from the nucleation of interface-graphene layers. Therefore, the fitting parameter obtained from experimental results is a good estimate of the real terrace propagation barrier. We also found that this additional energy barrier is relatively insensitive to the growth temperature and initial nano-facet height.

CHAPTER VII

PHASE FIELD MODEL OF SUBMONOLAYER EPITAXIAL GROWTH

7.1 Introduction

This thesis has been focused on the epitaxial growth of graphene on SiC substrates by sublimation. However, it was pointed out in Section 3.2.2 that graphene is also grown on metals using conventional deposition methods. The purpose of this Chapter is to examine the ability of the so-called *phase field method* to model conventional epitaxial deposition in the submonolayer regime [105]. The submonolayer regime is particularly interesting because (i) comparison between experiment and theory can be used to extract diffusion and adatom detachment barriers and (ii) the kinetics of submonolayer growth is replicated in the subsequent multilayer regime [99].

The KMC simulations and rate equations introduced earlier in this thesis have been widely used to study conventional epitaxial growth. The KMC simulations are stochastic and provide a visualization of the growth morphology. On the other hand, as a mean-field approach, the rate equations are computational efficient. A desire to combine their advantages led to the development of the continuum level set method (LSM) [106, 107]. It has been shown that the level set method is able to reproduce the results of KMC simulations for both submonolayer total island densities and island size distributions [108, 109]. Therefore, the level set method is consistent with other theoretical approaches.

A recent paper by Yu and Liu [110] approached the submonolayer problem using a phase field method. Phase field modeling is a continuum approach to the kinetics of phase transformations which makes no use of atomistic information. For that reason,

it is widely used to study evolution phenomena over large length and time scales which are inaccessible to other methods [111]. When applied to the problem of step flow growth in the limit of a thin interface (between the solid and its vapor), the phase field model reduces to the classic step flow model of Burton et al. (BCF) [112] Yu and Liu wrote down a phase field model to study the density of islands in the submonolayer regime. They reported that this quantity scaled with the deposition flux F and the adatom surface diffusion constant D as $N \propto (F/D)^{1/3}$. This is the expected result in the irreversible aggregation regime where island nucleate when two atoms collide and there is no detachment of atoms from island edges.

We tried to reproduce the island density results of Ref. [110] and to extend them to study the distribution of island sizes in the submonolayer regime. It turned out that our results differed from theirs in an interesting way which, we believe, demonstrates some of the virtues and some of the defects of the phase field method applied to this particular problem.

Our main result is that the island size distribution shows scaling behavior. When the capillary length is small, the island size distribution is consistent with irreversible aggregation kinetics. As the capillary length increases, the islands size distribution reflects the effects of reversible aggregation. The results agree quantitatively with KMC and LSM simulations and with experimental data. The total island density scales with D/F, but the exponent is not $\frac{1}{3}$, nor does it change when the scaled island size distribution changes shape. The scaling of the island total density also does not agree with known results. The reasons are traced to the mechanisms of island nucleation and aggregation in the phase field model.

7.2 Calculation Method

7.2.1 Analytical Model

The phase field model of Yu and Liu [110] uses two dimensionless variables, the adatom concentration u and the order parameter (surface profile) ϕ. These are coupled by the evolution equations:

$$\frac{\partial u}{\partial t} = D\nabla^2 u - \frac{\partial \phi}{\partial t} + F + \eta \tag{9}$$

$$\frac{\partial \phi}{\partial t} = \frac{1}{\tau}\{W^2\nabla^2\phi - 2\sin(2\pi\phi)$$

$$- \lambda(u - u_{eq})[2\cos(2\pi\phi) - 2]\} + \lambda_n D u^2. \tag{10}$$

In Equation (9), the first term models the surface diffusion of adatoms. The second term models mass exchange between the adatom population and the steps. The third term is the mean deposition rate, and the last term is a random variable which determines the points on the surface where deposited atoms land. In Equation (10), the term $2\sin(2\pi\phi)$ identifies the terraces of the step profile with integer values of ϕ. The term $W^2\nabla^2\phi$ determines the width W of the step which connects adjacent terraces and the term proportional to $u - u_{eq}$ causes the boundary of an island to move by the capture or release of adatoms. The final term in Eq. (10) is a rate-equation estimate of the island nucleation rate.

Figure 35 shows the different types of island morphology and their corresponding phase field representations using ϕ and u. It is clear from the figure that the sharp island-step profile is mimicked by the continuous order parameter function ϕ. The adatom concentration is always lowest at the center of the islands, and increases away from the islands.

To discuss our choice of parameters, we recall the "thin-interface" limit of the phase field model [113]. This limit defines a capillary length d_0 and a kinetic coefficient

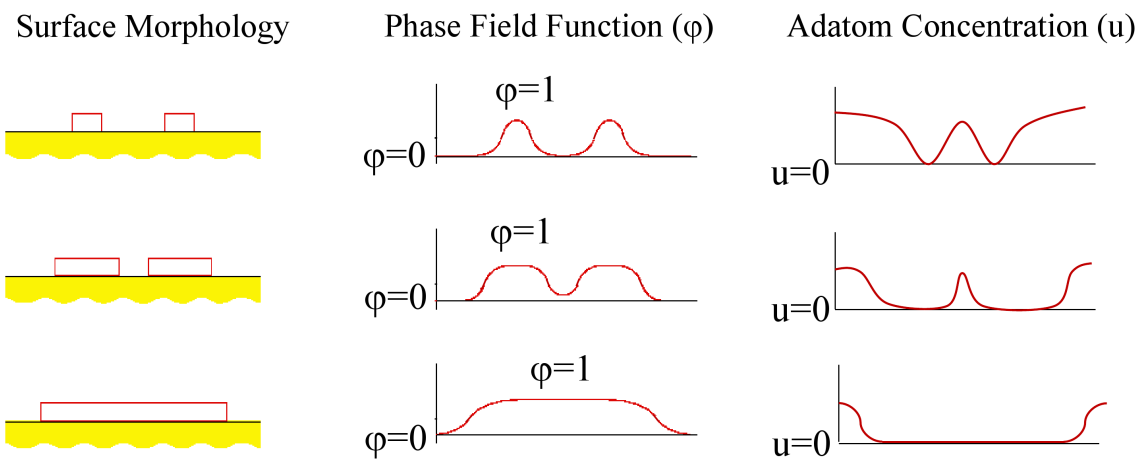

Figure 35: Schematic representation of the surface morphology using the order parameter ϕ and the adatom concentration u.

β from

$$d_0 = a_1 \frac{W}{\lambda}, \tag{11}$$

and

$$\beta = \frac{a_1 \tau}{\lambda W}\left[1 - a_2 \lambda \frac{W^2}{D\tau}\right], \tag{12}$$

where $a_1 = 0.36$ and $a_2 = 0.51$. More importantly, d_0 and β are related to each other in exactly the same way as they are related in the Burton, et al. model of step flow growth [114]. Namely,

$$v = D[\hat{\mathbf{n}} \cdot \nabla u]_{step} = \beta^{-1}[u - u_{eq} - d_0 \kappa]_{step} \tag{13}$$

where v is the velocity of a step, $\hat{\mathbf{n}}$ is a unit vector normal to the step, u_{eq} is the equilibrium concentration of adatoms at a straight step, and κ is the step curvature. The subscript "step" in Equation (13) means that the quantities in brackets are evaluated at the step edge. We consider the limit $\beta = 0$ only, which corresponds to fast attachment of adatoms to step edges (surface-diffusion-limited growth). In that case, we get the Gibbs-Thomson equation [11]

$$[u]_{step} = u_{eq} + d_0[\kappa]_{step}. \tag{14}$$

In the same $\beta = 0$ limit,

$$\lambda = \frac{a_1 W}{d_0} \qquad \text{and} \qquad \tau = \frac{a_1 a_2 W^3}{d_0 D}. \tag{15}$$

In practice, we let $a = 1$, $W = a$, and $u_{\text{eq}} = 0$. [1] The free parameters of the model are D (units of a^2/s), F (units of ML/sec), d_0 (units of a), and λ_n.

We discretized the coupled Eqs. (9) and (10) on a $L \times L$ square lattice with $L = 960$ grid points and solved them using no-flux boundary condition at the lattice edges and a two-dimensional forward time, central space (finite difference) algorithm. We found good convergence using a spatial grid size $\Delta x = 0.4a$. The time step Δt is chosen so that $\Delta t \ll (\Delta x)^2/D$. Maintenance of the last-stated condition requires that the time-step vary inversely with changes in D. Using that information, it is straightforward to show that the discretized equations depend only the ratio D/F. Accordingly, we set $D = 10^4 a^2/\text{sec}$ and varied F.

The deposition noise variable η in Eq. (9) is Gaussian distributed with zero mean and no correlations in space or time. However, rather than solve Eq. (9) as a stochastic differential equation, we followed Ref. [110] and used a KMC type algorithm to model depositions. Thus, we choose a grid site at random and set $u = a^2/(\Delta x)^2$ at that site. We then repeat this step every $1/F(L\Delta x)^2$ seconds. The surface coverage is defined as $\theta = Ft$.

7.3 Results and Discussion

7.3.1 Nucleation and Aggregation

Figure 36 illustrates the nucleation and aggregation behavior produced by the phase field equations (9) and (10). The left column shows the adatom density u at three successive times. The right column shows the order parameter ϕ (surface morphology) at the same three times. Panel (a) shows the rapid, isotropic diffusion of the adatom

[1] In principle, the value of u_{eq} affects both the nucleation rate and the growth rate of nucleated islands. However, for our choices of the other parameters, we find that the simulation results are very insensitive to the exact value of u_{eq}. For that reason, we have set $u_{eq} = 0$ in the simulations.

concentration away from a deposition event which occurred at the point labeled (4). Through the nucleation term in Eq. (10), this distribution of u triggers the growth of a small spike in ϕ at exactly the point (4). This spike, which we call a proto-island, is not yet visible in panel (b), which instead shows three proto-islands [labeled (1)–(3)] which were triggered by three earlier deposition events. The adatom density associated with these earlier events has completely diffused away by the time of deposition event (4).

Understanding the fate of proto-islands is the key to understanding the behavior of the model overall. Some proto-islands grow into true islands by the capture of adatom density from other deposition events. Other proto-islands disappear because not enough adatom density is captured before ϕ itself "diffuses" away due to the interface width term W in Eq. (10). Our choice of W produces well-defined islands with sharp edges. The surface free-energy minimization that leads to Eq. (10) implies that the islands are circular in shape (as if the simulation included fast edge diffusion). In detail, we label as a proto-island every set of one or more nearest-neighbor connected grid sites where $\phi > 0.05$. If the value of ϕ at each connected site is called ϕ_k, we form the quantity $s = (\Delta x/a)^2 \sum_k \phi_k$ for each proto-island and monitor its value as time goes on. If $s \to 0$, we say that this proto-island has disappeared; if $s > 1$ we say this proto-island has become a true island composed of s atoms.

Panel (c) in Fig. 36 shows the expected adatom concentration very soon after a deposition event at the point labeled (8). More interesting is panel (d), which shows seven true islands. Islands (1)–(3) evolved from the proto-islands (1)–(3) in panel (b). Islands (4)–(7) were produced by deposition events that occurred in the time between panels (a) and (c). A short time later, panel (e) shows that the adatom density associated with deposition event (8) has diffused entirely away. However, no island (8) has been created in panel (f) because proto-island (8) disappeared. It did not grow to a true island because the existing islands captured all the available adatom density. In other words, the island density in this neighborhood of the surface

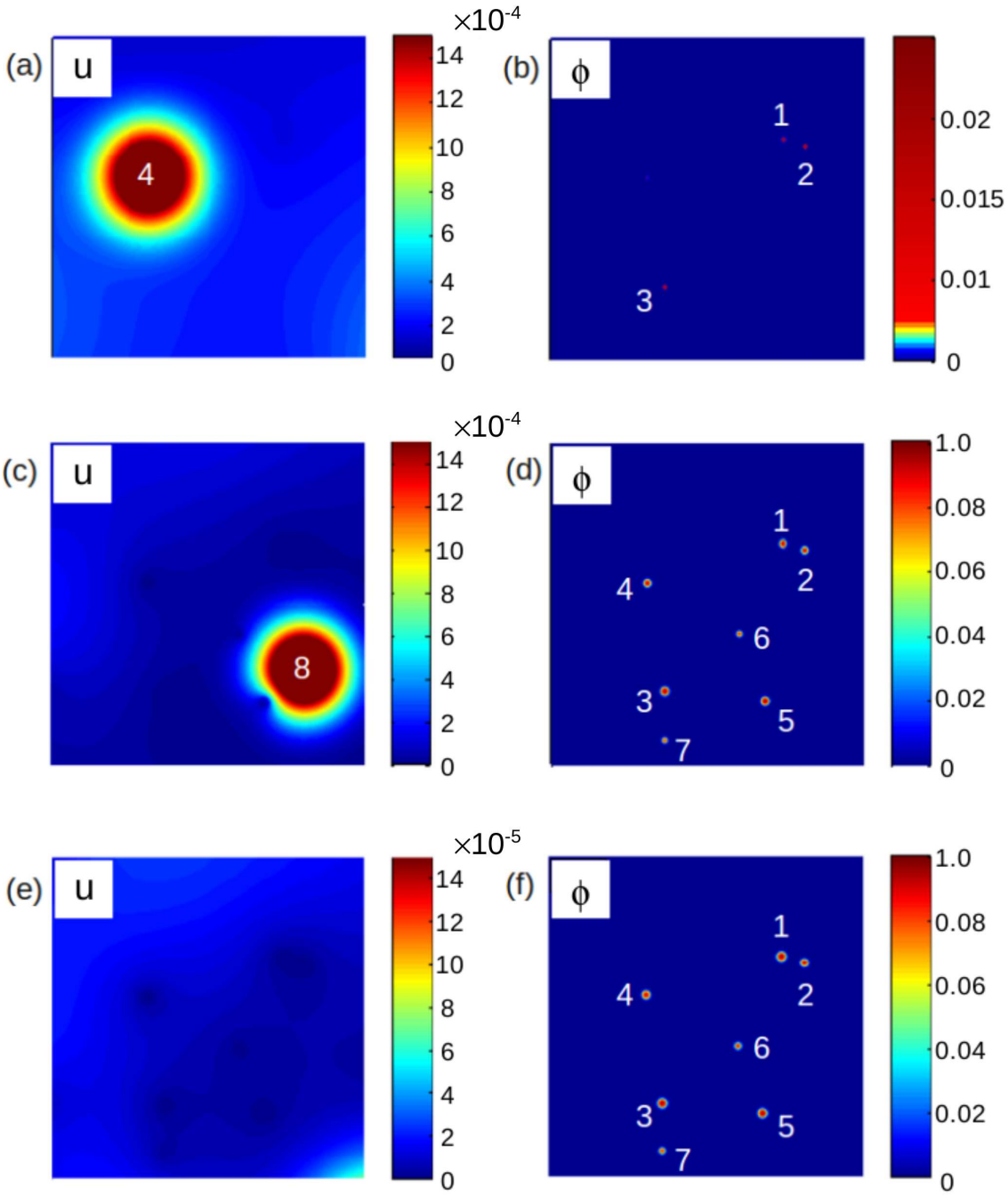

Figure 36: Time evolution of the order parameter and the corresponding adatom concentration. θ is the surface coverage. Note that the color bar is varied to optimize the contrast. For all panels, $D/F = 10^7$, $d_0 = 1.44 \times 10^{-6}$, $\lambda_n = 8.4 \times 10^{-3}$, and $L = 80a$. The surface coverage: panels (a) and (b) $\theta = 2.7{\times}10^{-4}$, panels (c) and (d) $\theta = 2.2{\times}10^{-2}$, and panels (e) and (f) $\theta = 2.8 \times 10^{-2}$

.

has saturated and further deposition only causes the existing islands to grow. Indeed, the very dark regions of panel (e) can be regarded as "denuded" zones around each island.

The foregoing shows that the *nucleation* of an island in the phase field model occurs quite differently than it does in, say, an atomistic KMC simulation. There, deposited atoms diffuse on the surface until they collide to form a stable island somewhere away from the deposition point of either atom. We have said that the phrase "irreversible growth" is used if this collision produces a stable island. We speak of "reversible growth" if a just-nucleated island can dissociate back into adatoms. That being said, the *aggregation* behavior of the phase field model seems quite similar to that seen in KMC and LSM simulations. We will see in a moment that this similarity (dissimilarity) of the nucleation (aggregation) process to other simulation results has consequences for the behavior of the distribution of island sizes and for the total island density.

For later use, we draw particular attention to the level set method to simulate submonolayer epitaxial growth. In LSM simulations, islands are nucleated at random positions on the surface using a rate-equation like weighting factor proportional to the square of the adatom density [108]. The adatom density itself evolves as dictated by a uniform deposition flux at every point and a diffusion equation with specified boundary conditions at the moving edges of existing islands. The method is very computer-time intensive but as mentioned earlier, the total island density and the distribution of island sizes agree very well with KMC simulations and with experiment.

7.3.2 Island Size Distribution

The island size distribution n_s is the number of islands composed of s atoms. If s_{av} is the average island size, it is well-known that a plot of the scaled quantity $n_s s_{av}^2/\theta$

versus s/s_{av} will collapse onto a single curve data collected for different values of D/F [101, 99]. One particular curve is characteristic of irreversible aggregation and the shape of this curve varies smoothly as the degree of reversibility is increased by changing, say, the pair-bond energy in a KMC simulation [115].

Figure 37(a) shows island size distributions obtained from our phase field simulations model at very low coverage for $D/F = 10^5 - 10^7$ and various choices of the model parameters d_0 and λ_n. Each data point of the same symbol represents the average of at least 20 simulations. The scaling curve we find agrees very well with *irreversible* KMC and LSM simulations and with low-temperature experimental data collected for Fe/Fe(001) [115, 116]. Data collapse onto a single curve generally required us to reduce the value of d_0 as we increased the value of D/F. Doing this (or changing λ_n) produced very different total island densities, even though the scaled island size distributions were the same. For example, the data associated with the symbols ▲ and ● in Fig. 37(a) have island densities that differ by 25%. Similar behavior occurs in LSM simulations when the boundary conditions at the island edges are changed slightly. [109] Based on Fig. 37(a), we conclude that the details of the island nucleation process are not critical to the shape of the island distribution when irreversible growth occurs. What matters is the subsequent process of monolayer capture by existing islands.

Figs. 37(b) and 37(c) show the effect on the island size distribution of progressively increasing the capillary constant d_0. The ▲ data in these two figures correspond to the same choices of D/F, λ_n, and θ used in Fig. 37(a). The change in shape we find for the scaled island size distribution as d_0 increases agrees quantitatively with the change in shape seen in *reversible* KMC simulations when the pair-bond energy is decreased or (equivalently) when the critical island size is increased [117]. Our results also agree with *reversible* LSM simulations [118].

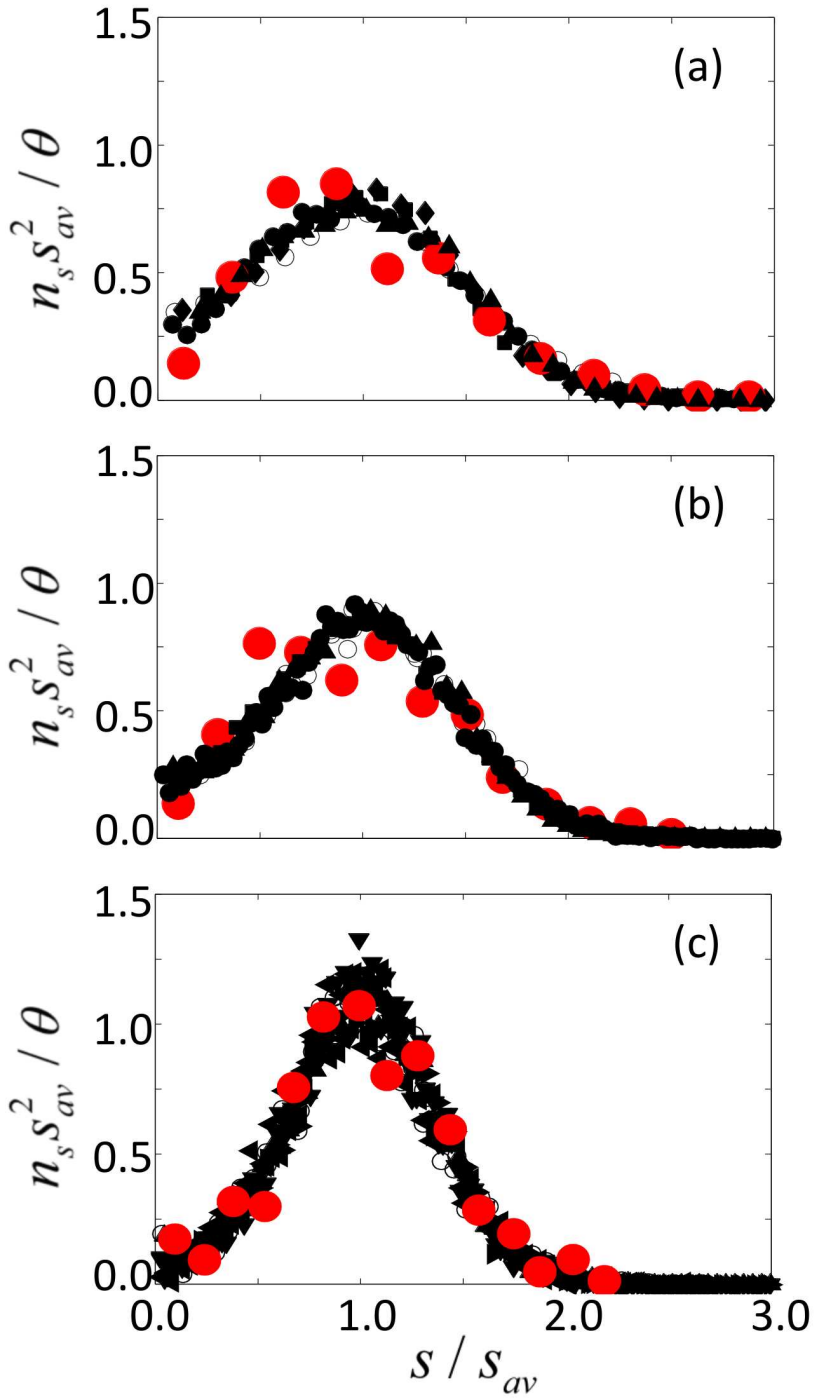

Figure 37: Crossover scaling of island size distributions. Experimental data (large red circles) replotted from Ref. [116] for different temperatures, and KMC data (open symbols) from Ref. [115]. The phase field parameters are as follows. (a) ■: $D/F = 10^5, d_0 = 1.44 \times 10^{-4}, \theta = 0.06, \lambda_n = 0.03$; ● and ▲: $D/F = 10^6, d_0 = 1.44 \times 10^{-5}$ and $2.43 \times 10^{-5}, \lambda_n = 0.06$ and $0.1, \theta = 0.05 - 0.1$. ♦: $D/F = 10^7, d_0 = 1.44 \times 10^{-6}, \lambda_n = 8.4 \times 10^{-3}, \theta = 0.01$. (b) ■: $D/F = 10^5, d_0 = 1.44 \times 10^{-4}, \theta = 0.1, \lambda_n = 0.03$; ● and ▲: $D/F = 10^6, d_0 = 1.44 \times 10^{-5}$ and $4.0 \times 10^{-5}, \lambda_n = 0.012$ and $0.1, \theta = 0.05 - 0.1$. (c) $D/F = 10^6$. ▲ and ▼: $d_0 = 1.0 \times 10^{-4}, \lambda_n = 0.1$, $\theta = 0.05$ and 0.1; ▶ and ◀: $d_0 = 3.2 \times 10^{-4}$, $\lambda_n = 1$, $\theta = 0.05$ and 0.1.

The step velocity in reversible LSM simulations is calculated from

$$v = D[\mathbf{n} \cdot \nabla u]_{step} - v_{det}, \tag{16}$$

where the second term takes account of the detachment of atoms from island boundaries. Typically, v_{det} is taken to be proportional to the density of island edge atoms. This may be contrasted with our Eq. (14), which shows that increasing d_0 has the effect of raising the adatom density at islands edges (which is zero in LSM simulations). For the BCF problem of adatom diffusion on terraces, this simultaneously reduces the gradient of the adatom density at the step edge in the leftmost in Eq. (13) and thus retards the growth speed of an island. The capillary constant d_0 measures the strength of the Gibbs-Thomson effect [11], which is the driving force for adatom detachment from step edges in phase field modeling.

7.3.3 Total Island Density

We have pointed out (in connection with Fig. 36) that nucleation is treated rather differently in the phase field model than in KMC or LSM simulations. To emphasize this point, Figure 38 shows the total island density as a function of d_0 and λ_n for $D/F = 10^6$. The decrease in island density with increasing d_0 is striking but not hard to understand. Larger d_0 increases the relative magnitude of the first two terms on the right-hand side of Eq. (10), which preserves the equilibrium state (i.e., $\phi = 0$ or $\phi = 1$). Consequently, proto-islands hardly grow in the beginning (when ϕ is close to zero) and many of them diffuse away. The island density increases as λ_n increases also. This parameter is the coefficient of the nucleation term in Eq. (10). Given the same surrounding adatom concentration, as one adatom is deposited, a larger λ_n triggers a larger change in the order parameter, which is more likely to survive and become an island.

The foregoing may be compared with a rate-equation analysis or an LSM simulation, where the nucleation rate is determined by a *global* average of the adatom

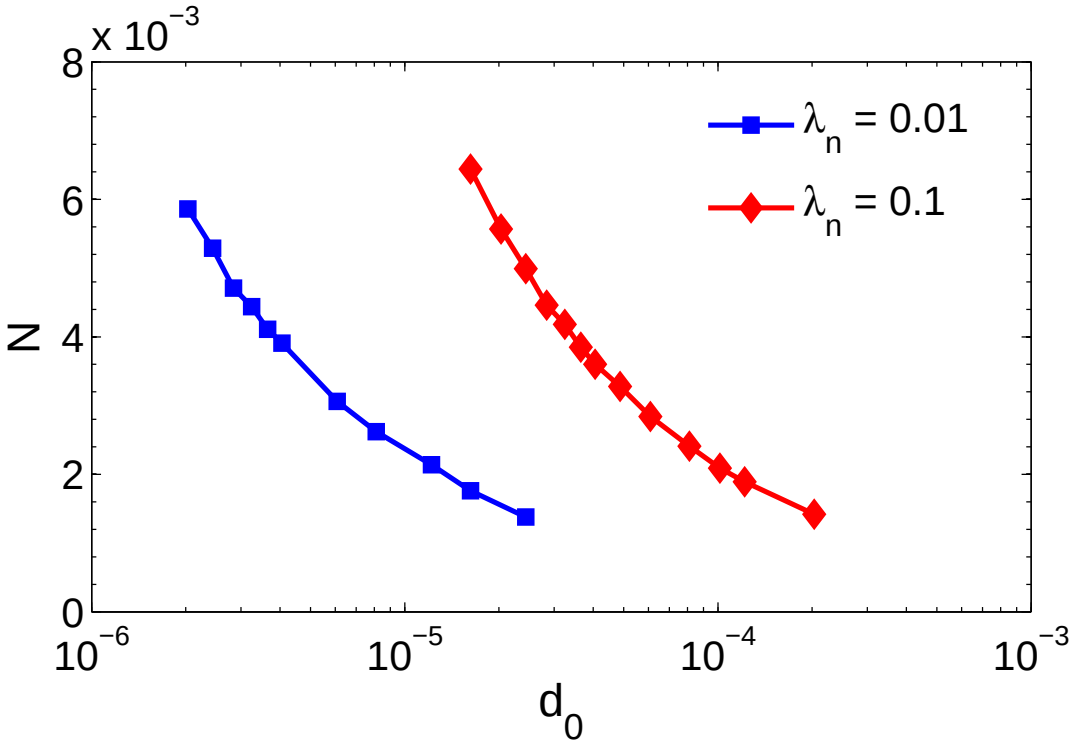

Figure 38: The island density at a coverage of $\theta = 0.1$ depends on both d_0 and λ_n. Simulations were done on a lattice with 1920×1920 grid points. $D/F = 10^6$.

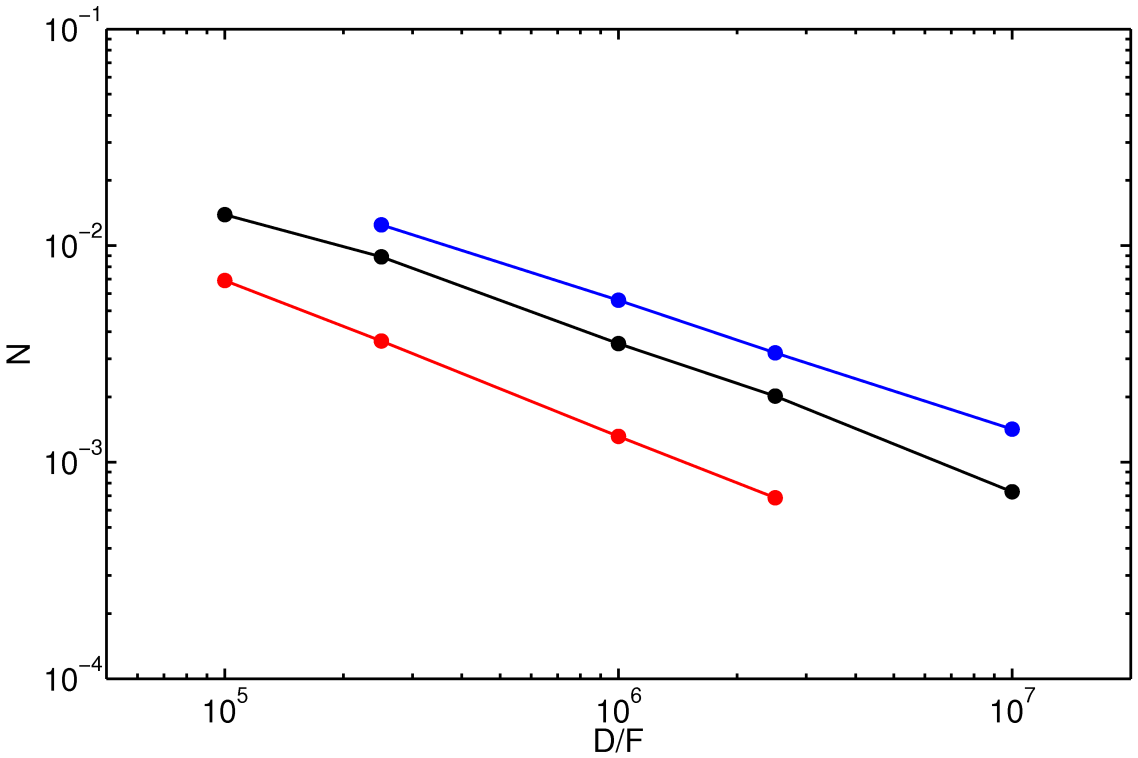

Figure 39: The island density scaling vs D/F with different choices of d_0 and λ_n. $\theta = 0.1$. Blue: $d_0 = 1.4 \times 10^{-6}$, $\lambda_n = 0.01$; Black: $d_0 = 4.0 \times 10^{-5}$, $\lambda_n = 0.1$; Red: $d_0 = 3.3 \times 10^{-4}$, $\lambda_n = 1$.

concentration over the whole domain. Specifically,

$$dN/dt = D\sigma_1\langle u^2\rangle, \tag{17}$$

where σ_1 is the (constant) capture number. In the standard rate theory of irreversible aggregations, Equation (17) leads to a well-known scaling law for the total island density: $N \sim (D/F)^{-\chi}$ with $\chi = 1/3$. This is also seen in irreversible LSM and KMC simulations. However, the mechanism implied by Eq. (17) is not truly captured by Eqs. (9) and (10). Instead, our phase field model uses $\lambda_n D u^2$ as a *local* estimate of the nucleation rate. We remind the reader that, unlike other simulation methods, most islands grow out of the initial adatom depositions in the phase field method. Be that as it may, upon fixing d_0 and λ_n and changing only D/F, we found that the total island density shows distinct scaling behavior. This is shown in Fig. 39. The curves of different color correspond to different values of d_0 and λ_n over a wide range. The average value for the scaling exponent is $\chi \approx 0.65$. It is worth remarking that the island size distributions from different data points on the same curve in Fig. 39 usually do not collapse very well. This suggests that the degree of reversibility is not the same.

We do not fully understand the scaling seen in Fig 39, although we presume a simple analytic theory exists which can reproduce the observed exponent. On the other hand, we can gain some insight by looking into the time evolution of the island density in more detail. Figure 40 is a typical curve of $N(t)$ obtained from a phase field simulation with $D/F = 10^7$. By changing the model parameters as described in Fig. 38, we can match the island density produced by a KMC simulation with the same value of D/F. However, there is a clear discrepancy in the nucleation rate: the island density approaches the steady state much faster in our simulations than in the KMC simulations.

In fact, all of our phase field simulations show similar behavior. Since the island size distribution is a characteristic of the aggregation regime, this could explain why

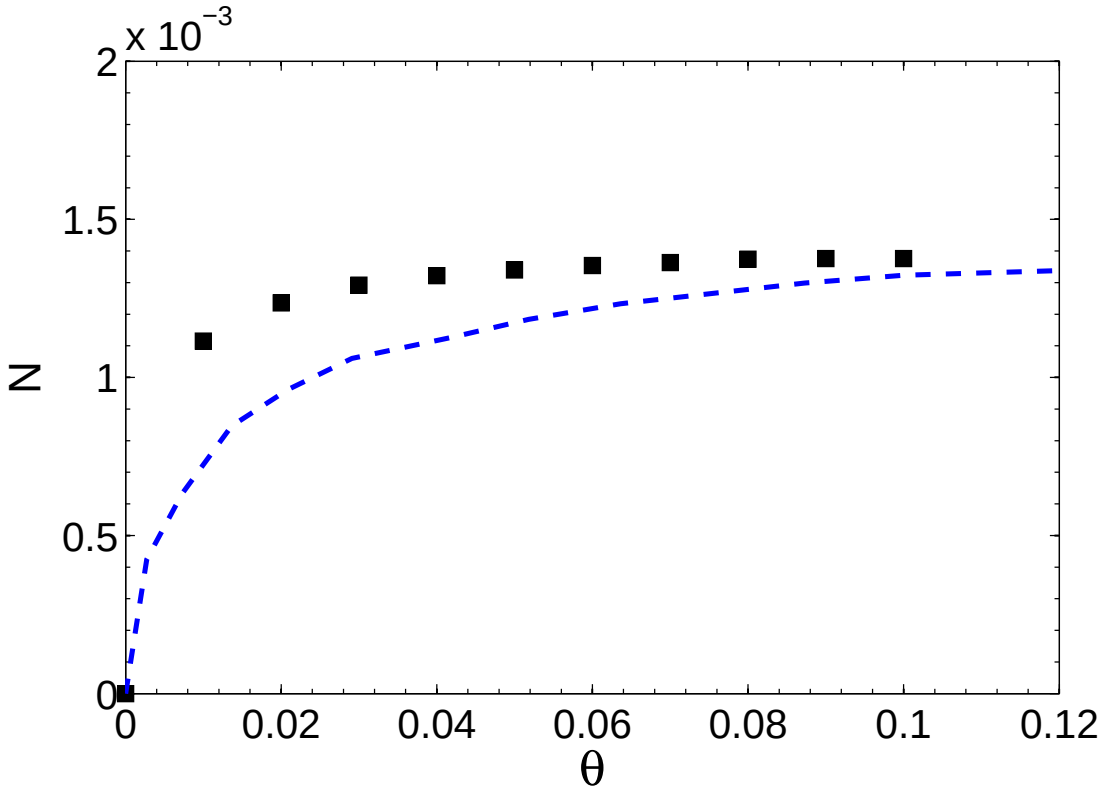

Figure 40: Nucleation shuts off faster in phase field simulations. For $D/F = 10^7$ and the same island density in the steady state, the time evolution of island density in phase field simulations (black squares) reaches the steady state much faster than in KMC simulations (dashed line, replotted from Ref. [109]). $d_0 = 1.44 \times 10^{-6}$ and $\lambda_n = 8.4 \times 10^{-3}$.

we can obtain the scaling of island size distribution at a much lower coverage than expected from KMC simulations (see Fig. 37). The fact that most islands tend to form at an earlier time is undoubtedly caused by the initial adatom depositions (see Fig. 36). It follows that the nucleation rate in this phase field model decreases faster than what we expect from Eq. (17), which results in a stronger dependence on u and thus changes the scaling of the island density.

7.4 Conclusion

In summary, we have shown that phase field modeling of sub-monolayer epitaxial growth reproduces the scaled island size distributions seen in experiment and obtained from other high-quality simulation methods. The crossover from irreversible aggregation to reversible aggregation is driven by the magnitude of a capillary constant which enters the Gibbs-Thomson equation. This shows that diffusion-limited aggregation phenomena are well captured by the model [119].

On the other hand, the scaling of the island density itself disagrees with experiment and with other simulation methods. This implies that our model does not treat nucleation as accurately as one would like. One simple solution is to replace the local nucleation rate $\lambda_n D u^2$ in Eq. (10) with the global average nucleation rate in Eq. (17). This is the scheme used in the level set simulations and we suspect this will produce the correct total island density without changing the high quality already obtained for the island size distributions. This might be important, moving forward, because the phase field method is less computationally intensive than the LSM and is much easier to implement at larger spatial scales and for more complicated epitaxial growth situations.

CHAPTER VIII

FINAL REMARKS

8.1 Summary of Results

In this thesis, results were reported for two related KMC models designed to specifically understand the growth kinetics of graphene on vicinal and nano-faceted surfaces of SiC, respectively. For vicinal surfaces, our model shows that there are two outcomes for each growing graphene strip: coalescence or climbover. It is interesting to compare them with two other similar kinetic processes previously identified for graphene deposition growth on Ru surfaces (see Fig. 9). In particular, the climbover process for growth on SiC corresponds to the graphene growth on Ru in the downhill direction.

The competition between coalescence and climbover results in a crossover of the graphene strip width distribution, and two growth regimes are identified. From our KMC simulations, a strategy for extracting effective energy barriers is proposed by using the experimental graphene layer coverages and the growth time. To further understand our graphene growth model, a rate-equation analysis is also developed. The numerical results are found to agree well with the KMC simulations.

Our KMC model for SiC nano-faceted surfaces generalizes the vicinal surface model by the addition of several kinetic processes. This new model can be used to interpret the nonuniform graphene layer thickness observed for graphene growth on nano-faceted surfaces. When the fracture angle is used to characterize the growth-induced fracture of a nano-facet, the distribution of fracture angles is related to the graphene strip width distribution. Similar to the strip width distribution, as the terrace propagation barrier decreases, the fracture angle distribution changes from

a Gaussian to a power-law. Our analytic treatment for the most probable fracture angle agrees well with the KMC simulations. Using the fracture angle distribution, the energy barriers of our KMC model can be extracted from experiments.

As a step toward studying the deposition epitaxial growth which has been used to grow graphene on metal surfaces, a phase field method has been introduced and examined in the submonolayer regime. It is found that this method reproduces the scaled island size distribution seen in experiments and obtained from other simulation methods. The crossover of the island size distribution from irreversible aggregation to reversible aggregation is driven by the magnitude of a capillary constant. This indicates that the phase field method can well describe diffusion-limited aggregation phenomena. However, our method to treat island nucleation results in a scaling of island density that does not agree with experiments and other simulation methods.

8.2 Future Considerations

Our KMC models predict that the morphology of graphene grown from SiC is strongly dependent on the effective energy barriers to the kinetic process assumed. It is important to realize that these growth parameters can be correlated to the experimental growth conditions such as the partial pressure of silicon in the growth chamber. Our model results thus can be used by experimenters to explore the exact relations. We have shown that as a function of our model parameters, there is a crossover in the graphene strip width distribution and the fracture angle distribution for SiC vicinal surfaces and nano-faceted surfaces, respectively. Scanning microscopy techniques can be exploited to identify these transitions.

Recent experiments show that the growth rate decreases with increasing graphene thickness [15]. It will be interesting for our model to include different nucleation and propagation barriers for different graphene layers so that the model can be more

realistic. One may also use our approach to study graphene growth on 4H-SiC surfaces, in which case the SiC steps are double and quadruple bilayers. As mentioned previously, graphene growth from SiC double bilayers has an instability, which leads to more complicated surface morphology and requires a two dimensional model.

Our phase field model does not treat nucleation accurately. To address that, we propose to replace the local nucleation rate $\lambda D u^2$ in Eq. (10) with the global average nucleation rate in Eq. (17). We suspect that this will produce the correct total island density. However, a strategy has to be formed to decide where to seed the proto-islands.

APPENDIX A

KMC ALGORITHMS

Our KMC simulations use the algorithms from Ref. [100, 120], which are summarized as follows.

1. A KMC event is defined by its move and rate r_i. The move is specified by the change of data structures used to describe the surface morphology. The data structures for the list of events and the surface morphology are all maintained. The events can be classified into several categories based on their rates. Let M be the number of possible KMC events, then the total rate is $R = \sum_{i=1}^{M} r_i$.

2. Choose a random number ρ in the range [0,1).

3. Update the time $\Delta t = -(1/R)\log(\rho)$.

4. Find the corresponding integer ν such that

$$\sum_{i=1}^{\nu-1} r_i \leq \rho R < \sum_{i=1}^{\nu} r_i. \tag{18}$$

   To speedup the search, a data structure of partial sums of the rates rp_i is maintained to use the binary search algorithm. The binary search algorithm is described as follows.

   a Define $low = 1$, $up = M$.

   b Define $pivot = (low + up)/2$.

   c If $rp_{pivot-1} \leq \rho R < rp_{pivot}$, then the event is found. $\nu = pivot$, exit the binary search. Otherwise, if $\rho R < rp_{pivot-1}$, then $up = pivot$; if $\rho R > rp_{pivot}$, then $low = pivot$.

d Go back to Step (b).

5. Execute the event ν by updating the data structures of the surface morphology.

6. Update the rate list r_i, partial sum list rp_i and R as a result of event ν.

7. Go back to Step (2) for the next event.

APPENDIX B

COMPUTATIONAL RESOURCES AND CONVERGENCE

To obtain statistically meaningful results from our KMC model, a large number of simulation runs are required. Intensive computations were performed on two supercomputers, Lonestar and Ranger, located at the Texas Advanced Computing Center (TACC). Time allocations were requested through a National Science Foundation program Teragrid, which is an open scientific infrastructure working in partnership with a dozen high-performance computational resource providers across the United States.

Some comment is needed on the convergence of our KMC simulations. When $\Delta E/kT$ is small, we typically obtain statistically significant results for layer 1 and layer 2 coverages by averaging over about 10^2 simulation runs. This type of computation can be done on a standard workstation within 12 hours, using an iterative algorithm. During each simulation iteration, a different random number seed is used.

When $\Delta E/kT$ is large, the kinetic processes in our model have very different rates, and much more variation in growth morphology occurs. To obtain statistically meaningful results in this regime, we typically had to average over $10^5 - 10^6$ runs. In this case, we performed the computation in parallel over a few tens to hundreds of cores of the two supercomputers. Each core is responsible for about 10^3 simulation runs. The parallel computation is managed through a Message-Passing-Interface (MPI), which is a standard message-passing application for C or similar languages to function on multiple-core computation systems. The parallel computations usually can be performed within 24 hours.

By contrast, to study the fracture angle in our KMC simulations for graphene

growth on SiC nano-faceted surfaces, much less intensive computation was needed. The computations were typically executed on a standard workstation with Intel i7 quad-core processors. A typical simulation takes less than 24 hours.

In our study of phase field method, we used a two-dimensional square lattice. The computation was done on the two supercomputers mentioned earlier. A parallel domain-decomposition algorithm was also used to speed up the computation. For each time iteration, this algorithm uses MPI to deliver the variable information stored on the boundary points of each core. In addition, we also used MPI to obtain statistical results of island size distributions. The most intensive computation requires about 100 cores and a wall time of 24 hours.

REFERENCES

[1] P. Avouris. Carbon nanotube electronics and photonics. *Phys. Today*, 62(1): 34–40, January 2009.

[2] K. Nakada, M. Fujita, G. Dresselhaus, and M. S. Dresselhaus. Edge state in graphene ribbons: Nanometer size effect and edge shape dependence. *Phys. Rev. B*, 54(24):17954–17961, December 1996.

[3] C. Berger, Z. M. Song, T. B. Li, X. B. Li, A. Y. Ogbazghi, R. Feng, Z. T. Dai, A. N. Marchenkov, E. H. Conrad, P. N. First, and W. A. de Heer. Ultrathin epitaxial graphite: 2D electron gas properties and a route toward graphene-based nanoelectronics. *J. Phys. Chem. B*, 108(52):19912–19916, December 2004.

[4] H. P. Boehm, A. Clauss, G. O. Fischer, and U. Hofmann. Dnnste kohlenstoff-folien. *Z. Naturforschung.*, 17 b:150–153, 1962.

[5] H. P. Boehm, R. Setton, and E. Stumpp. Nomenclature and terminology of graphite-intercalation compounds. *Pure Appl. Chem.*, 66(9):1893–1901, September 1994.

[6] A.J. Van Bommel, J.E. Crombeen, and A. Van Tooren. Leed and auger electron observations of the SiC(0001) surface. *Surf. Sci.*, 48(2):463–72, 1975.

[7] I. Forbeaux, J. M. Themlin, and J. M. Debever. Heteroepitaxial graphite on 6H-SiC(0001): Interface formation through conduction-band electronic structure. *Phys. Rev. B*, 58(24):16396–16406, December 1998.

[8] R. M. Tromp and J. B. Hannon. Thermodynamics and kinetics of graphene growth on SiC(0001). *Phys. Rev. Lett.*, 102(10):106104, March 2009.

[9] C. Virojanadara, M. Syvajarvi, R. Yakimova, L. I. Johansson, A. A. Zakharov, and T. Balasubramanian. Homogeneous large-area graphene layer growth on 6H-SiC(0001). *Phys. Rev. B*, 78(24):245403, December 2008.

[10] K. V. Emtsev, A. Bostwick, K. Horn, J. Jobst, G. L. Kellogg, L. Ley, J. L. McChesney, T. Ohta, S. A. Reshanov, J. Rohrl, E. Rotenberg, A. K. Schmid, D. Waldmann, H. B. Weber, and T. Seyller. Towards wafer-size graphene layers by atmospheric pressure graphitization of silicon carbide. *Nat. Mater.*, 8(3): 203–207, March 2009.

[11] A. Pimpinelli and J. Villain. *Physics of Crystal Growth*. Cambridge UP, Cambridge, 1998.

[12] T. Ogino, H. Hibino, and Y. Homma. Kinetics and thermodynamics of surface steps on semiconductors. *Crit. Rev. Solid State*, 24(3):227–263, 1999.

[13] B.A. Joyce, D.D. Vvedensky, and Foxon C.T. *Handbook on Semiconductors: Materials, Properties, and Preparation*, volume 3A. Elsevier, Amsterdam, 1994. 275-368 pp.

[14] P. Kratzer, E. Penev, and M. Scheffler. First-principles studies of kinetics in epitaxial growth of III-V semiconductors. *Appl. Phys. A*, 75(1):79–88, July 2002.

[15] S. Tanaka, K. Morita, and H. Hibino. Anisotropic layer-by-layer growth of graphene on vicinal SiC(0001) surfaces. *Phys. Rev. B*, 81(4):041406, January 2010.

[16] L. S. Ramsdell. Studies on silicon carbide. *Am. Minera.*, 32(1-2):64–82, 1947.

[17] J. Kato, S. Tanaka, S. Yamada, and I. Suemune. Structural anisotropy in GaN films grown on vicinal 4H-SiC surfaces by metallorganic molecular-beam epitaxy. *Appl. Phys. Lett.*, 83(8):1569–1571, August 2003.

[18] A. Nakajima, Y. Furukawa, S. Koga, and H. Yonezu. Growth of high-quality AlN with low pit density on SiC substrates. *J. Cryst. Growth*, 265(3-4):351–356, May 2004.

[19] Y. M. Tairov and V. F. Tsvetkov. Investigation of growth processes of ingots of silicon-carbide single-crystals. *J. Cryst. Growth*, 43(2):209–212, 1978.

[20] J. Drowart, G. De Maria, and M. G. Inghram. Thermodynamic study of SiC utilizing a mass spectrometer. *J. Chem. Phys.*, 29(5):1015–1021, 1958.

[21] W. A. de Heer, C. Berger, M. Ruan, M. Sprinkle, X. B. Li, Y. Hu, B. Zhang, J. Hankinson, and E. H. Conrad. Large area and structured epitaxial graphene produced by confinement controlled sublimation of silicon carbide. *arXiv:1103.3552v1 [cond-mat.mtrl-sci]*, 2011.

[22] T. Sugii, T. Aoyama, and T. Ito. Low-temperature growth of beta-SiC on Si by gas-source MBE. *J. Electrochem. Soc.*, 137(3):989–992, March 1990.

[23] T. Kimoto, A. Itoh, and H. Matsunami. Step-controlled epitaxial growth of high-quality SiC layers. *Phys. Status Solidi.*, 202(1):247–262, July 1997.

[24] T. Ueda, H. Nishino, and H. Matsunami. Crystal-growth of SiC by step-controlled epitaxy. *J. Cryst. Growth*, 104(3):695–700, August 1990.

[25] T. Kimoto, A. Itoh, and H. Matsunami. Step bunching in chemical-vapor-deposition of 6H-SiC and 4H-SiC on vicinal SiC(0001) faces. *Appl. Phys. Lett.*, 66(26):3645–3647, June 1995.

[26] T. Kimoto, A. Itoh, H. Matsunami, and T. Okano. Step bunching mechanism in chemical vapor deposition of 6H- and 4H-SiC0001. *J. Appl. Phys.*, 81(8): 3494–3500, April 1997.

[27] V. Borovikov and A. Zangwill. Step bunching of vicinal 6H-SiC(0001) surfaces. *Phys. Rev. B*, 79(24):245413, June 2009.

[28] F. R. Chien, S. R. Nutt, W. S. Yoo, T. Kimoto, and H. Matsunami. Terrace growth and polytype development in epitaxial beta-SiC films on alpha-SiC (6H and 15R) substrates. *J. Mater. Res.*, 9(4):940–954, April 1994.

[29] M. Syvajarvi, R. Yakimova, and E. Janzen. Interfacial properties in liquid phase growth of SiC. *J. Electrochem. Soc.*, 146(4):1565–1569, April 1999.

[30] M. Syvajarvi, R. Yakimova, and E. Janzen. Step-bunching in sic epitaxy: anisotropy and influence of growth temperature. *J. Cryst. Growth*, 236(1-3): 297–304, March 2002.

[31] C. A. Zorman, A. J. Fleischman, A. S. Dewa, M. Mehregany, C. Jacob, S. Nishino, and P. Pirouz. Epitaxial-growth of 3C-SiC films on 4-inch diam (100) silicon-wafers by atmospheric-pressure chemical-vapor-deposition. *J. Appl. Phys.*, 78(8):5136–5138, October 1995.

[32] A. Severino, C. Bongiorno, N. Piluso, M. Italia, M. Camarda, M. Mauceri, G. Condorelli, M. A. Di Stefano, B. Cafra, A. La Magna, and F. La Via. High-quality 6 inch (111) 3C-SiC films grown on off-axis (111) Si substrates. *Thin Solid Films*, 518:S165–S169, January 2010.

[33] J. A. Powell, L. G. Matus, M. A. Kuczmarski, C. M. Chorey, T. T. Cheng, and P. Pirouz. Improved beta-sic heteroepitaxial films using off-axis si substrates. *Appl. Phys. Lett.*, 51(11):823–825, September 1987.

[34] S. Nishino, J. A. Powell, and H. A. Will. Production of large-area single-crystal wafers of cubic SiC for semiconductor-devices. *Appl. Phys. Lett.*, 42(5):460–462, 1983.

[35] A. Ouerghi, A. Kahouli, D. Lucot, M. Portail, L. Travers, J. Gierak, J. Penuelas, P. Jegou, A. Shukla, T. Chassagne, and M. Zielinski. Epitaxial graphene on cubic SiC(111)/Si(111) substrate. *Appl. Phys. Lett.*, 96(19):191910, May 2010.

[36] C. Coletti, K. V. Emtsev, A. A. Zakharov, T. Ouisse, D. Chaussende, and U. Starke. Large area quasi-free standing monolayer graphene on 3C-SiC(111). *arXiv:1109.6240v1 [cond-mat.mtrl-sci]*, 2011.

[37] F. Owman, C. Hallin, P. Martensson, and E. Janzen. Removal of polishing-induced damage from 6H-SiC(0001) substrates by hydrogen etching. *J. Cryst. Growth*, 167(1-2):391–395, September 1996.

[38] A. Kawasuso, K. Kojima, M. Yoshikawa, H. Itoh, and K. Narumi. Effect of hydrogen etching on 6H-SiC surface morphology studied by reflection high-energy positron diffraction and atomic force microscopy. *Appl. Phys. Lett.*, 76 (9):1119–1121, February 2000.

[39] A. Nakajima, H. Yokoya, Y. Furukawa, and H. Yonezu. Step control of vicinal 6H-SiC(0001) surface by H-2 etching. *J. Appl. Phys.*, 97(10):104919, May 2005.

[40] S. Nakamura, T. Kimoto, H. Matsunami, S. Tanaka, N. Teraguchi, and A. Suzuki. Formation of periodic steps with a unit-cell height on 6H-SiC(0001) surface by HCl etching. *Appl. Phys. Lett.*, 76(23):3412–3414, June 2000.

[41] Z. Y. Xie, C. H. Wei, L. Y. Li, Q. M. Yu, and J. H. Edgar. Gaseous etching of 6H-SiC at relatively low temperatures. *J. Cryst. Growth*, 217(1-2):115–124, July 2000.

[42] V. Ramachandran, M. F. Brady, A. R. Smith, R. M. Feenstra, and D. W. Greve. Preparation of atomically flat surfaces on silicon carbide using hydrogen etching. *J. Electron. Mater.*, 27(4):308–312, April 1998.

[43] A. A. Burk and L. B. Rowland. The role of excess silicon and in situ etching on 4H-SiC and 6H-SiC epitaxial layer morphology. *J. Cryst. Growth*, 167(3-4): 586–595, October 1996.

[44] M. Hupalo, E. H. Conrad, and M. C. Tringides. Growth mechanism for epitaxial graphene on vicinal 6H-SiC(0001) surfaces: A scanning tunneling microscopy study. *Phys. Rev. B*, 80(4):041401, July 2009.

[45] T. Ohta, N. C. Bartelt, S. Nie, K. Thurmer, and G. L. Kellogg. Role of carbon surface diffusion on the growth of epitaxial graphene on SiC. *Phys. Rev. B*, 81 (12):121411, March 2010.

[46] K. Hayashi, K. Morita, S. Mizuno, H. Tochihara, and S. Tanaka. Stable surface termination on vicinal 6H-SiC(0001) surfaces. *Surf. Sci.*, 603(3):566–570, February 2009.

[47] S. Nie, C. D. Lee, R. M. Feenstra, Y. Ke, R. P. Devaty, W. J. Choyke, C. K. Inoki, T. S. Kuan, and G. Gu. Step formation on hydrogen-etched 6H-SiC0001 surfaces. *Surf. Sci.*, 602(17):2936–2942, September 2008.

[48] H. Nakagawa, S. Tanaka, and I. Suemune. Self-ordering of nanofacets on vicinal SiC surfaces. *Phys. Rev. Lett.*, 91(22):226107, November 2003.

[49] K. S. Novoselov, A. K. Geim, S. V. Morozov, D. Jiang, Y. Zhang, S. V. Dubonos, I. V. Grigorieva, and A. A. Firsov. Electric field effect in atomically thin carbon films. *Science*, 306(5696):666–669, October 2004.

[50] P. R. Wallace. The band theory of graphite. *Phys. Rev.*, 71(9):622–634, 1947.

[51] X. Du, I. Skachko, A. Barker, and E. Y. Andrei. Approaching ballistic transport in suspended graphene. *Nat. Nanotech.*, 3(8):491–495, August 2008.

[52] X. Du, I. Skachko, F. Duerr, A. Luican, and E. Y. Andrei. Fractional quantum Hall effect and insulating phase of Dirac electrons in graphene. *Nature*, 462 (7270):192–195, November 2009.

[53] X. B. Li, X. S. Wu, M. Sprinkle, F. Ming, M. Ruan, Y. K. Hu, C. Berger, and W. A. de Heer. Top- and side-gated epitaxial graphene field effect transistors. *Physica Stat. Solidi A*, 207(2):286–290, February 2010.

[54] FN Xia, D. B. Farmer, Y. M. Lin, and P. Avouris. Graphene field-effect transistors with high on/off current ratio and large transport band gap at room temperature. *Nano Lett.*, 10(2):715–718, February 2010.

[55] Y. W. Son, M. L. Cohen, and S. G. Louie. Energy gaps in graphene nanoribbons. *Phys. Rev. Lett.*, 97(21):216803, November 2006.

[56] M. Y. Han, B. Ozyilmaz, Y. B. Zhang, and P. Kim. Energy band-gap engineering of graphene nanoribbons. *Phys. Rev. Lett.*, 98(20):206805, May 2007.

[57] X. L. Li, X. R. Wang, L. Zhang, S. W. Lee, and H. J. Dai. Chemically derived, ultrasmooth graphene nanoribbon semiconductors. *Science*, 319(5867):1229–1232, February 2008.

[58] Z. Q. Wei, D. B. Wang, S. Kim, S. Y. Kim, Y. K. Hu, M. K. Yakes, A. R. Laracuente, Z. T. Dai, S. R. Marder, C. Berger, W. P. King, W. A. de Heer, P. E. Sheehan, and E. Riedo. Nanoscale tunable reduction of graphene oxide for graphene electronics. *Science*, 328(5984):1373–1376, June 2010.

[59] R. Balog, B. Jorgensen, L. Nilsson, M. Andersen, E. Rienks, M. Bianchi, M. Fanetti, E. Laegsgaard, A. Baraldi, S. Lizzit, Z. Sljivancanin, F. Besenbacher, B. Hammer, T. G. Pedersen, P. Hofmann, and L. Hornekaer. Bandgap opening in graphene induced by patterned hydrogen adsorption. *Nat. Mater.*, 9(4):315–319, April 2010.

[60] J. T. Robinson, J. S. Burgess, C. E. Junkermeier, S. C. Badescu, T. L. Reinecke, F. K. Perkins, M. K. Zalalutdniov, J. W. Baldwin, J. C. Culbertson, P. E. Sheehan, and E. S. Snow. Properties of fluorinated graphene films. *Nano Lett.*, 10(8):3001–3005, August 2010.

[61] M. Sprinkle, M. Ruan, Y. Hu, J. Hankinson, M. Rubio-Roy, B. Zhang, X. Wu, C. Berger, and W. A. de Heer. Scalable templated growth of graphene nanoribbons on SiC. *Nat. Nanotech.*, 5(10):727–731, October 2010.

[62] Y. M. Lin, C. Dimitrakopoulos, K. A. Jenkins, D. B. Farmer, H. Y. Chiu, A. Grill, and P. Avouris. 100-GHz transistors from wafer-scale epitaxial graphene. *Science*, 327(5966):662–662, February 2010.

[63] K. S. Kim, Y. Zhao, H. Jang, S. Y. Lee, J. M. Kim, K. S. Kim, J. H. Ahn, P. Kim, J. Y. Choi, and B. H. Hong. Large-scale pattern growth of graphene films for stretchable transparent electrodes. *Nature*, 457(7230):706–710, February 2009.

[64] F. Schedin, A. K. Geim, S. V. Morozov, E. W. Hill, P. Blake, M. I. Katsnelson, and K. S. Novoselov. Detection of individual gas molecules adsorbed on graphene. *Nat. Mater.*, 6(9):652–655, September 2007.

[65] H. Hiura, T. W. Ebbesen, J. Fujita, K. Tanigaki, and T. Takada. Role of sp(3) defect structures in graphite and carbon nanotubes. *Nature*, 367(6459):148–151, January 1994.

[66] X. K. Lu, M. F. Yu, H. Huang, and R. S. Ruoff. Tailoring graphite with the goal of achieving single sheets. *Nanotechnology*, 10(3):269–272, September 1999.

[67] H. Shioyama. Cleavage of graphite to graphene. *J. Mater. Sci. Lett.*, 20(6): 499–500, March 2001.

[68] Y. B. Zhang, J. P. Small, W. V. Pontius, and P. Kim. Fabrication and electric-field-dependent transport measurements of mesoscopic graphite devices. *Appl. Phys. Lett.*, 86(7):073104, February 2005.

[69] Y. B. Zhang, Y. W. Tan, H. L. Stormer, and P. Kim. Experimental observation of the quantum Hall effect and berry's phase in graphene. *Nature*, 438(7065): 201–204, November 2005.

[70] R. Rosei, M. Decrescenzi, F. Sette, C. Quaresima, A. Savoia, and P. Perfetti. Structure of graphitic carbon on Ni(111) - a surface extended-energy-loss fine-structure study. *Phys. Rev. B*, 28(2):1161–1164, 1983.

[71] T. Aizawa, R. Souda, S. Otani, Y. Ishizawa, and C. Oshima. Anomalous bond of monolayer graphite on transition-metal carbide surfaces. *Phys. Rev. Lett.*, 64(7):768–771, February 1990.

[72] H. Itoh, T. Ichinose, C. Oshima, T. Ichinokawa, and T. Aizawa. Scanning tunneling microscopy of monolayer graphite epitaxially grown on a TiC(111) surface. *Surf. Sci.*, 254(1-3):L437–L442, August 1991.

[73] T. A. Land, T. Michely, R. J. Behm, J. C. Hemminger, and G. Comsa. STM investigation of single layer graphite structures produced on Pt(111) by hydrocarbon decomposition. *Surf. Sci.*, 264(3):261–270, March 1992.

[74] S. Marchini, S. Gunther, and J. Wintterlin. Scanning tunneling microscopy of graphene on Ru(0001). *Phys. Rev. B*, 76(7):075429, August 2007.

[75] P. W. Sutter, J. I. Flege, and E. A. Sutter. Epitaxial graphene on ruthenium. *Nat. Mater.*, 7(5):406–411, May 2008.

[76] S. Bae, H. Kim, Y. Lee, X. F. Xu, J. S. Park, Y. Zheng, J. Balakrishnan, T. Lei, H. R. Kim, Y. I. Song, Y. J. Kim, K. S. Kim, B. Ozyilmaz, J. H. Ahn, B. H. Hong, and S. Iijima. Roll-to-roll production of 30-inch graphene films for transparent electrodes. *Nat. Nanotech.*, 5(8):574–578, August 2010.

[77] M. Sprinkle, D. Siegel, Y. Hu, J. Hicks, A. Tejeda, A. Taleb-Ibrahimi, P. Le Fevre, F. Bertran, S. Vizzini, H. Enriquez, S. Chiang, P. Soukiassian, C. Berger, W. A. de Heer, A. Lanzara, and E. H. Conrad. First direct observation of a nearly ideal graphene band structure. *Phys. Rev. Lett.*, 103(22): 226803, November 2009.

[78] C. Berger, Z. M. Song, X. B. Li, X. S. Wu, N. Brown, C. Naud, D. Mayou, T. B. Li, J. Hass, A. N. Marchenkov, E. H. Conrad, P. N. First, and W. A. de Heer. Electronic confinement and coherence in patterned epitaxial graphene. *Science*, 312(5777):1191–1196, May 2006.

[79] X. S. Wu, Y. K. Hu, M. Ruan, N. K. Madiomanana, J. Hankinson, M. Sprinkle, C. Berger, and W. A. de Heer. Half integer quantum Hall effect in high mobility single layer epitaxial graphene. *Appl. Phys. Lett.*, 95(22):223108, November 2009.

[80] J. Hass, W. A. de Heer, and E. H. Conrad. The growth and morphology of epitaxial multilayer graphene. *J. Phys.: Cond. Matter*, 20(32):323202, August 2008.

[81] J. B. Hannon and R. M. Tromp. Pit formation during graphene synthesis on SiC(0001): In situ electron microscopy. *Phys. Rev. B*, 77(24):241404, June 2008.

[82] M. Sprinkle. *Epitaxial Graphene On Silicon Carbide: Low-Vacuum Growth, Characterization, and Device Fabricatiion.* PhD thesis, Georgia Institute of Technology, 2010.

[83] E. Rollings, G. H. Gweon, S. Y. Zhou, B. S. Mun, J. L. McChesney, B. S. Hussain, A. Fedorov, P. N. First, W. A. de Heer, and A. Lanzara. Synthesis and characterization of atomically thin graphite films on a silicon carbide substrate. *J. Phys. Chem. Solids*, 67(9-10):2172–2177, September 2006.

[84] L. Muehlhoff, W. J. Choyke, M. J. Bozack, and J. T. Yates. Comparative electron spectroscopic studies of surface segregation on SiC(0001) and SiC(000-1). *J. Appl. Phys.*, 60(8):2842–2853, October 1986.

[85] J. Bernhardt, M. Nerding, U. Starke, and K. Heinz. Stable surface reconstructions on 6H-SiC(0001). *Mater. Sci. Eng., B*, 61-2:207–211, July 1999.

[86] J. Hass, F. Varchon, J. E. Millan-Otoya, M. Sprinkle, N. Sharma, W. A. De Heer, C. Berger, P. N. First, L. Magaud, and E. H. Conrad. Why multilayer graphene on 4H-SiC(000(1)over-bar) behaves like a single sheet of graphene. *Phys. Rev. Lett.*, 100(12):125504, March 2008.

[87] C. Faugeras, A. Nerriere, M. Potemski, A. Mahmood, E. Dujardin, C. Berger, and W. A. de Heer. Few-layer graphene on SiC, pyrolitic graphite, and graphene: A raman scattering study. *Appl. Phys. Lett.*, 92(1):011914, January 2008.

[88] W. A. de Heer, C. Berger, X. S. Wu, P. N. First, E. H. Conrad, X. B. Li, T. B. Li, M. Sprinkle, J. Hass, M. L. Sadowski, M. Potemski, and G. Martinez. Epitaxial graphene. *Solid State Commun.*, 143(1-2):92–100, July 2007.

[89] P. Lauffer, K. V. Emtsev, R. Graupner, T. Seyller, L. Ley, S. A. Reshanov, and H. B. Weber. Atomic and electronic structure of few-layer graphene on SiC(0001) studied with scanning tunneling microscopy and spectroscopy. *Phys. Rev. B*, 77(15):155426, April 2008.

[90] J. Robinson, X. J. Weng, K. Trumbull, R. Cavalero, M. Wetherington, E. Frantz, M. LaBella, Z. Hughes, M. Fanton, and D. Snyder. Nucleation of epitaxial graphene on SiC(0001). *Acs Nano*, 4(1):153–158, January 2010.

[91] W. Norimatsu and M. Kusunoki. Formation process of graphene on SiC(0001). *Physica E*, 42(4):691–694, February 2010.

[92] C. Virojanadara, R. Yakimova, A. A. Zakharov, and L. I. Johansson. Large homogeneous mono-/bi-layer graphene on 6H-SiC(0001) and buffer layer elimination. *J. Phys. D: Appl. Phys.*, 43(37):374010, September 2010.

[93] K. V. Emtsev, F. Speck, T. Seyller, L. Ley, and J. D. Riley. Interaction, growth, and ordering of epitaxial graphene on SiC{0001} surfaces: A comparative photoelectron spectroscopy study. *Phys. Rev. B*, 77(15):155303, April 2008.

[94] C. Riedl, U. Starke, J. Bernhardt, M. Franke, and K. Heinz. Structural properties of the graphene-SiC(0001) interface as a key for the preparation of homogeneous large-terrace graphene surfaces. *Phys. Rev. B*, 76(24):245406, December 2007.

[95] J. B. Hannon, M. Copel, and R.M. Tromp. Determination of the graphene growth mode on SiC(0001) and SiC(000-1). *arXiv:1108.2627v1 [cond-mat.mtrl-sci]*, 2011.

[96] T. Filleter, K. V. Emtsev, T. Seyller, and R. Bennewitz. Local work function measurements of epitaxial graphene. *Appl. Phys. Lett.*, 93(13):133117, September 2008.

[97] A. Tiberj, J. R. Huntzinger, J. Camassel, F. Hiebel, A. Mahmood, P. Mallet, C. Naud, and J. Y. Veuillen. Multiscale investigation of graphene layers on 6H-SiC(000-1). *Nano. Res. Lett.*, 6:171, 2011.

[98] F. Ming and A. Zangwill. Model for the epitaxial growth of graphene on 6H-SiC(0001). *Phys. Rev. B*, 84(11):115459–115464, September 2011.

[99] J. W. Evans, P. A. Thiel, and M. C. Bartelt. Morphological evolution during epitaxial thin film growth: Formation of 2D islands and 3D mounds. *Surf. Sci. Rept.*, 61(1-2):1–128, April 2006.

[100] Arthur F. Voter. Introducton to the kinetic monte carlo method. In Kurt E. Sickafus, Eugene A. Kotomin, and Blas P. Uberuaga, editors, *Radiation Effects in Solids*, volume 235 of *NATO Science Series*, chapter 1, pages 1–23. Springer Netherlands, Dordrecht, 2007.

[101] M. C. Bartelt and J. W. Evans. Scaling analysis of diffusion-mediated island growth in surface-adsorption processes. *Phys. Rev. B*, 46(19):12675–12687, November 1992.

[102] T. Michely and J. Krug. *Islands, Mounds and Atoms: Patterns and Processes in Crystal Growth Far from Equilibrium*. Springer-Verlag, Berlin, 2004.

[103] J. Borysiuk, R. Bozek, W. Strupinski, A. Wysmolek, K. Grodecki, R. Stepniewski, and J. M. Baranowski. Transmission electron microscopy and scanning tunneling microscopy investigations of graphene on 4H-SiC(0001). *J. Appl. Phys.*, 105(2):023503, January 2009.

[104] W. Norimatsu and M. Kusunoki. Selective formation of ABC-stacked graphene layers on SiC(0001). *Phys. Rev. B*, 81(16):161410, April 2010.

[105] F. Ming and A. Zangwill. Phase field modeling of submonolayer epitaxial growth. *Phys. Rev. B*, 81(23):235431–235435, June 2010.

[106] S. Chen, B. Merriman, S. Osher, and P. Smereka. A simple level set method for solving stefan problems. *J. Comput. Phys.*, 135(1):8–29, July 1997.

[107] M. F. Gyure, C. Ratsch, B. Merriman, R. E. Caflisch, S. Osher, J. J. Zinck, and D. D. Vvedensky. Level-set methods for the simulation of epitaxial phenomena. *Phys. Rev. E*, 58(6):R6927–R6930, December 1998.

[108] C. Ratsch, M. F. Gyure, S. Chen, M. Kang, and D. D. Vvedensky. Fluctuations and scaling in aggregation phenomena. *Phys. Rev. B*, 61(16):10598–10601, April 2000.

[109] C. Ratsch, M. Kang, and R. E. Caflisch. Atomic size effects in continuum modeling. *Phys. Rev. E*, 64(2):020601, August 2001.

[110] Y. M. Yu and B. G. Liu. Phase-field model of island growth in epitaxy. *Phys. Rev. E*, 69(2):021601, February 2004.

[111] H. Emmerich. Advances of and by phase-field modelling in condensed-matter physics. *Adv. Phys.*, 57(1):1–87, 2008.

[112] W. K. Burton, N. Cabrera, and F. C. Frank. The growth of crystals and the equilibrium structure of their surfaces. *Philos. Trans. R. Soc. London, Ser. A*, 243(866):299–358, 1951.

[113] A. Karma and W. J. Rappel. Phase-field method for computationally efficient modeling of solidification with arbitrary interface kinetics. *Phys. Rev. E*, 53(4): R3017–R3020, April 1996.

[114] O. Pierre-Louis. Phase field models for step flow. *Phys. Rev. E*, 68(2):021604, August 2003.

[115] C. Ratsch, P. Šmilauer, A. Zangwill, and D. D. Vvedensky. Submonolayer epitaxy without a critical nucleus. *Surf. Sci.*, 329(1-2):L599–L604, May 1995.

[116] J. A. Stroscio and D. T. Pierce. Scaling of diffusion-mediated island growth in iron-on-iron homoepitaxy. *Phys. Rev. B*, 49(12):8522–8525, March 1994.

[117] J. G. Amar, F. Family, and M. N. Popescu. Kinetics of submonolayer epitaxial growth. *Comput. Phys. Commun.*, 146(1):1–8, June 2002.

[118] M. Petersen, C. Ratsch, R. E. Caflisch, and A. Zangwill. Level set approach to reversible epitaxial growth. *Phys. Rev. E*, 64(6):061602, December 2001.

[119] N. Provatas, N. Goldenfeld, and J. Dantzig. Adaptive mesh refinement computation of solidification microstructures using dynamic data structures. *J. Comput. Phys.*, 148(1):265–290, January 1999.

[120] J. L. Blue, I. Beichl, and F. Sullivan. Faster Monte Carlo simulations. *Phys. Rev. E*, 51(2):R867–R868, February 1995.

VITA

Fan Ming was born in 1983 as the first child of the family in a small town named Yingshan in central China. After finishing high school with academic success, he went to Peking University in Beijing to study physics in 2001. He studied ohmic contacts and the spin Hall effect for undergraduate research practice. After graduating Peking University with a Bachelor of Science degree, the research experience inspired him and led him to begin the graduate studies at Georgia Institute of Technology.

At Georgia Tech, he focused his research on epitaxial graphene growth mechanism. He fulfilled the requirements for the degree Doctor of Philosophy in Physics in 2011. After graduation, Fan will join Micron Technology at Boise, Idaho as a Metrology Engineer.